DOE-ET-53088-275

IFSR#275

PLASMA CURRENT SUSTAINED BY FUSION CHARGED PARTICLES IN A FIELD REVERSED CONFIGURATION

*H.L. Berk, H. Momota** and *T. Tajima*
Institute for Fusion Studies
The University of Texas at Austin
Austin, Texas 78712

* Institute of Plasma Physics, Nagoya Univ., Nagoya 464 Japan

April 1987

Plasma Current Sustained by Fusion Charged Particles in a Field Reversed Configuration

H.L. BERK, H. MOMOTA,[a] AND T. TAJIMA
Institute for Fusion Studies
The University of Texas at Austin
Austin, Texas 78712

The distribution of energetic charged particles generated by thermonuclear fusion reactions in a field reversed configuration (FRC) are studied analytically and numerically. A fraction of the charged fusion products escapes directly while the others are trapped to form a directed particle flow parallel to the plasma current. It is shown that the resultant current density produced by these fusion charged particles can be comparable to background plasma current density that produces the original field reversed configuration in a D-^3He reactor. Self-consistent equilibria arising from the currents of the background plasma and proton fusion products are constructed where the Larmor radius of the fusion product is of arbitrary size. Reactor relevant parameters are examined, such as how the fusion reactivity rate varies as a result of supporting the pressure associated with the fusion products. A model for synchrotron emission from various pressure profiles is developed and it is shown quantitatively how synchrotron losses vary with different pressure profiles in an FRC configuration.

[a] Permanent address: Institute of Plasma Physics, Nagoya University, Nagoya 464, Japan

I Introduction

Energetic particle beams in a magnetized plasma have been studied as a means of sustaining current[1–6] or for stabilizing various instabilities in a plasma.[1,2,7–9] Often, the use of externally imposed neutral beams is assumed. However, a large amount of energetic fusion charged particles can be present in a burning plasma. In these situations, studies on the favorable or unfavorable effects of fusion charged particles are of interest and of great importance.

In order to provide a distinct model, we will analyze the behavior of fusion charged products in an axisymmetric field reversed configuration (FRC). One important characteristic of this configuration is that the typical Larmor radius of the fusion product is quite large and sometimes comparable to the separatrix radius. This brings in a number of significant consequences, including the possibility that a significant fraction of the current can be sustained by the fusion products.

We will choose the z-axis of the cylindrical coordinates as the axis of symmetry. The flux function of a field reversed configuration is taken as zero on the separatrix and without loss of generality it is assumed that it is positive inside the separatrix. Thus, the flux function has its maximum value at the field null and decreases monotonically away from the null point.

The fusion products move in dynamical orbits in accordance with the equations of motion and Coulomb collisions. We assume that at birth Coulomb drag dominates the collision processes. Only at lower energies, where the effect on current flow is small, is the Coulomb scattering process important. This assumption is satisfied for protons that are produced from the reaction of D-^3He in the plasma of density of interest ($\sim 10^{15}\text{cm}^{-3}$). Thus we are justified in only accounting for drag when considering the effect of collisions.

We shall investigate the structure of the currents formed by fusion products by two methods. One is a semi-analytical one in which an ergodicity assumption is made that a particle with a fixed speed and canonical angular momentum can reach every point of its accessible region of phase space with equal probability. This assumption was also invoked by Lovelace,[3] who investigated a somewhat similar problem but with emphasis

of the structure of systems whose high energy particles have Larmor radii the size of the plasma radius. We are able to derive the steady-state distribution function which evolves according to the Fokker-Planck drag equation. From this distribution we calculate the current that arises from the charged fusion products.

The rigorous justification of this method depends on the accuracy of the ergodic assumption. In an alternate approach, we develop a particle simulation method for constructing the current profile. The orbits of a group of particles that are distributed with an initial weight proportional to the local rate of fusion production and which slow down according to the classical drag equation, are integrated in time. We then calculate the current produced by such a distribution and show that the time integrated current of this distribution function is, to within the accuracy of the statistical fluctuations, exactly the steady-state distribution one would calculate when one has a continuous source given by the fusion production rate.

An analysis of the exact particle orbits indicates that the ergodic assumption is not fulfilled. Nonetheless, the current profiles obtained by the particle simulation method are qualitatively similar to the semi-analytic method that uses the ergodic hypothesis. We discuss the reason for the close agreement of the two methods as well as compare the discrepancies.

The investigation of the currents produced by the slowing down distribution shows that it produces similar current profiles as prompt fusion products that last about a slowing down time, and are then lost. The distribution of currents for such a mechanism is easily obtained, and as a result the self-consistent magnetic field is readily calculated. With this calculation one can quantitatively assess various fusion parameters such as the reactivity, synchrotron radiation, plasma size, required magnetic field, etc. Examples of such parameters will be presented.

An important point that one needs to consider is whether fusion products actually carry current, or whether they are just a source of momentum, and their current is cancelled by the plasma background current, or alternatively the fusion products induce current via the Ohkawa effect[4] which arises if the fusion product has a different atomic number than the effective atomic number of the plasma. In this paper we assume that the charged fusion product carries a current. We note that Sudan and Reimann[5] and Hammer and

Berk[6] have pointed out that a significant plasma back-current can only arise if the plasma obtains a significant rotational velocity that is driven by $\mathbf{E} \times \mathbf{B}$ drifts of a radial electric field. If a mechanism for electron viscosity exists, these electric fields are shorted out and the currents induced by the fusion products will not be be cancelled by the background plasma. In Ref. 5, it is pointed out that the instabilities that can arise from the induced electric fields, is a mechanism for maintaining the needed electron viscosity which enables the flow of the charged energetic species to be a current. Alternatively, externally imposed θ-symmetry violations can induce the need electron viscosity.[6]

Section II discusses the semi-analytical method of treating the velocity and spatial distribution of the fusion produced particles. The particle simulation method and results are presented in Sec. III. Section IV deals with the self-consistent magnetic field calculation. Section V discusses various reactor relevant physical quantities and their relative merits for a fusion reactor and draws conclusions.

II Semi-Analytical Method

Particles moving in a magnetic field without an electric field have two exact constants of motion: its speed v and the canonical angular momentum per unit mass $p = rv_\theta + U(r,z)$, where U is the magnetic flux function ψ multiplied by q/Mc with q the charge and M the mass of the particle. Particles with given p and v are confined within an accessible domain $D_{(p,v)}$ of the phase space with $D_{(p,v)}$ defined by:

$$D_{(p,v)} = \{(\mathbf{r}, \mathbf{v}) : \quad rv > |p - U(r,z)|\} \tag{1}$$

(i.e., the domain of accessible $\mathbf{r}$, $\mathbf{v}$ is determined by the conditions $rv > |p - U(r,z)|$ with p and v constant). Examples of the domains D_1, D_2, D_3, ... for canonical momenta p_1, p_2, p_3, ... with $p_1 > p_2 > p_3 > \ldots$, are shown in Fig. 1. One can readily show that, if $p_j < p_k$ and $p_j > 0$, the outer boundary surface of D_j surrounds the other boundary surface of D_k, while the inner boundary surface (if it exists) of D_j surrounds the inner boundary surface of D_k (if it exists). For a given v, the maximum value of $p = p_b$ (for which D is a single point in our diagram) is determined by the betatron condition

$$r_b v \;=\; p_b - U(r_b, 0)$$

$$v = -\frac{d}{dr}U(r_b, 0), \tag{2}$$

where $z = 0$ is the mirror symmetry point in the z-direction. For values of $p > p_c$, D does not have an inner boundary, while for $p < p_c$, D has an inner boundary, with p_c determined from the conditions

$$\begin{aligned} r_c v &= U(r_c, 0) - p_c \\ v &= \frac{d}{dr}U(r_c, 0). \end{aligned} \tag{3}$$

We note that at $p = av$, the domain D grazes the separatrix and for $p < av$, the domain D intersects the separatrix, where a is the radius of the separatrix at $z = 0$.

The motion of the particle does not have another exact invariant although an additional adiabatic invariant or dynamical accessibility constraints may exist. As a first approximation or as a model, it is assumed that particles can reach on a collision time scale, every point of the accessible phase space domain with equal probability (maximum ergodicity). This assumption has also been made by Lovelace in related studies of ion rings.[10,11] The accuracy of the stochasticity assumption has also been studied in Refs. 12 and 13.

We will also assume that if a particle penetrates the separatrix, it is lost quickly compared to a characteristic collision rate of the plasma, through such processes as edge cooling, charge exchange, orbit instabilities, due to the relatively sharp magnetic field at the separatrix, etc. This assumption may be somewhat controversial, as in some concepts an important role is played by particles confined on open field lines. Nevertheless, if energy confinement on closed lines is appreciably greater than on open field lines, our assumption is valid as long as the confined plasma is isothermal up to the separatrix. Thus, we define a particle to be confined if its accessible domain does not penetrate the separatrix. It follows from the above considerations that the condition for a fusion charged particle being confined within the separatrix can be described by the inequality:

$$p > av. \tag{4}$$

We will see later this selective particle confinement gives rise to a directed particle flow in a plasma.

In order to analyze the directed flows, we shall evaluate the distribution function of the fusion charged particles. A certain amount of fusion charged particles will be lost directly

through the separatrix and the other particles satisfying condition (4) are trapped within the separatrix. Since the initial speed v_0 of these trapped particles is much higher than the thermal speed of plasma ions and much lower than the electron thermal speed under consideration, collisions primarily cause a drag force due to the background electrons. When pitch angle diffusion becomes appreciable, the speeds of fusion products are low, and thus will not greatly influence the expressions we obtain for the particle flow. Thus the equation for the distribution $f(r,z,\theta,p,v,v_z)$ of the charged fusion products takes the form:

$$\begin{aligned} v_r\frac{\partial f}{\partial r} &+ \frac{(p-U)}{r^2}\frac{\partial f}{\partial \theta} + v_z\frac{\partial f}{\partial z} + \frac{v_\phi}{r}\frac{\partial U}{\partial z}\frac{\partial f}{\partial v_z} \\ &= \nu(r,z)\left[1+\frac{v_c^3(r,z)}{v^3}\right]\left[3f + v\frac{\partial f}{\partial v} + rv_\phi\frac{\partial f}{\partial p} + v_z\frac{\partial f}{\partial v_z}\right] \\ &+ S(r,z)\frac{\delta(v-v_0)}{4\pi v^2}\theta(p-av_0)\theta\left[p_b(v_0)-p\right], \end{aligned} \tag{5}$$

where $\nu(r,z)$, $v_c(r,z)$ and $S(r,z)$ are respectively: the frequency of the slowing down collisions due to the electron drag with

$$\nu/n = \frac{4(2\pi)^{1/2}e^4\ln\Lambda}{3T_e^{3/2}M} \approx \frac{2.9\times10^{-6}\ln\Lambda}{A\tilde{T}_e^{3/2}}.$$

(e is the electronic charge, M the fusion product mass, A the atomic number, and T_e and $\tilde{T}_e$ are the electron temperature in ergs and in eV), the critical speed where angular scattering becomes appreciable, and the generation rate of fusion particles per unit volume. The function $\delta(r)$ is Dirac's delta function and $\theta(x)$ is Heaviside's step function.

For weak collisions and sources, the left-hand side of Eq. (5), is denoted as $L_0 f$ and it describes the evolution on a dynamical time scale. $L_0 f$ is normally large compared to the right-hand side of Eq. (5), which we denote as $-L_1 f + A$. The left-hand side describes collisions and the fusion production rate. Thus, we take $f = f_0 + f_1$, with $f_0 \gg f_1$, and using perturbation theory, we have for the first two orders,

$$\begin{aligned} L_0 f_0 &= 0 \\ L_0 f_1 &= -L_1 f_0 + A. \end{aligned} \tag{6}$$

The form $f_0(p,v)$ certainly solves $L_0 f_0 = 0$. A more general solution for f_0 can arise if the particle motion possesses adiabatic invariants or if the collisionless flow has KAM

(Kolmogorov-Arnold-Mozer) surface barriers that prevents all of the region $D_{(p,v)}$ from being reached. However, if we assume that neither adiabatic invariants or KAM barriers exist for the configuration we are studying, then $f_0 = f_0(p,v)$ is the solution of the first equation in (6). In the second equation of (6) we can eliminate f_1 by integrating the volume element $drd\theta dv_z dz/\left|v_r(v,p,U,p_z)\right|$ over its accessible domain. One can show that the left-hand side vanishes by assuming regular boundary conditions, using $v_\theta \partial U/\partial z = r\partial v_r^2/\partial z$ and performing suitable parts integrations. We then obtain the following equation which describes the evolution of $f_0(p,v)$,

$$\frac{\partial}{\partial v}\left[\left(\langle\nu\rangle v^3 + \left\langle\nu v_c^3\right\rangle\right) f(p,v)\right] + \frac{1}{v}\left[\langle\nu\rangle p - \langle\nu U\rangle\right]\frac{\partial}{\partial p}\left[\langle\nu\rangle v^3 + \left\langle\nu v_c^3\right\rangle\right] f$$
$$= -\frac{\langle S\rangle}{4\pi}\delta(v-v_0)\theta(p-av_0)\theta\left[p_b(v_0)-p\right], \tag{7}$$

where the volumetric mean of a quantity $Q(r,z)$ is defined as:

$$\langle Q\rangle_{(p,v)} \equiv \frac{\displaystyle\int_{D_{(p,v)}} \frac{1}{|v_r|} Q(r,z)dv_z dr dz}{\displaystyle\int_{D_{(p,v)}} \frac{1}{|v_r|} dv_z dr dz} = \frac{\displaystyle\int_{rv>|p-U|} Q(r,z)drdz}{\displaystyle\int_{rv>|p-U|} drdz}. \tag{8}$$

Note that the subscript (p,v) was suppressed in Eq. (7) as well as the subscript 0 in f_0. If for simplicity we neglect the space dependence of ν_c, we can rewrite Eq. (7) as,

$$\frac{\partial}{\partial v}\left[\left(v^3+v_c^3\right) f\right] + \frac{1}{v}\left[p - \frac{\langle\nu U\rangle}{\langle\nu\rangle}\right]\left(v^3+v_c^3\right)\frac{\partial f}{\partial p}$$
$$= -\frac{\langle S\rangle}{4\pi\langle\nu\rangle}\delta(v-v_0)\theta(p-av_0)\theta\left[p_b(v_0)-p\right]. \tag{9}$$

The solution to Eq. (9) obtained by the use of the method of characteristics is

$$f(p,v) = \frac{\langle S\rangle_{[p_0(p,v),v_0]}}{4\pi(v^3+v_c^3)\langle\nu\rangle_{[p_0(p,v),v_0]}}\theta\left[p_0(p,v)-av_0\right]\theta\left[p_b(v_0)-p_0(p,v)\right]\delta(v-v_0). \tag{10}$$

Here, the quantity p_0 is to be defined as a function of p and v through the solution $p(u) \equiv p(u;p_0(v_0))$ of the characteristic equation defined from Eq. (9),

$$\frac{d}{du}\left[\frac{p(u)}{u}\right] = -\frac{\langle\nu U\rangle}{\langle\nu\rangle}\frac{1}{u^2} \tag{11}$$

with the initial condition: $p(u=v_0)=p_0$ and final endpoint condition $p(u=v)=p$. The integral of Eq. (11) is

$$p(v) = \frac{p_0 v}{v_0} + v\int_v^{v_0} du\frac{\langle\nu U\rangle}{\langle\nu\rangle}. \tag{12}$$

It then follows that a fusion product, whose accessible domain just grazes the separatrix (i.e., $p_0 = av_0$), will as it slows down have a domain that always lies inside the separatrix. This follows from Eq. (12) because if $p_0 = av_0$, we see that $p(v) > av$ for $v < v_0$. Further, from the property that the solutions to Eq. (11) with different initial p_0 values cannot cross, it readily follows that particles born with $p_0 > av_0$ will likewise always be trapped as they slow down.

It can also be shown that the solution for $p(u)$ with $p(v_0) = p_b(v_0)$ is $p_b(u)$, so that a particle born in a betatron orbit remains in a betatron orbit as it slows down. Thus the Heaviside function $\theta(p_b(v_0) - p_0(p,v))$ in Eq. (10) can be suppressed. As $p_b(v) \geqq rv - U(r,z)$, p in Eq. (10) can take on all values in the physical domain $rv < -|p - U(r,z)|$.

We now use Eq. (10) for the distribution function, to evaluate the fusion product current flow J_f in the θ-direction. We use

$$d^3v = \frac{2dv_z dp dv v}{r\left[v^2 - (p-U)^2/r^2 - v_z^2\right]^{1/2}}$$

where the factor of 2 accounts for positive and negative v_r,

$$v_\theta = \frac{1}{r}\left[p - U(r,z)\right]$$

and we integrate over the accessible region of v_z to find,

$$\begin{aligned} J_f \;\equiv\; & q\int d^3v v_\theta f = \frac{q}{2r^2}\int_0^{v_0} \frac{dvv}{(v^3 + v_c^3)} \\ & \times \int_{U(r,z)-rv}^{rv+U(r,z)} dp[p - U(r,z)]\frac{\langle S\rangle_{p_0,v_0}}{\langle \nu\rangle_{p_0,v_0}}\theta\left[p_0(p,v) - av_0\right] \end{aligned} \tag{13}$$

We also note that if the background plasma is isothermal and if the relative concentration of the reacting ion mixture is homogeneous (we shall now assume the fusion product results from the interaction of two species with densities n_1 and n_2 with a reaction rate σv_i) then

$$\frac{\langle S\rangle_{p_0,v_0}}{\langle \nu\rangle_{p_0,v_0}} = g\frac{\langle n^2\rangle_{p_0,v_0}}{\langle n\rangle_{p_0,v_0}}\frac{\sigma v_i}{\nu/n}; \tag{14}$$

with $g \equiv n_{10}n_{20}/n_0^2$ with n_{10}, n_{20}, n_0 the density at the field null for the two ion species and the electrons respectively. For an axially extended MHD equilibrium with $\partial P/\partial U \equiv$ const, with P the background plasma pressure the magnetic field at the mid-plane is of the form[14]

$$\frac{qB_H(r)}{Mc} = \omega_c\left(1 - \frac{2r^2}{a^2}\right) \tag{15}$$

where $\omega_c = qB_H(a)/Mc$, with M the mass of the fusion product. The background plasma current, J_p, is given by

$$4\pi J_p(r) = \frac{\partial B_H}{\partial r} = \frac{-4M\omega_c r}{qa^2}. \tag{16}$$

Then the ratio $J_f(r,z)/J_p(a)$ can be written as

$$\frac{J_f(r,z)}{J_p(a,0)} = g\frac{\beta_e E_F}{4T_e}\frac{n_0\overline{\sigma v_i}}{\nu_0}\alpha I_H(r,z) \tag{17}$$

where $\alpha = a\omega_c/v_0$, $T_e \equiv$ electron temperature, $\beta_e \equiv 8\pi n_0 T_e/B_H^2(a) \equiv$ electron beta for Hill's extended vortex solution,[15] $E_F = Mv_0^2/2$, and the renormalized current is defined as

$$\begin{aligned} I_H(r,z) &= \frac{1}{2}\frac{a^2}{r^2}\int_0^1 \frac{dss}{s^3+s_c^3} \\ &\times \int_{\tilde{U}(r,z)-xs}^{\tilde{U}(r,z)+xs} dy[y-U(r,z)]\frac{\langle n^2\rangle_{p_0,v_0}}{n_0\langle n\rangle_{p_0,v_0}}\theta(p_0-av_0) \end{aligned} \tag{18}$$

with $s = v/v_0$, $y = p/av_0$, $x = r/a$, $\tilde{U}(r,z) = U(r,z)/av_0 = \alpha x^2(1-x^2)$ with $z = 0$ and $s_c = v_c/v_0$. We have assumed that the background temperature is constant in space.

To evaluate these integrals we need to know how $p_0(y,s)$ is to be determined. This is obtained by evaluating Eq. (12) numerically. Results are shown in Fig. 2 for $\alpha = 5$ and 15. These curves need to be used in determining the density functions $\langle n^2\rangle_{p_0,v_0}$ and $\langle n\rangle_{p_0,v_0}$ in the integrand of Eq. (18). For example, in Fig. 2, there is a curve that links the point (s,y) to an initial value point $s = 1$ and $y = y_0$. Thus from the curve that intersects at a given (s,y), we can determine the value of y_0 of the curve at $s = 1$, and thereby obtain $p_0 = av_0y_0$, which one needs to know in evaluating the volumetric means $\langle n^2\rangle_{p_0,v_0}$ and $< n >_{p_0,v_0}$.

It is interesting to evaluate I_H assuming $k \equiv \langle n^2\rangle_{p_0,v_0}/\langle n\rangle_{p_0,v_0}$ is independent of p and v. In this case the y integration in Eq. (18) can be performed and yields,

$$I_H(r,z) = \frac{1}{2}\int_0^1 ds\frac{s}{s^3+s_c^3}Gk \tag{19}$$

where

$$G = \left[\frac{y^2}{2} - \tilde{U}(r,z)y\right]\Big|_{y=\tilde{U}(r,z)-xs}^{y=\tilde{U}(r,z)+xs}\theta\left[\tilde{U}(r,z)+xs-y(s;1)\right],$$

$y(s;y_0=1) = p(v;av_0)/av_0$, and $y(s) \equiv y(s;y_0=1)$ satisfies the differential equation obtained from Eq. (11)

$$\frac{d}{ds}\left(\frac{y}{s}\right) = -\frac{\langle\nu\tilde{U}\rangle}{\langle\nu\rangle s^2} \tag{20}$$

with the initial condition $y = 1$ when $s = 1$. The numerical solution of Eq. (20) (with $\nu \propto U$) is the lowest curve of Fig. 2 for an arbitrarily long equilibrium. Observe that if $\tilde{U}(ax, z) - xs > y(s;1)$ then $G = 0$, while if $\tilde{U}(ax, z) + xs > y(s;1) > \tilde{U}(ax, z) - xs$, we find

$$G = \frac{1}{2}\left[x^2 s^2 - \tilde{U}^2(r, z)\right] - y(s;1)\left[\frac{y(s;1)}{2} - \tilde{U}(r, z)\right]. \tag{21}$$

The remaining s integral has to be performed numerically.

It is important to have an insight into these solutions for G. If $U(r, z) - xs < y(s;1) < U(r, z) + xs$, particles can reach the point (ax, z), but part of the phase space accessible to (ax, z) is unoccupied because of direct losses. The imbalance in the occupation of phase space allows a flow. The mechanism is quite similar to an array of equal strength diamagnetic loops that suddenly terminate (as shown in Fig. 3). In the region of the last Larmor diameter, such as point "b" in Fig. 3, the downward vertical flux of particles whose guiding centers are on the left of the observation point, is larger than the upward flux of particles whose guiding centers are on the right side of the observation point where guiding centers are depleted. However, if $\tilde{U}(xs, z) - xs > y(s;1)$, all the particles that can dynamically reach the point (ax, z) are all part of a phase space region with no direct losses. Then, the model of treating $\langle n^2 \rangle / \langle n \rangle$ as a constant, produces a birth source that is independent of phase space. As a result, there is no preferred direction of the flow and one obtains complete cancellation of the current, in a manner quite analogous to the flux cancellation at point "a" in Fig. 3.

We have evaluated Eq. (18) numerically with $\nu \propto \tilde{U}$. The results are shown in Fig. 4 for $\alpha = 5$, 10 and 15. Note that $1/\alpha$ is the ratio of the gyroradius in the vacuum field to the plasma radius. For small α we obtain a smooth profile of the current density. At larger $\alpha(\alpha = 10)$ a dip develops, which becomes a very pronounced minimum as α increases further ($\alpha = 15$). We note that the zeros of the current I_H at small x arises because none of the fusion products born at small x are contained. The small values of I_H in the central region arises because of the cancellation that arises from particles with oppositely directed velocities.

It is interesting to compute the current profiles obtained if we assume $\langle n^2 \rangle_{p_0, v_0} / \langle n_0 \rangle_{p_0, v_0}$ is a fixed number and the contained fusion products exist for a time λ/ν_0 without slowing

down. For this model the current profile factor in Eq. (18), $I_H(x,z) \equiv I_M$ is found to be

$$I_M = \frac{\lambda}{4}\left\{1 - \left[\tilde{U}(x,z) - 1\right]^2 \Big/ x^2\right\} \theta\left[x^2 - (\tilde{U}-1)^2\right]. \tag{22}$$

Plots of this function are shown in Fig. 5 with $\lambda = 1$. We note that the current profiles of this model are very similar to the slowing down model. The amplitudes are slightly different but choosing $\lambda \approx 0.6$ synchronizes the amplitudes of the current from the two models quite closely. When there is no slowing down and no bias in the initial production of fusion products, there is an exact cancellation of the current in the region of good containment. This explains exact zeros of the $\alpha = 15$ case between $0.55 < x < 0.8$ in Fig. 5(c). Since the model distribution gives current profiles similar to the slowing down distribution function, we can study the self-consistent magnetic field generated with fusion products, using the model distribution. The results of this study will be given in Sec. IV.

We further note that the model given by Eq. (22) can be expected to be accurate if $\alpha \lesssim 16$, and fail for larger values of α. This estimate arises by observing that for large α, the peak of the fusion product current density arises from roughly fusion particle production two Larmor radii within the separatrix. In the large α approximation, this point is at $x = x_L \equiv 1 - 2/\alpha$, and the approximate value of $U(x_L) \equiv U_L$ at this point is $U_L = 2$, while the maximum value of U is $U_{\max} = \alpha/8$. When $U_L/U_{\max} < 1$, the edge fusion product currents are driven by a source $\overline{n^2\sigma v_i}/\nu \propto n(x = x_L)$. At smaller α-values, the point x_L approaches the null of the configuration (indeed the approximation $x_L \approx 1 - 2/\alpha$ is incorrect), and then the source of fusion products is roughly independent of α and proportional to n_0. The transitions of these two regions is at $U_L/U_{\max} = 1$, which we see is at $\alpha = 16$.

Another parameter of interest is the fraction, h, of fusion products trapped. This parameter is given by

$$\begin{aligned} h &= \frac{\int d^3r d^3v \theta(p_0 - av_0) n_p^2 \overline{\sigma v_i} \theta(p_0 - av_0) \delta(v - v_0)}{\int d^3r d^3v n_p^2 \overline{\sigma v_i} \delta(v - v_0)} \\ &= \frac{\int_0^1 dx x n_p^2(x) \max\left\{\left[\max\left(\tilde{U}(x) + x, y_{\max}\right) - \min\left(\tilde{U}(x) - x, y_{\min}\right)\right], 0\right\}}{\int_0^1 dx x n_p^2(x)} \end{aligned} \tag{23}$$

where $n_p(x)$ is the background plasma density when it is assumed the background plasma is isothermal and we have taken an elongated equilibrium so that we can neglect the z-dependence. If $\partial P/\partial \tilde{U} \equiv$ constant, then $n_p(x) \propto \tilde{U}(x)$. We also note that $y_{\min} = 1$, and $y_{\max}$ is determined from the solution of the equations

$$\begin{aligned} y_{\max} &= \tilde{U}(x) + x \\ 1 &= -\frac{d\tilde{U}}{dx}. \end{aligned}$$

The results are shown in solid curve of Fig. 6. Note that over half the fusion products are retained if $\alpha > 9$.

We have also examined cases where we have modelled $n_p^2\overline{\sigma v_i} \propto n_p$ and ν is constant. We find that the current profile has a very similar structure and amplitude. Also the fraction of retained fusion particles is quite similar as seen in the dotted curve in Fig. 6. It is this latter model that was primarily used in our particle simulation studies which are discussed in the next section.

Other pressure profiles can also be considered. For example one can choose

$$\frac{4\pi q_0^2 a^2}{v_0^2 M^2 c^2}\frac{\partial P(\tilde{U})}{\partial \tilde{U}} = 4\alpha \exp(-\sigma \tilde{U}/\tilde{U}_{\max}) \tag{24}$$

and hence

$$\tilde{P}(\tilde{U}) \equiv \frac{4\pi q^2 a^2 P(\tilde{U})}{c^2 M^2 v_0^2} = \frac{4\alpha \tilde{U}_{\max}}{\sigma}\left[1 - \exp\left(-\frac{\sigma \tilde{U}}{\tilde{U}_{\max}}\right)\right]. \tag{25}$$

For $\sigma = 0$ we recover the results for the constant pressure $\partial P/\partial U$ profile discussed earlier. However, with finite σ, one obtains equilibria that shields out a larger fraction of the external magnetic field. The solution to the normalized MHD equilibrium equation

$$\frac{1}{x}\frac{\partial}{\partial x}\frac{1}{x}\frac{\partial \tilde{U}}{\partial x} = -\frac{\partial \tilde{P}}{\partial \tilde{U}} = -4\alpha \exp\left(-\frac{\sigma \tilde{U}}{\tilde{U}_{\max}}\right), \tag{26}$$

with $(0 < x < 1)$ is found to be

$$\frac{\tilde{U}(x)}{\tilde{U}_{\max}} = 1 - \sigma^{-1} \ln\left\{1 + \tan^2\left[4\tan^{-1}(e^{\sigma} - 1)^{1/2}\left|\frac{x^2 - 1/2}{2}\right|\right]\right\} \tag{27}$$

with the following equilibrium relations holding as well,

$$\tilde{U}_{\max} = \frac{\sigma \alpha_{\text{eff}} \exp(-\sigma/2)}{8\left[\tan^{-1}\left(\exp(\sigma) - 1\right)^{1/2}\right]\left[1 - \exp(-\sigma)\right]^{1/2}}$$

$$\longrightarrow \begin{cases} \frac{\alpha_{\rm eff}}{8}, & \sigma \ll 1 \\ \sigma\alpha_{\rm eff}\exp(-\sigma/2)/4\pi, & \sigma \gg 1 \end{cases}$$

$$\alpha_{\rm eff} \equiv \left|\frac{\partial U(x=1)}{\partial x}\right| = \frac{\alpha\exp(-\sigma/2)\left[1-\exp(-\sigma)\right]^{1/2}}{\tan^{-1}\left(\exp(\sigma)-1\right)^{1/2}} \tag{28}$$

$$\longrightarrow \begin{cases} \alpha, & \sigma \ll 1 \\ \frac{2\alpha}{\pi}e^{-\sigma/2}, & \sigma \ll 1 \ . \end{cases}$$

Note that $\alpha_{\rm eff}$ is the ratio of the separatrix radius to the maximum fusion product Larmor radius. In Fig. 7 we plot $U_{\rm max}$ as a function of σ for fixed $\alpha_{\rm eff}$. Note that $U_{\rm max}$ decreases at fixed $\alpha_{\rm eff}$ with increasing σ.

We can also construct h, the fraction of retained fusion products if we take $n_p(x) \propto \left[1-\exp\left(-\frac{\sigma\tilde{U}}{\tilde{U}_{\rm max}}\right)\right]$. The results will be discussed in Sec. IV when we present results that self-consistently account for currents arising from fusion products. For now we note that h decreases with increasing σ for fixed $\alpha_{\rm eff}$, because with increasing σ less magnetic flux is trapped and magnetic flux is needed to contain a charged particle. We note, however, that h as a function of $U_{\rm max}$ is quite insensitive to σ, as is seen in Fig. 8, where h is plotted as a function of $\tilde{U}_{\rm max}$ for $\sigma = 0.0, 1.0, 2.0$. Other interesting parameters relevant to a fusion reactor, such as synchrotron emission, will be discussed in Sec. IV.

III Particle Simulation Method

Before describing the particle simulation method we note that there is a fundamental identity between the time integrated solution of an initial value problem and a steady-state problem. Consider the following dynamical kinetic equation

$$\frac{\partial f}{\partial t} + Lf = 0 \tag{29}$$

where L is a kinetic operator independent of time that includes phase space flow (the Vlasov equation), collisions (Fokker-Planck equation) and sinks through the boundary conditions on L. Suppose at $t = 0$ the distribution function is determined by an initial condition $f = S_0(r,v)$ and at $t = \infty$, $f = 0$, i.e., all particles lost at the position (r,v). Then integrating this equation from $t = 0$ to infinity, yields,

$$Lg = S_0(r,v) \tag{30}$$

where $g = \int_0^\infty f dt$. Note that this time averaged equation is the steady state kinetic equation for a source $S_0(r,v)$. This observation allows us to calculate by a dynamical simulation method steady-state quantities from an initial set of data. In particular, if $S_0(r,v)$ is an initial distribution $f(r,v,t=0)$ which then evolves in time, the time integral of $f(r,v,t)$ (or any moment) at fixed (r,v) yields the steady state distribution for a steady source $S_0(r,v)$.

The particle simulation is performed with a toroidal particle code.[15] The particle dynamics is evaluated in $r, \theta, z, p_r, p_\theta, p_z$ coordinates. An equilibrium for an axially extended constant pressure gradient ($\partial P/\partial\psi \equiv$ pressure, $\psi \equiv$ magnetic flux) is chosen which is of the form[14]

$$\psi = \frac{b\tilde{r}^2}{2}\left\{1-\tilde{r}^2-\left(\frac{1}{1+\frac{6}{\epsilon^2}+\frac{4}{\epsilon^4}}\right)\left[\frac{1}{2}\left(\tilde{r}^2-1\right)\left(\tilde{r}^2-2\right)-6\tilde{z}^2\left(\tilde{r}^2-1\right)+4\tilde{z}^4\right]\right\}, \quad (31)$$

and the magnetic field $\mathbf{B}$ is given by

$$\mathbf{B} = \nabla\psi \times \hat{\theta}/r$$

where $\tilde{r} = r/a$, $\tilde{z} = z/z_0$, $\epsilon = a/z_0$, b is the axially magnetic field at the separatrix, and a is the radius of the separatrix at $z=0$. The poloidal flux ψ is defined such that $\psi = 0$ on the separatrix. Note that with ϵ small, ψ is the same as U (to within a scale factor) which was studied in the previous section. We assume the plasma is isothermal, so that the pressure is of the form,

$$P(\psi) = n_0(\psi)T_0 = \frac{n_0(\psi_{\max})}{\psi_{\max}}\psi T_0 \equiv C\psi. \quad (32)$$

The equation of motion for individual particles are

$$\frac{d\mathbf{v}}{dt} = \frac{q}{M}\mathbf{v}\times\mathbf{B}(\mathbf{r}) - \nu\mathbf{v}, \quad (33)$$

where ν is the slowing down rate due to collisions. Electric field effects are neglected. In the simulation we remove particles if they reach the separatrix where ψ becomes negative.

Two types of simulations were performed; one with ν constant and the other ν proportional to the density n of the plasma. When ν is taken independent of n, the source

S is taken to be proportional to n, while when ν is proportional to n, S is taken to be proportional to n^2, since $S = n_p^2 \overline{\sigma v_i}$. The results of the two methods are similar. Most of the simulations are with the former method, which will be shown here.

The steady-state current is obtained by accumulating in time

$$J_\theta(r,z) = \frac{1}{T}\int_0^T dt \sum_j v_{\theta_j}(t) = \frac{1}{T}\int_0^T dt v_\theta f(v_\theta, p, v_z, r, z, t), \tag{34}$$

where T is the length of simulation. We typically run the code with 8192 particles for at least 4×10^4 time steps, which correspond to approximate 10^2 axial bounce periods.

Figure 9 shows the flux contours of Eq. (31). Here $2z_0 = 160$, $a = 8.5$ in the normalized code units. Then the magnetic field is relatively weak so that α (defined as $a\omega_c/v_0$) is approximately 5, particle orbits are largely of the betatron type. An example of such an orbit is shown in Fig. 10(a), where dots indicate particle position at regular time intervals in (r,z) coordinates. As discussed in Sec. II, with an increased magnetic field so that α is somewhat greater than 10, particle orbits bifurcate into two radial regions surrounding an inaccessible region. In the three dimensional problem of the present simulation we typically observe a figure shown in Fig. 10(b). The figures in Figs. 10(a) and 10(b) are obtained in runs with $\nu = 0$. Figure 9(c) shows the same particle under the same conditions as in Fig. 10(b) except for the collision frequency $\nu T = 4$.

We would like to address the following issues:

(i) Current profile: As discussed in the previous section, the radial current profile has a double peak in strong field cases ($\alpha \gtrsim 10$). In this section we study the two-dimensional (r,z) profile of the current formed with or without collisional drag effects.

(ii) Particle density profile: Although the current may cancel near the middle, the density is high in the central region.

(iii) Particle orbits: We shall study orbits that are bifurcated in the strong field case vs. orbits that are not. We shall investigate the extent in which particles with $p - av < 0$ can be contained, as this condition violates the ergodic assumption of the previous section.

(iv) Properties of confined particles. Do confined particles satisfy the conditions

$$p - av_0 > 0 (\nu = 0)$$
$$p(t) - av(t) < 0 (\nu \neq 0).$$

(v) Ergodicity: We shall investigate whether orbits are regular, chaotic, or somewhat in between. For a completely chaotic orbit, one obtains a constant density ($\times r$) profile in the accessible region of phase space, while if KAM barriers exists, even chaotic orbits do not fill in the $r-z$ density space uniformly. Only regular orbits give rise to curves on surface of section plots.

We shall shortly present some detailed results of the simulations. A summary of our conclusions to the above issues are as follows:

(i) Current profile. A hollow distribution begins to appear when $\alpha \gtrsim 10$. Then in the r, z space the high current region encircles the low current (or zero) current region. The peak of the fusion produced current density J_θ is $0.68 J_p$, where J_p is the peak of the plasma current (at the separatrix) for $\alpha = 5$ case and $J_\theta = 1.14 J_p$ for $\alpha = 16$. These cases were computed assuming 50-50 D-^3He background plasma at 100 keV ion temperature.

(ii) Particle density profile. The particle density does not have a hollow structure (even though the current density can be hollow). For smaller values of α the density profile is more peaked than for larger values of α.

(iii) Typical particle orbits are shown in Fig. 10.

(iv) Confinement properties. Particles with $p < 0$ are immediately lost from the system. Less than a quarter of the particles are directly lost for $\alpha \cong 16$. As α becomes smaller, the fraction of confined fusion protons decreases.

All unconfined particles (for case $\nu \neq 0$, $\nu T = 1$) satisfied $p(t) - av(t) < 0$ as they must from dynamical considerations. Not all confined particles satisfy $p - av_0 > 0$ (in the $\nu = 0$ case). For example, about 17% of confined particles did not satisfy this condition for $\alpha \simeq 9$. However, all confined particles satisfy $p(t) - av(t) > 0$ for the $\nu \neq 0$, $\nu T = 1$ case. The stochasticity properties of the orbits of confined particles is characterized as: the larger α, the larger the fraction of the orbits of confined chaotic particles. In case of $\alpha \cong 16$ a majority of particles are chaotic. However, most particles do not exhibit complete ergodicity as the phase space density is not uniformly filled even for the large α cases.

The fraction of particles that are confined is determined at the end of the run. As we generate particles uniformly within $\psi > 0$, we assign different weights w_j to different particles j according to density $n(\mathbf{x}_j)$, where $\mathbf{x}_j$ is the j-th particles original position. The density n is given according to Eq. (32). In the early time ($\sim 10^3$ steps) we run the code

without the slowing down due to collisions so that we can quickly eliminate particles that contact the separatrix which leads to direct loss. Then we turn on the collisional drag. After 10^3 steps, until the end of the run we lose a very small fraction of particles. Therefore, it is reasonable to assume that by the end of the run most of the particles that remain confined would be confined indefinitely. In Fig. 6 we have inserted crosses to indicate the fraction of particles that remain confined at the end of the run with the appropriate weighting according to the initial equilibrium density. These are for $\alpha = 5$, 10, and 16 cases. While the theoretical curve is obtained based on the ergodicity assumption and the one dimensional model, the simulation points are generated by the code in an elongated equilibrium with a finite aspect ratio as given by Eq. (31). Both theory and simulation agree qualitatively with each other.

Possible reasons for slight errors are as follows: (i) while theory assumes ergodicity, simulation shows that this assumption does not hold well, as we shall see below. This tends to have the simulation points above the theoretical curve. (ii) the finite aspect ratio two dimensional equilibrium has a larger relative area to the low density region than the one dimensional code. Thus, the two dimensional codes predict more relative fusion production in the low density region than the 1-d code, leading to more losses than the 1-d code. This tends to make the simulation points fall below the theory curve. The actual results in Fig. 6 indicate that the second factor is apparently stronger than the first.

Figure 11 shows the comparison of the theoretical fusion current calculation of the previous section and the corresponding simulation result for $\alpha = 5$ and 16 cases. What is shown is the nondimensionalized integral $I_H(r)$ defined in Eq. (18) and the corresponding fusion current is given by Eq. (17). For smaller values of α the current profile has a single peak toward 60-70% of the separatrix radius (a). For a large value ($\alpha \simeq 16$) it has a double peak with one at $r < a/2$ and the other near $r \sim 0.9a$. Both theory and simulation exhibit qualitative agreement but a quantitative disparity. In Fig. 11(a) the simulation result is larger than the theory result. We shall discuss possible reasons below. In Fig. 11(b) there appears more ragged structure in the simulation than in the theory, which might possibly arise from statistical fluctuations or because the finite drag to axial bounce time of the simulation is too large. The radial structure is hardly seen in cases with $\nu = 0$, perhaps because in this case particles do not slow down. It may be that the slow particles, which

have a low bounce frequency do not exhibit the phase cancellation that they would at smaller slowing down rates.

Figures 12, 13 and 14 corresponding to $\alpha = 5$, 9, and 16 respectively, show: the radial profile of fusion particle density in panel (a); the (r, z) contours of fusion current in panel (b); and the radial profile of the fusion current J_θ in panel (c). For the $\alpha = 5$ case the current has a single peaked radial structure. For the $\alpha = 16$ case, confined particles exist in larger radial positions and there appears a complete encirclement of a low (current) region by a high current. The $\alpha = 9$ case is on the verge of establishing the hollow current profiles that are typical of the larger α cases, as in $\alpha = 16$.

We studied the stochastic nature of the orbits of fusion produced particles with two distinct statistical approaches. In the first method the surface of section of particle orbits at $z = 0$ is constructed and the structure of the surface of section appearing in this plot is studied. For a given confined particle, the orbit intersects with the $z = 0$ surface many times during a computational run. Our runs have typically 10^2 intersections through $z = 0$. The radial position of the n-th section r_n and its associated velocity $\dot{r}_n$, or alternatively, r_n and r_{n+1} provide phase space of the orbit at the $z = 0$ section [The Poincare return map or Lorentz plot[16] (r_n, r_{n+1})]. The map (r_n, r_{n+1}) or the phase space plot $(r_n, \dot{r}_n)$ for various n's provides the map. From these maps one can study the regularity or diffusive structure of the orbits. Figure 15 shows an example of the Lorentz map and the phase space map for the same and is an example of a relatively regular orbit. An example of a surface of section plot of an ergodic orbit is shown in Fig. 15(d).

In principle, precise criteria can be used to give a quantitative measure to the degree of stochasticity of an orbit, for example the determination of the Hausdorff dimension[16] or alternative definitions for an attractor dimension.[17,18] In our investigation the stochasticity criterion is only qualitatively determined from visual inspection of the surface of section plot. For this purpose the Hausdorff dimension, which is defined as

$$D_H = \lim_{\varepsilon \to 0} \ell n \; N(\varepsilon)/\ell n(1/\varepsilon) \tag{35}$$

with ε being the width of phase space "cube" and $N(\varepsilon)$ is the number of "cubes" covering the "volume", is what is inferred from intuitive inspection. From visual inspection we infer if the orbit on the surface of section is a curve, whereupon $D_H = 1$, while if the orbit fills

an area in the phase space, then we infer $D_H = 2$. In the former case the orbit is regular and in the latter case the orbit is chaotic. Thus , if the attractor is diffuse, the orbit is chaotic, while if the attractor is on or almost on a curve, the orbit is regular. For the Poincare map, let

$$r_{n+1} = f(r_n), \tag{36}$$

then

$$r_{n+s} = f^s(r_n). \tag{37}$$

We note that the larger s, the more sensitive our surface of section technique is for exhibiting chaotic behavior. For example weak stochasticity may appear regular with the $s = 1$ test because the area being filled is small while the $s = 4$ case clearly exhibits stochasticity.

Table 1, which classifies whether the contained particles are regular or chaotic, is determined using $s = 1$ or $s = 4$. For the $\alpha = 5(B = 2.8$ Tesla, $a =$ (1 meter)), all confined particles in the simulation are regular regardless of choice of s ($s = 1$ or 4). For $\alpha = 9(B = 5$ Tesla, $a = 1m)$ $D_H(f^4)$ and $D_H(f^1)$ are different for a fair number of particles as it is for $\alpha = 16$ (9 Tesla, $a = 1m$) case. This result illustrates the greater sensitivity of the $s = 4$ test. Overall, less particles are regular, as α increases.

The second approach is to study the phase space density of a given orbit. If the particle follows an ergodic orbit as postulated in the previous section, the number of particles, dN, in the phase space volume element $dpvdv$ is

$$dN(\theta, r, z, v_z) = F(p, v)\frac{d^3r d^3v}{dpvdv} = F(p, v)\frac{d\theta dr dz dv_z}{\left[v^2 - \frac{1}{r^2}(p - U)^2 - v_z^2\right]^{1/2}}, \tag{38}$$

where $F(p, v)$ is a function of only p and v. After integrating Eq. (38) over θ and v_z, we obtain

$$dN(r, z) = 2\pi^2 F(p, v) dr dz. \tag{39}$$

This is independent of r and z for a given particle orbit. Our simulation examines the validity of the completely ergodic assumption by checking if Eq. (39) is indeed obtained. Figure 16 shows density contours for three representative particle orbits in r, z for $\alpha = 5$, 9 and 16 cases, respectively. As is clear for all these figures, the density is not uniform, and thus inconsistent with Eq. (39). In particular the densities near the turning points of the

orbit are very much higher than other areas. We note that a regular orbit would give rise to a divergent density at the turning point. Thus, we have another indication that some orbits appear closer to regular orbits.

If an orbit is completely ergodic, the relative occupation number, $\mathcal{N}$, at a given (r, z) point would be independent of position if (r, z) is an accessible point. However, if orbits are not ergodic, then for a given initial condition, the relative occupation number generated by the trajectory of the motion varies with different points (r, z). One can then define the area in the (r, z) plane covered per unit occupation number. For a fully chaotic system all the area is covered for one occupation number. With partial ergodicity, the covered area is a broader function of occupation number, with less ergodicity corresponding to a broader function of $\mathcal{N}$. This function can be examined numerically by dividing (r, z) into square bins, and then plotting the number of bins, $f(\mathcal{N})$, that have a given relative occupation number (to within a specified uncertainty $\Delta\mathcal{N}$. Figure 17 shows that $f(\mathcal{N})$ has a peak near $\mathcal{N} = 3$ for $\alpha = 16$, and $\mathcal{N} = 4$ for $\alpha = 9$ and 5 cases. As α decreases, the distribution of $f(\mathcal{N})$ is more spread. This indicates that the smaller α, the less the ergodicity.

We have noted that the complete ergodicity assumption is not strictly valid, yet the general comparison of the currents calculated in the semi-analytic theory and the particle simulation method compare favorably with each other. Part of the reason is that currents are integrals, which smooth over the discrepancies between different results in the orbit calculations. It even appears that specifying the energy and angular momentum of an orbit puts a sufficient restriction of the phase space of the orbit, that currents produced by different possible distributions of a third variable (e.g., an additional action variable) do not qualitatively change the mean current density profile that can be produced.

IV Self-Consistent Magnetic Field and Reactor Parameter

To calculate the self-consistent magnetic field with a given background pressure profile and a given fusion product current profile, we need to solve the equation

$$(\nabla \times \mathbf{B})_\theta = \frac{\partial^2 \psi}{r \partial z^2} + \frac{\partial}{\partial r} \frac{1}{r} \frac{\partial \psi}{\partial r} = 4\pi (J_p + J_f)$$

where $\mathbf{B} = \nabla\psi \times \nabla\theta$, and J_p and J_f are the fusion product currents which are in the θ-direction. The plasma current is determined from the pressure $P(\psi)$,

$$J_\theta = r\frac{\partial P(\psi)}{\partial \psi}$$

and the fusion product current is determined from Eq. (13),

$$J_f = q\int d^3v v_\theta f.$$

We rescale variables so that $\tilde{U} = q\psi/Mcav_0$, $x = r/a$ with a the separatrix radius and v_0 the birth speed of the fusion product. We use Eqs. (24) and (25) for the pressure profile P. Rather than solving the exact slowing down distribution, we use the model distribution given by Eqs. (17) and (22), as then the explicit dependence of J_f on $\tilde{U}$ is known and we have observed that this model is accurate. We then find we need to solve the equation

$$\begin{aligned}&\frac{a^2}{x^2}\frac{\partial^2\tilde{U}}{\partial z^2} + \frac{1}{x}\frac{\partial}{\partial x}\frac{1}{x}\frac{\partial\tilde{U}}{\partial x}\\ &= -4\alpha\left[\exp\left(-\sigma\frac{\tilde{U}}{U_{\max}}\right) + \frac{8f}{x}I_M(\tilde{U})\frac{\tilde{U}_{\max}}{\sigma}\Big(1-\exp(-\sigma)\Big)\right]\end{aligned} \tag{40}$$

with

$$I_M(\tilde{U}) = \frac{1}{4}\left[1-\frac{(\tilde{U}-1)^2}{x^2}\right]\theta\left[x^2-(\tilde{U}-1)^2\right] \tag{41}$$

and

$$f = \frac{\lambda g}{4}\frac{E_F}{T_e}\frac{n_{0e}\overline{\sigma v_i}}{\nu_0}\frac{n_{0e}T_e}{\sum_j n_{0j}T_j} \tag{42}$$

where n_{0j} and T_j are the density and temperature of background species j consisting of electrons of ion constituents, $g = n_{0D}n_{03He}/n_{0e}^2$ and the subscript "0" refers to quantities at the magnetic null. All the other quantities have been defined in Sec. II. In particular α, which is proportional to the pressure gradient, is determined from Eqs. (24) and (25).

Equation (40) is a nonlinear equation that is solved in the highly elongated limit by iteration (we neglect the $\partial^2\tilde{U}/\partial z^2$ term). Then, for a given α, σ, and f we guess $\tilde{U}_{\max}$ and $\frac{\partial\tilde{U}}{\partial x}(x=1)$, and integrate the equation from $x = 1$, where $\tilde{U} = 0$, to $x = 0$, where we demand $\tilde{U} = 0$. After several iterations, solutions are found.

The physical solutions relate $\frac{\partial \tilde{U}}{\partial x}(x=1)$ to $\tilde{U}_{\max}$. To convert to the actual external magnetic field, B_0, we note that

$$\frac{qB_0}{Mv_0c} \equiv \frac{\omega_{ci}a}{v_0} = \left|\frac{\partial \tilde{U}}{\partial x}(x=1)\right| \tag{43}$$

$$\frac{q\psi_{\max}}{M} = v_0 a \tilde{U}_{\max} \tag{44}$$

where q and M are the charge and mass of a proton, and v_0 the speed of a 15 MeV proton. We note that at fixed temperature the primary parameter in establishing f is g, the factor determining the mixture $^3He - D (g = \frac{n_{He}n_D}{n_0^2} = \frac{n_{He}n_D}{(2n_{He}+n_D)^2} \leq \frac{1}{6}$ when $2n_0T_e \equiv \frac{B_0^2}{8\pi}$ is held fixed). If for the example we choose $T_e = T_i = 100$ keV and $E_F = 15$ MeV, then $\overline{\sigma v_i} = 1.5 \times 10^{-16}\text{cm}^3/\text{sec}$, $n_0/\nu_0 = 10^{15}\text{cm}^{-3}\,\text{sec}$, we find

$$f = \frac{g}{4}\frac{\lambda E_F}{T_e}\frac{n_0\overline{\sigma v_i}}{\nu_0}\frac{n_0T_e}{\sum_j n_{0j}T_j} \approx 2.81\lambda g.$$

Thus, for $T = 100$ keV and $\lambda = 0.6$, f is physically limited to $f \lesssim 0.28$ but higher values of f are possible at higher plasma temperatures, to about $T = 300$ keV. We note that for $\alpha = 15$, that the peak fusion particle current density is comparable to the peak background plasma current density.

In Figs. 18 we present the results of equilibrium studies. We choose three background pressure profiles $\sigma = 0.1, 1, 2$, and examine the effect of the equilibrium. In Fig. 18(a) and (b) we show $\tilde{U}_{\max}$ vs. $\left|\partial\tilde{U}(x=1)/\partial x\right| \equiv \alpha_{\text{eff}}$ for different values of $f (f = 0.0,\ 0.1,\ 0.2,\ 0.4)$. For the same pressure profile, we observe that for small normalized magnetic fields where there is only one spatial region of confinement for the fusion products the normalized magnetic flux increases with increasing f. However, at higher fields where there are two spatial regions of confinement, the magnetic flux decreases, with increasing f.

We also plot the fraction of trapped fusion products, h, as a function of normalized magnetic field in Figs. 19 and normalized magnetic flux in Figs. 20. One observes that the trapping function depends primarily on the enclosed magnetic flux almost independent of any other parameter. At low fields, finite f improves fusion product confinement slightly, while finite f at higher relative magnetic fields decreases the fusion product confinement slightly.

In Figure 21 we plot the relative reactivity defined as

$$R_F = \frac{64\pi^2}{B^4(x=1)}\int_0^1 P^2(x)dxx$$
$$= \frac{64\alpha^2\tilde{U}_{\max}^2}{[\partial U(x=1)/\partial x]^4}\int_0^1 dxx\left[1-\exp\left(-\frac{\sigma\tilde{U}}{\tilde{U}_{\max}}\right)\right]^2. \quad (45)$$

The relative reactivity would be unity if $\sigma \to \infty$ and $f = 0$. The R_F is a measure of fusion power density for a given magnetic field. We see that the R_F improves with increasing σ, but that there is a substantial decrease in the R_F factor with increasing f. This decrease must be accounted for in design assessment if fusion products are retained. The reason for the decrease in reactivity is that if f increases for fixed plasma radius and external magnetic field, the plasma pressure must decrease in order to accommodate added pressure of the fusion component. This is reflected in Fig. 22 where

$$\beta \equiv 8\pi P(\tilde{U}=\tilde{U}_{\max})/B^2(x=1) = \frac{8\alpha\tilde{U}_{\max}(1-\exp(-\sigma))}{\left|\frac{\partial\tilde{U}}{\partial x}(x=1)\right|^2}$$

is plotted for different values of σ, f and $\left|\frac{\partial\tilde{U}}{\partial x}(x=1)\right|$.

Finally, we plot in a single particle synchrotron parameter which measures the relative rate of single particle synchrotron emission (without reabsorption taken into account). We define

$$SYN = \frac{2}{B^2(x=1)P_{\max}}\int_0^1 dxxP(x)B^2(x)$$
$$= \frac{2}{[1-\exp(-\sigma)]\left(\frac{\partial\tilde{U}(x=1)}{\partial x}\right)^2}\int_0^1 \frac{dx}{x}\left(\frac{\partial\tilde{U}(x)}{\partial x}\right)^2\left[1-\exp\left(\frac{-\sigma\tilde{U}(x)}{\tilde{U}_{\max}}\right)\right] \quad (46)$$

and note that $SYN = 1$ for a uniform low beta plasma in a constant magnetic field. We see that the relative single particle synchrotron radiation is substantially suppressed from this uniform estimate for all profiles. In Fig. 23 we show SYN for various values of f ($f = 0.0$, 0.1, 0.2, and 0.4) for different pressure profiles designated by $\sigma(\sigma = 0.1$ and 2.0). We see that the presence of fusion products produce moderate changes in the bare particle synchrotron emission.

To take into account radiative reabsorption we evaluate an interpolation formula (obtained from an analysis of J. Dawson[19]) that attempts to take into account radiative

reabsorption in an inhomogeneous medium. The formula is correct in the extreme limits of black-body and optically thin single particle emission. The radiated power per unit length (cgs units) is given by,

$$P_S(Abs) = 2\pi a(1-r)\int_0^\infty d\omega I_{bb}(\omega)\left[1-\exp\left[\frac{-a}{(1-r)}\int_0^1 dx x\kappa(x,\omega)\right]\right] \qquad (47)$$

where

$$\begin{aligned}
\kappa(x,\omega) &= \frac{\varepsilon(\omega,ax)}{I_{bb}} \quad , \quad I_{bb}(\omega) = 4\pi T_e\omega^2/c^2 \\
\varepsilon(x) &= \frac{1}{8\pi^{3/2}}\frac{M_e^2c^4}{T_e}\omega_{pe0}^2\omega^{1/2}\omega_{ce}^{1/2}\hat{n}(x)b^{1/2}(x) \\
&\times \int_0^\infty \frac{d\gamma}{\gamma}\left[\frac{\gamma-1}{\gamma+1}\right]^{\gamma\omega/\omega_{ce}b(x)}\exp\left[\frac{2\omega}{\omega_{ce}b(x)}+\frac{(1-\gamma)M_ec^2}{T_e}\right] \\
r &\equiv \text{reflectivity factor} \\
\omega_{pe0}^2 &= \frac{4\pi n_0e^2}{M_e}, \quad \omega_{ce} = \frac{eB_{\max}}{M_ec}, \quad T_e \equiv \text{electron temperature in ergs} \\
b(x) &= \frac{B(x)}{B_0} = \frac{\left|\frac{\partial\tilde{U}(x)}{\partial x}\right|}{\left|\frac{\partial\tilde{U}(x=1)}{\partial x}\right|} \\
\hat{n}(x) &= \frac{n(x)}{n_0(x)} = \left[1-\exp\left(-\sigma\frac{\tilde{U}(x)}{\tilde{U}_{\max}}\right)\right]\Big/\left[1-\exp(-\sigma)\right].
\end{aligned}$$

The power radiated per unit axial length in a uniform field B_0 by a homogeneous plasma of density n_0 and radius a is

$$P_S(\text{bare}) \doteqdot \frac{4e^4B_0^2T_en_0\pi a^2}{3M_e^3c^5}\left(1+T_e/M_ec^2\right).$$

Hence, the relative power emitted relative single power emitted of a homogeneous plasma of radius a, $P_S(\text{rel})$, is

$$P_S(\text{rel}) = P_S(\text{Abs})/P_S(\text{bare}).$$

We show our results for $P_S(\text{rel})$ in Table II when $g = 1/6$. For simplicity we have only examined the $f = 0$ case. Our results are much more optimistic than that published by Dawson,[19] who apparently made a numerical error in presenting his final results. For example we find for $T = 100keV$, $n_0 = 0.6\times10^{15}\text{cm}^{-3}$, $B = 50kg$, that $P_S(\text{rel}) = .05$ for

$a = 100$cm, whereas in Ref. 19 $P_S(\text{rel}) \approx 1$ is inferred. We also gain from the exclusion of magnetic field in the interior of the plasma as Table II shows even lower values of $P_S(\text{rel})$ are obtained. Only the $f = 0$ case has been investigated.

V Conclusions

We have investigated the effect of charged fusion products on the current flow of an FRC. This investigation is complicated by the fact that particle orbits are complex as the particle motion does not in general satisfy the limiting assumptions used in developing small Larmor radius theory or betatron orbit theory. As a result in our investigation, we have integrated particle orbits exactly, and compared the result with the assumption that particles reach all regions of accessible space at constant energy and angular momentum with equal probability. We have found that in detail most particles do not fulfill the ergodicity assumption. Nonetheless, the resulting charged fusion product current and other global quantities calculated by the two methods give qualitatively similar results. Hence, meaningful results will be obtained by invoking the assumption of maximum ergodicity of the charged particle orbit.

We have developed a new method of solution of the Fokker-Planck drag equation when pitch angle and energy scattering of particles is unimportant, which is applicable to fusion protons of the D-^3He reaction during most of its slowing down time. Under the assumption of maximum ergodicity, this combined numerical and analytic method can be implemented to take into account exact geometry. We have explicitly performed calculations for highly elongated FRC geometries.

We find that the results of the detailed slowing down model for the current and the fusion product trapping fraction is closely reproduced by a monoergetic fusion product model that is otherwise self-consistent. This simpler current model enables one to readily calculate the self-consistent arbitrary Larmor radius (of the fusion product) equilibrium in the highly elongated limit. Of course one assumes a given pressure profile for the background plasma whose current is given by the ideal MHD equations.

As one traps fusion products, the characteristics of the system must change and this aspect needs to be taken into account in applying the curves we have obtained. If we assume

that the radial size of the plasma and the external magnetic field do not change, then Fig. 18 shows that the enclosed magnetic flux changes by as much as 25% as fusion products build up. The size remains constant if there is a physical limiter (or divertor) present that determines the radius. However, it is more difficult to justify that the magnetic field will remain constant. One should note that as the fusion-product containment increases, the plasma will swell radially, unless a larger external magnetic field is imposed to keep the same dimensions. The surrounding inductive and resistive characteristics will also affect the magnetic field evolution. Stabilizing considerations may also be an important factor that determines the flexibility on how much radial dimensions can change during the evolution of a discharge. This is because wall stabilization, which may require fixed boundaries, can be an important component in establishing a stable discharge. Thus, the details of how parameters specifically evolve from the onset of ignition to steady state operation, is a problem that needs careful further study. Nonetheless, despite these complications, we compare systems with the same external magnetic field and the same separatrix radius.

The enclosed magnetic flux is the single most important parameter in determining what fraction of the charged fusion products are retained. The parameter almost uniquely determines the trapping fraction as we have shown (see Fig. 8) that the trapped fraction is insensitive to the shape of the pressure profile. Thus, profiles that contain less magnetic flux, trap a smaller fraction of the charged fusion products. In smaller systems, where the trapped fusion products are in betatron orbits, the magnetic flux in the plasma increases as the number of contained fusion products increase, at constant external magnetic field and constant separatrix radius. On the other hand, in large systems, where the topology of the orbits of charged fusion products begin to resemble the orbits of small Larmor radius theory, the magnetic flux in the plasma decreases with increasing trapped charged-fusion products at constant magnetic field and constant separatrix radius. Thus a small system, with a given radial size and external magnetic field, exhibits a larger fraction of fusion product containment if the fusion-product fraction is taken into account, than would be predicted if the fusion-products were ignored in the equilibrium. For large systems, the trapping fraction for the fusion products decrease relative to what would be calculated without accounting for the current derived from fusion product containment.

With the charged fusion products taking up part of the pressure, the beta of the

background decreases (at constant temperature and external magnetic field this means a decrease of the background density), and a substantial decrease in the fusion produced power results.

To illustrate a specific case we consider a pressure profile characterized by $\sigma = 0.1$ and a rise of the trapped fraction of fusion products from $f = 0$ to $f = 0.2$. The reactivity, R_F, at larger α_{eff} then decreases from 0.55 to 0.25 (from Fig. 20) while the central density (from Fig. 21) decreases a factor 0.65 of the value when fusion products are not retained. To consider this affect on the fusion power per unit volume produced, we choose as an example $T = 100$ keV where $\overline{\sigma v_i} = 1.5 \times 10^{-16}\text{cm}^3\,\text{sec}$. The fusion power, P_F, produced per unit volume is then

$$P_F = n_{D0} n_{He_0}^3 \overline{\sigma v_i} E_F R_F = 450 N_{D0}(15) N_{He0}(15) R_F \text{ Watts/cm}^3 \tag{48}$$

where $E_F \equiv 19$ MeV $\equiv$ energy of proton and alpha fusion products, n_{D0} and $n_{^3He0}$ are the densities of deuterium and Helium-3 at the magnetic null in units of cm^{-3} and $N_{D0}(15)$ and $N_{He0}(15)$ the corresponding densities in units of 10^{15}cm^{-3}, and R_F is the fusion reactivity defined in Eq. (45). Let us consider density parameters that optimize the power produced. For $f = 0$ we have from equilibrium and charge neutrality,

$$\frac{B^2}{8\pi} \equiv 2n_0 T = (n_{e0} + n_{D0} + n_{^3He})\, T, \quad n_{e0} = n_{D0} + 2n_{^3He}.$$

Then maximizing $n_{D0} n_{^3He}$ with n_0 constant, gives

$$n_{e0} = 7/6 n_0, \quad n_{^3He} = n_0/2, \quad n_{D0} = n_0/2 \quad \max\ n_{D0} n_{^3He0} = n_0^2/6.$$

The equilibrium condition give $n_0 = 1.25 \times 10^{15}\text{cm}^{-3}$. Thus, the optimal average power per unit volume produced, with $R_F = 0.55$ is

$$P_f = 64 \text{ watts/cm}^3 \qquad \text{(no fusion product containment)}.$$

Now, with $f = 0.2$, $R_F = 0.25$ as indicated in Fig. 20. The decreased value of R_F takes into account that the absolute density at the center has changed. However, maximum power will still require the same density mixture as the $f = 0$ case. Thus substituting into Eq. (48) the same values of $N_{d0}(15)$ and $N_{He}(15)$ as the $f = 0$ case, but using the appropriate value of R_F, we obtain,

$$P_f = 25 \text{ watts/cm}^3 \qquad \text{(with fusion product containment)}.$$

For a reasonable sized fusion reactor burning D-^3He, we find that the fusion power generated is substantially more than the synchrotron emission, even without wall reflection and for a relatively diffuse profile ($\sigma = 0.1$). Specifically, the synchrotron power radiated per unit volume, P_s, is given by (in cgs units)

$$\begin{aligned} P_s &= \frac{4e^4 n_{e0} B_0^2}{3c^5 M_e^5} T_e (1 + T_e/M_e c^2) P_S(\text{rel}) \\ &= 3.17 \times 10^3 B_0^2(5) N_{e0}(15) \frac{T_e}{M_e^2} \left(1 + \frac{T_e}{M_e c^2}\right) P_S(\text{rel}) \frac{\text{watts}}{\text{cm}^3} \end{aligned}$$

where $B_0(5)$ is the edge magnetic field in units of 10^5 gauss, and $P_S(\text{rel})$ is defined in Eq. (47). Now choosing $N_{e0}(15) = 1.45$, $B_0(5) = 1$, $\frac{T_e}{M_e c^2} = 0.2$, the separatrix radius $a = 100$ cm, the plasma profile parameter $\sigma = 0.1$, and the wall reflectivity $r = 0$, we have from Table I that $P_S(\text{rel}) = 3.4 \times 10^{-3}$. Hence, for this use the average synchrotron power radiated per unit volume is

$$P_s = 3.2 \text{watt/cm}^3,$$

which is an order of magnitude less than the fusion power produced. When fusion particles are retained, self-consistent equilibrium conditions demands that the central density for the $\sigma = 0.2$ profile with $f = 0.2$, lowers to $N_{e0}(15) = 0.812$ (see Fig. 21 where the central beta is given, so that the central density is found when using $T = 100$ keV and $B_0 = 10^5$ kg). To evaluate $P_S(\text{rel})$ we have assumed that the magnetic field profile does not change from the $f = 0$, $\sigma = 0.1$ case (so that we can use analytic magnetic fields) and we find for $a = 100$ cm

$$P_S(\text{rel}) = 4.5 \times 10^{-3}.$$

Thus, the estimate of the radiated synchrotron power per unit volume, when fusion products are retained, is

$$P_s = 2.8 \text{ watt/cm}^3.$$

This radiated power is still ~ 0.1 of the fusion power produced.

We also observe from Table II that synchrotron losses can be further reduced when wall reflectivity is taken into account and if the background pressure profiles can be made steeper corresponding to larger σ. Thus, synchrotron radiation loss should not be an important factor of a D-^3He FRC, at least in operation in mixtures that maximizes the

fusion power output. Synchrotron radiation may be a factor in mixtures lean in deuterium (this is of interest in cycles that suppress neutrons from D-D reactions). However, even in this case, moderate improvements from wall reflectivity and steeper profiles, should make such operation feasible with respect to the parasitic losses from synchrotron radiation.

We now consider the advantages of retaining or losing the charged fusion products. We first of all note that the loss of all charged fusion products, together with efficient direct conversion and plasma heating can have some significant advantages. These include:

(1) Configurational Stability: It is known that an FRC is theoretically MHD unstable and the observed experimental stability may be due to finite Larmor radius effects. As a result it may be difficult to scale-up an FRC, so it may be difficult for α_b, the ratio of the plasma radius to the Larmor radius (of the background plasma) at the separatrix, to be as large as what is needed in a reactor that retains charged fusion products. For example, in present-day experiment, $\alpha_b \approx 15$, while in a reactor we need $\alpha_b \approx 175$ (or $\alpha_{\text{eff}} \equiv$ plasma radius/fusion product Larmor radius at separatrix $= 15$). This is a large extrapolation and MHD stability problems may be severe in such large devices. However, a smaller FRC, where most of the fusion products are rapidly lost, with say, $\alpha_b \approx 50$, (or $\alpha_{\text{eff}} \approx 3.5$) may be large enough for good plasma confinement and small enough to allow for MHD instability.

(2) Efficient Direct Conversion: If the fusion products are promptly lost, they will emerge from the plasma with a sharply peaked energy. Hence, with expansion of the magnetic field, a peaked energetic ion beam can be produced, allowing for energy conversion efficiencies of perhaps 85%. We note however that the fusion products may indeed have a significant energy spread if the edge losses are due to rapid slowing down of fusion products on the cooler edge plasma. In this case, direct conversion, though possible, will be significantly less efficient. It is possible that means can be devised (e.g., through rf scattering[20]) to cause preferential loss of the fusion products out of the plasma, before their birth energy is significantly changed.

(3) Lack of Beam Microinstability: Retaining charged fusion products could make the system susceptible to microinstabilities driven by radial spatial gradients of the stored fusion products, particularly due to the excitation of Alfvén waves. Thus the prompt loss fusion products removes one significant instability drive.

(4) As we have observed, the partial pressure of the fusion products can reduce the reactivity of the plasma. By the direct loss of the fusion products, the reactivity of the plasma can be maintained at constant value.

The advantages of retaining the fusion products are as follows:

(1) Current drive: We have observed that an appreciable fraction of the plasma current can be supported by the charged fusion products if a viscosity mechanism arises to prevent radial electric fields from arising.

(2) Stability: There is experimental evidence and theoretical calculations that indicate that appreciable configuration stability can be achieved by using energetic current carriers. As the fusion products should respond in a manner appreciably different from an MHD fluid, some of the favorable stability properties of energetic particles may be achieved by retaining fusion products.

(3) Internal heating: Confined charged fusion products will allow self-sustaining ignition conditions without the complications of continuous external heating.

Much of the above factors need further study and successful implementation will depend on future results of experiments and more detailed theoretical studies. In the present paper, we have attempted a preliminary study of some of the issues in establishing a steady state FRC advanced fuel (D-^3He) reactor, particularly in regard to the role of the current from the charged fusion products in supporting the plasma and the importance of synchrotron radiation.

Acknowledgment

This work was supported by the U.S. Department of Energy contract #DE-FG05-80ET-53088, and by the Joint Institute of Fusion Theory Exchange Program.

References

1. N.C. Christofilos, in Proceedings of the Second U.N. International Conference on Peaceful Uses of Atomic Energy (United Nations, Geneva, 1958) Vol. 32, p. 279.

2. J.M Finn and R.N. Sudan, Nucl. Fusion **22**, 1443 (1982).

3. R.V. Lovelace, Phys. Fluids **22**, 542 (1979).

4. T. Ohkawa, Nucl. Fus. **10**, 185 (1970).

5. A. Reiman and R.N. Sudan, Comments on Plasma Physics & Cont. Fusion **5**, 167 (1979).

6. J.H. Hammer and H.L. Berk, Nucl. Fusion **22**, 89 (1982).

7. R.V. Lovelace, Phys. Rev. Lett. **35**, 162 (1985).

8. R.V. Lovelace, Phys. Fluids **18**, 723 (1976).

9. R.N. Sudan and P.K. Kaw, Phys. Rev. Lett. **47**, 575 (1981).

10. R.V. Lovelace, Phys. Fluids **22**, 542 (1979).

11. D.A. Larrabee and R.V. Lovelace, Phys. Fluids **23**, 1436 (1980).

12. J.M. Finn, Plasma Phys. **21**, 405 (1979).

13. J. Cary and J.S. Kim, Phys. Fluids **26**, 2167 (1983).

14. H.L. Berk and H. Weitzner, Phys. Fluids **24**, 1758 (1981).

15. M.J. Lebrun and T. Tajima, Bull. Am. Phys. Soc. **30**, 1463 (1985).

16. E.N. Lorentz, J. Atom. Sci. **20**, 130 (1963); see also A.J. Lichtenberg and M.A. Lieberman, Regular and Stochastic Motion (Springer-Verlag, New York, 1983).

17. R.H. Simoi, A. Wolf, and H.L. Swinney, Phys. Rev. Lett. **49**, 245 (1982).

18. P. Grassberger and I. Procaccia, Phys. Rev. Lett. **31**, 31 (1983).

19. J.M. Dawson, in *Fusion* (Academic Press, Inc., New York, 1981), Vol. I, Part B, p. 453.

20. S. Riyopoulos, T. Tajima, T. Hatori, and D. Pfirsch, Nucl. Fusion **26**, 627 (1986).

Stochastic Nature of Particle Orbits (Confined Population)

Case	Regular	Chaotic	Short-lived
2.8T	100%	0	0
5T			
(r_{n+1}, r_n)	67%	27%	7%
(r_{n+4}, r_n)	28%	68%	4%
9T			
$(r_{n+1} r_n)$	25%	59%	16%
(r_{n+4}, r_n)	5%	79%	16%

Table I: Classification of orbits for weak, moderate, and strong magnetic fields.

P_S (rel) $\times 10^3$

$B_{max} = 10^5$ Gauss $n_0 = 1.45 \times 10^{15}$ cm^{-3}

		σ=0.01			σ=1			σ=2			σ=4		
a(cm)	r	T=.1	T=.2	T=.3	T=.1	T=.2	T=.3	T=.1	T=.2	T=.3	T=.1	T=.2	T=.3
.01*	0	81.7	86.0	87.7	69.4	73.6	75.3	54.1	57.5	59.1	26.7	28.2	28.9
50	0	4.8	10.7	17.0	4.0	9.0	14.3	3.2	7.1	11.2	1.8	3.8	5.9
100	0	3.4	8.1	13.4	2.9	6.8	11.3	2.3	5.4	8.8	1.3	2.9	4.7
200	0	2.4	6.1	10.4	2.0	5.1	8.8	1.6	4.1	6.9	0.9	2.2	3.7
.01*	.9	50.1	63.4	71.0	42.3	53.8	60.5	33.0	41.9	47.3	16.7	20.8	23.3
50	.9	1.5	4.1	7.3	1.3	3.4	6.2	1.0	2.7	4.9	0.6	1.5	2.6
100	.9	1.0	3.0	5.5	0.9	2.5	4.7	0.7	2.0	3.7	0.4	1.1	2.0
200	.9	0.7	2.1	4.2	0.6	1.8	3.5	0.5	1.4	2.8	0.3	0.8	1.5
.01*	.99	24.6	38.4	48.6	20.7	32.4	41.2	16.3	25.3	32.1	8.6	12.8	16.1
50	.99	0.4	1.4	2.8	0.4	1.2	2.3	0.3	0.9	1.9	.18	0.5	1.0
100	.99	0.3	0.9	2.0	0.2	0.8	1.7	0.2	0.7	1.4	.12	0.4	.08
200	.99	0.2	0.7	1.5	0.2	0.6	1.2	0.1	0.5	.99	.08	0.3	.56

$B_{max} = 5 \times 10^4$ Gauss $n_0 = 0.362 \times 10^{15}$ cm^{-3}

		σ=0.01			σ=1			σ=2			σ=4		
a(cm)	r	T=.1	T=.2	T=.3	T=.1	T=.2	T=.3	T=.1	T=.2	T=.3	T=.1	T=.2	T=.3
.01*	0	90.6	91.1	90.9	77.1	78.1	78.3	60.1	61.2	61.5	29.6	29.9	30.1
50	0	6.6	13.9	21.2	5.6	11.7	17.9	4.5	9.2	14.0	2.5	4.9	7.3
100	0	4.8	10.7	17.0	4.0	9.0	14.3	3.2	7.1	11.2	1.8	3.8	5.9
200	0	3.4	8.1	13.4	2.9	6.8	11.3	2.3	5.4	8.9	1.3	2.9	4.7
.01*	.9	59.5	70.9	76.9	50.2	60.3	65.7	39.2	47.0	51.4	19.7	23.2	25.2
50	.9	2.1	5.5	9.6	1.8	4.7	8.1	1.5	3.7	6.4	0.8	2.0	3.4
100	.9	1.5	4.1	7.4	1.3	3.4	6.2	1.0	2.7	4.9	0.6	1.5	2.6
200	.9	1.0	3.0	5.6	0.9	2.5	4.7	0.7	2.0	3.7	0.4	1.1	2.0
.01*	.99	31.2	45.6	55.5	26.2	38.5	47.1	20.6	30.0	36.7	10.7	15.2	18.3
50	.99	0.6	1.9	3.8	0.5	1.6	3.2	0.4	1.3	2.5	0.3	0.7	1.4
.100	.99	0.4	1.4	2.8	0.4	1.2	2.4	.29	0.9	1.9	.18	0.5	1.0
200	.99	0.3	1.0	2.0	0.2	0.8	1.7	.19	0.7	1.4	.12	.38	.77

* The emission predicted for these values is about 0.7 of the true value because of the inaccuracy of the asymptotic synchrotron formula at low harmonic number.

Table II. List of the relative synchrotron loss rate P_s(rel) for plasmas of various radii a, wall reflectivity r, pressure profile parameters σ, temperature T (in units of $M_e c^2$), edge magnetic field B, and various central densities n_0.

Figure Captions

Fig. 1 Domain of D_1, D_2 and D_3 for $p_1 > p_2 > p_3$. The interior area to the solid curve bounds the accessible domain of p_1, the area between the two dotted curves is the accessible domain of p_2, while the area between the two dashed curves is the accessible domain of p_3. The outer most curve represents the separatrix.

Fig. 2 Solution of the equation

$$\frac{d(y/s)}{ds} + \langle \nu U \rangle / \langle \nu \rangle = 0$$

with initial conditions $s = 1$, $y = y_0$ with $U = \frac{\alpha}{2} x^2(1 - x^2)$ and $\nu \propto U$, for $\alpha = 5$ and 15.

Fig. 3 An example of flow arising from the removal of guiding centers that are otherwise uniformly distributed. The dotted curve represents an orbit on which there is zero particle occupation probability, while orbits (1) and (2) have equal occupation probability. Then at point (a) the opposing vertical fluxes cancel, while at point (b) there is a downward flux because of the absence of particle occupation to the right.

Fig. 4 Evaluation of $I_H(ax, z = 0)$ in the highly elongated limit. Figures (a)-(c) are for $\alpha = 5$, 10, and 15 respectively.

Fig. 5 Evaluation of $I_M(ax, z = 0)$ in the highly elongated limit. Figures (a), (b) and (c) are for $\alpha = 5, 10, 15$ respectively.

Fig. 6 Fraction of retained fusion proton product produced by an isothermal plasma in an elongated Hill's vortex equilibrium as a function of plasma size as measured by the parameter α, where $\alpha = r_{\text{sep}}/r_L$, with r_{sep} the separatrix radius, and r_L the Larmor radius of the charged fusion product at the plasma separatrix. The crosses are the retained fraction as observed in the numerical simulation calculation.

Fig. 7 Plot of $8U_{\max}/\alpha_{\text{eff}}$ vs. σ for equilibrium with pressure gradient $\partial P/\partial U \propto \exp\left[-\sigma \tilde{U}/\tilde{U}_{\max}\right]$.

Fig. 8 Fraction of retained fusion products, h, as a function of $\tilde{U}_{\max}$, for $\sigma = 0.0, 1.0$ and 2.0 for curves 1, 2 and 3 respectively.

Fig. 9 Equilibrium flux $\psi(r,z)$ used in simulation. The broken lines are for $\psi < 0$. The scale of z is 1/20 the scale of r. The figure r,z in the following are similarly compressed in the x-direction.

Fig. 10 Typical particle orbit in: (a) weak field ($\alpha = 5$), and (b) strong field ($\alpha = 16$) without collisions. The orbit in (a) corresponds to a betatron orbit, while the orbit in (b) corresponds to a bifurcated orbit. The particle orbit in (c) corresponds in an orbit with the same initial condition as the one in (b), but now with collisions.

Fig. 11 The normalized fusion current profile $I(r)$ as a function of the radius for (a) $\alpha = 5$ and (b) $\alpha = 16$. The thick curves are the simulation, while the thin ones are from theory. For the case (a) $\nu t_{\text{tend}} = 4$, where t_{end} is the end of the simulation run. For the case (b) we averaged over two samples: the first run with collisions present all the time and $\nu t_{\text{end}} = 4$, while the second run has the collisions turned on after $\nu t > 0.05$ and $\nu t_{\text{end}} = 2$.

Fig. 12 The density and current of fusion products for weak field ($\alpha = 5$); (a) the density n as a function of r; (b) the current equicontour lines in r,z plane; (c) the azimuithal current as a function of r.

Fig. 13 The density and current of fusion products for moderate field ($\alpha = 10$). (a), (b) and (c) are as in Fig. 12.

Fig. 14 The density and current of fusion products for strong field ($\alpha = 16$). (a), (b) and (c) are as in Fig. 12.

Fig. 15 Typical surface of section plots of fusion particles at the mid-plane of z. (a) and (b) are the Lorentz plot and the phase space plot of the same particle, which shows a regular orbit. (c) shows another Lorentz plot of a regular orbit, while (d) shows the Lorentz plot of an irregular orbit.

Fig. 16 Phase space density contours (weighted average) of typical confined particles for: (a) $\alpha = 5$, (b) $\alpha = 9$, (c) $\alpha = 16$.

Fig. 17 The statistics $f(\mathcal{N})$ of the phase space normalized densities of fusion particles at various accessible phase space points (bins). The solid line is for $9T(\alpha = 6)$, dotted line $5T(\alpha = 9)$, broked line $2.8T(\alpha = 5)$.

Fig. 18 Effect of trapped proton fusion products on the maximum contained magnetic flux $\tilde{U}_{\max}$. Figures (a) and (b) are for different pressure profiles measured by $\sigma = 0.1$ and 2 respectively. The x-axis is $\alpha_{\text{eff}} = r_{\text{sep}}/r_L$, the separatrix radius and r_L the Larmor radius of a 15 MeV proton. Curves 1, 2, 3 and 4 are for $f = 0.0$, 0.1, 0.2, and 0.4 respectively.

Fig. 19 Fraction of trapped proton fusion products, h, for various values of σ, and f as a function of α_{eff}. Figures 18(a) and 18(b) correspond to σ=.1 and 2 respectively. Curves 1-4 correspond to f=0.0, 0.1, 0.2 and 0.4 respectively.

Fig. 20 Fraction of retained fusion products, h, as a function of $\tilde{U}_{\max}$. Figures (a) and (b) are for $\sigma = 0.1$ and 2 respectively. The four curves for $f = 0.0$, 0.1, 0.2, and 0.4 can not be readily resolved.

Fig. 21 Relative fusion product reactivity (R_F) as function of α_{eff} for different values of σ and f. Figures (a) and (b) are for $\sigma = 0.1$ and 2 respectively. Curves 1-4 are for $f = 0.0$, 0.1, 0.2 and 0.4 respectively.

Fig. 22 Background plasma beta (plasma pressure at null/magnetic pressure at separatrix) as a function of α_{eff}. Figures (a) and (b) are for $\sigma = 0.1$, and 2 respectively. Curves 1-4 are for $f = 0$, 0.1, 0.2, and 0.4 respectively.

Fig. 23 The effect of pressure profiles and fusion products on the bare synchrotron emission. The pressure profiles are characterized by $\sigma = 0.1$ and 2.0, and the curves 1-4 are for $f = 0.0$, 0.1, 0.2, and 0.4 respectively.

Table Captions

Table I Classification of orbits for weak, moderate and strong magnetic fields.

Table II List of the relative synchrotron loss rate P_S(rel) for plasmas of various radii a, wall reflectivity r, pressure profile parameters σ, temperature T (in units of $M_e c^2$) edge magnetic field B, and various central densities n_0.

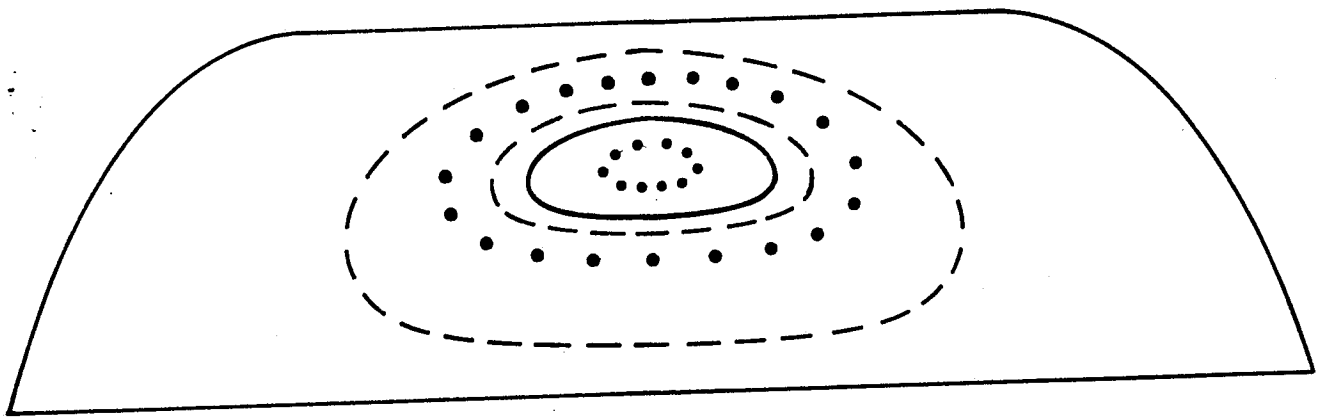

Fig. 1

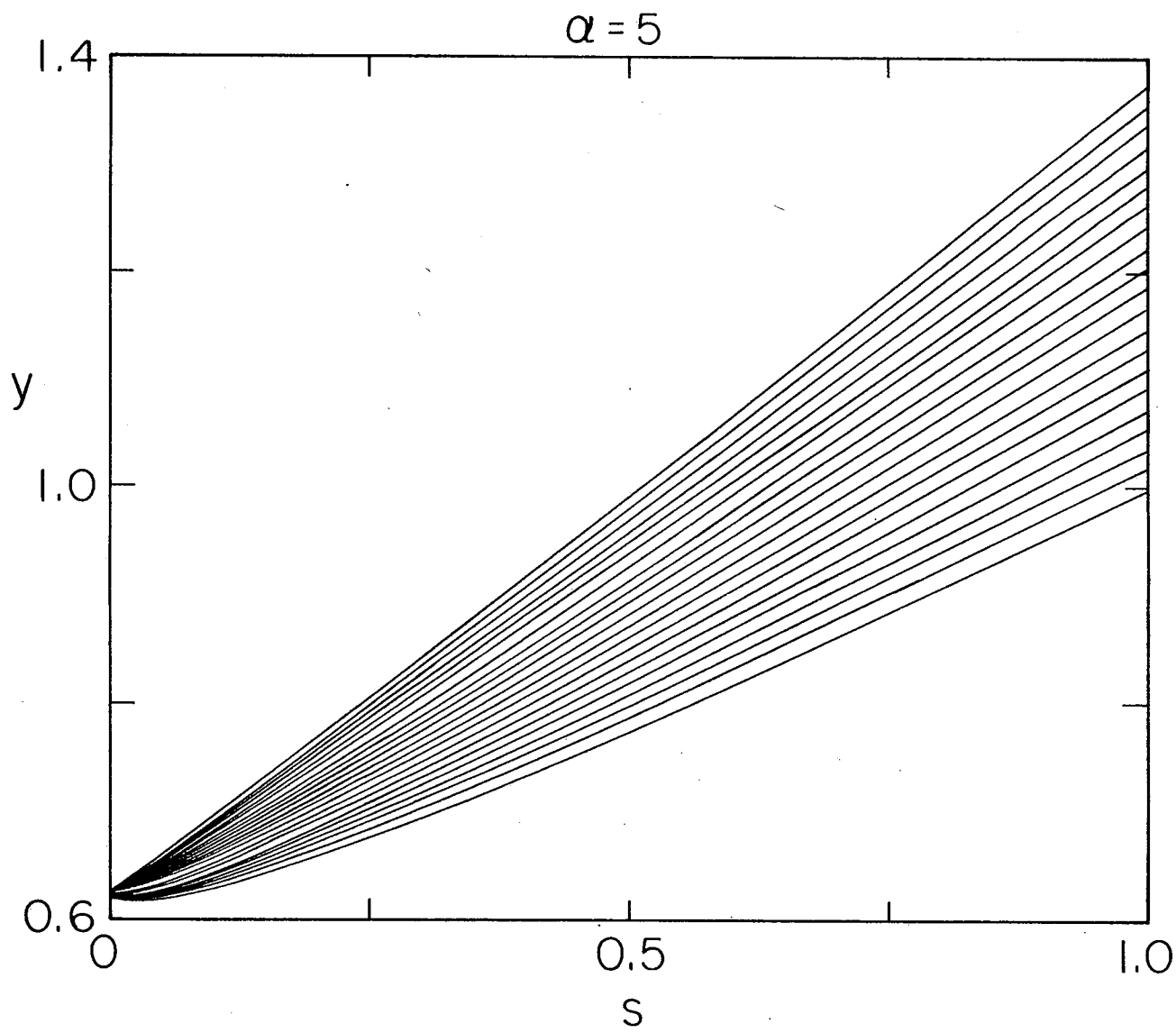

Fig. 2(a)

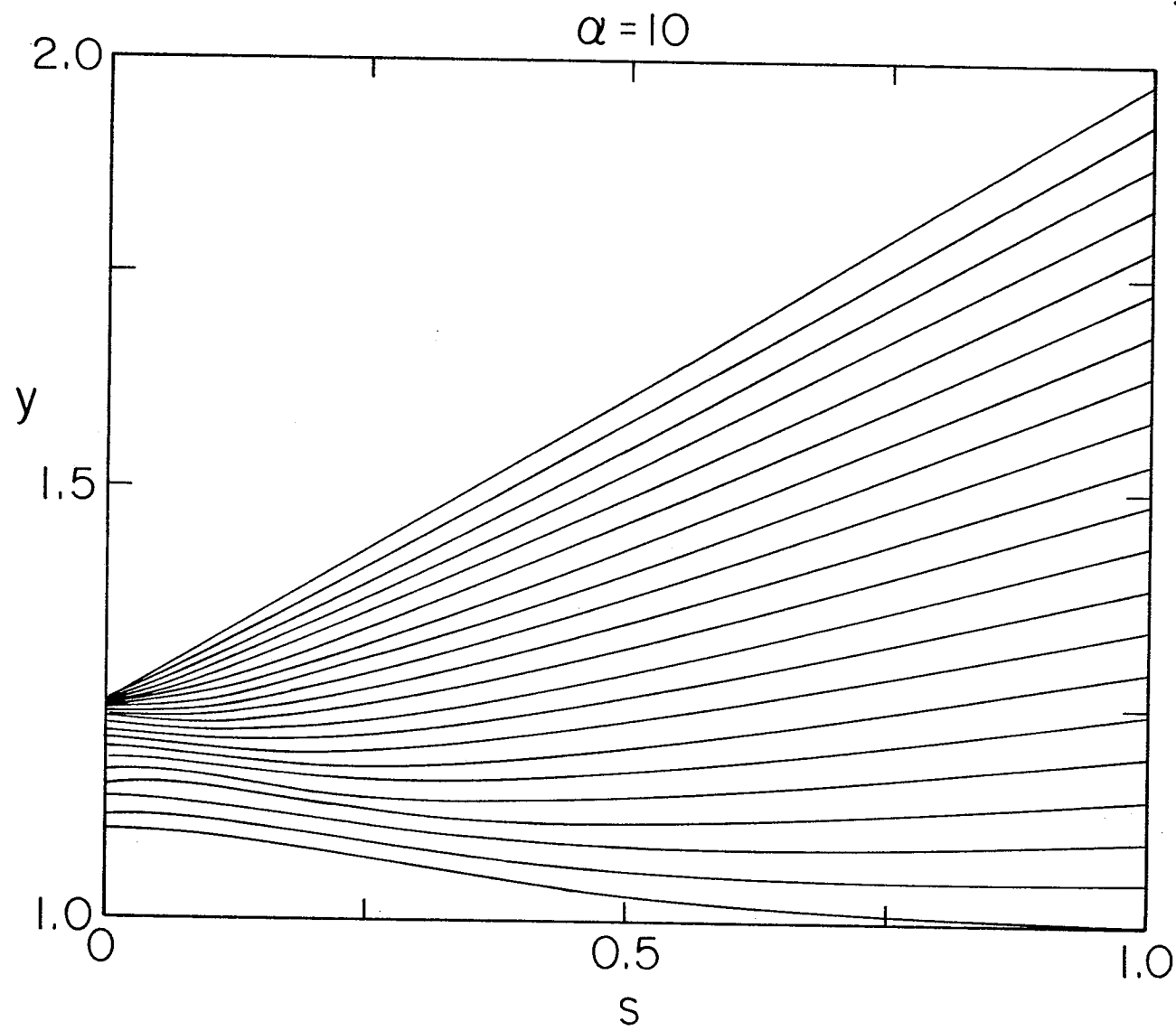

Fig. 2(b)

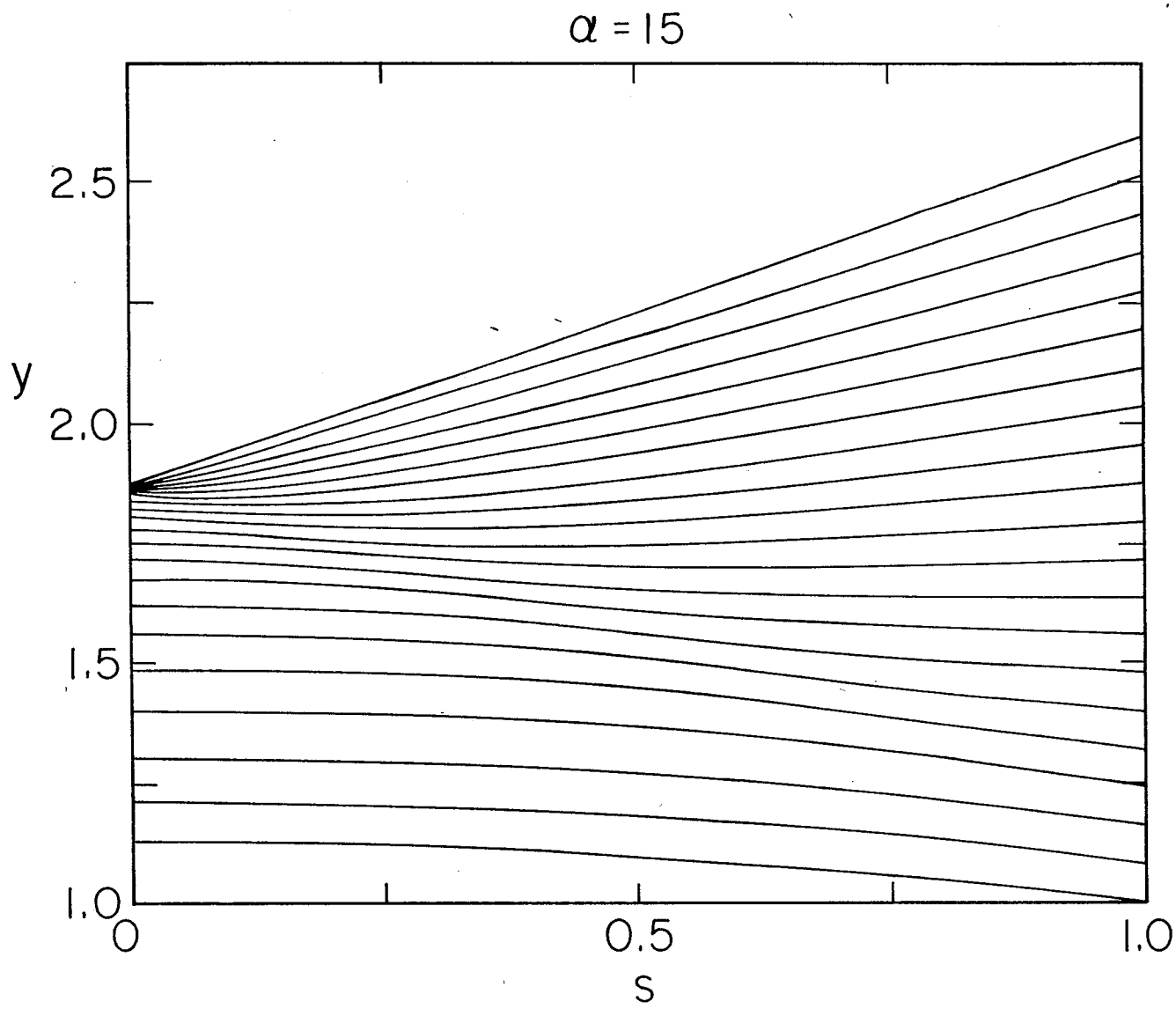

Fig. 2(c)

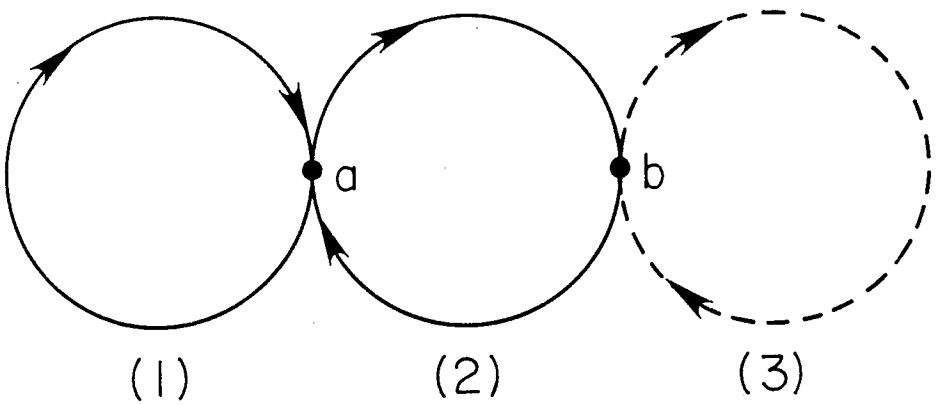

Fig. 3

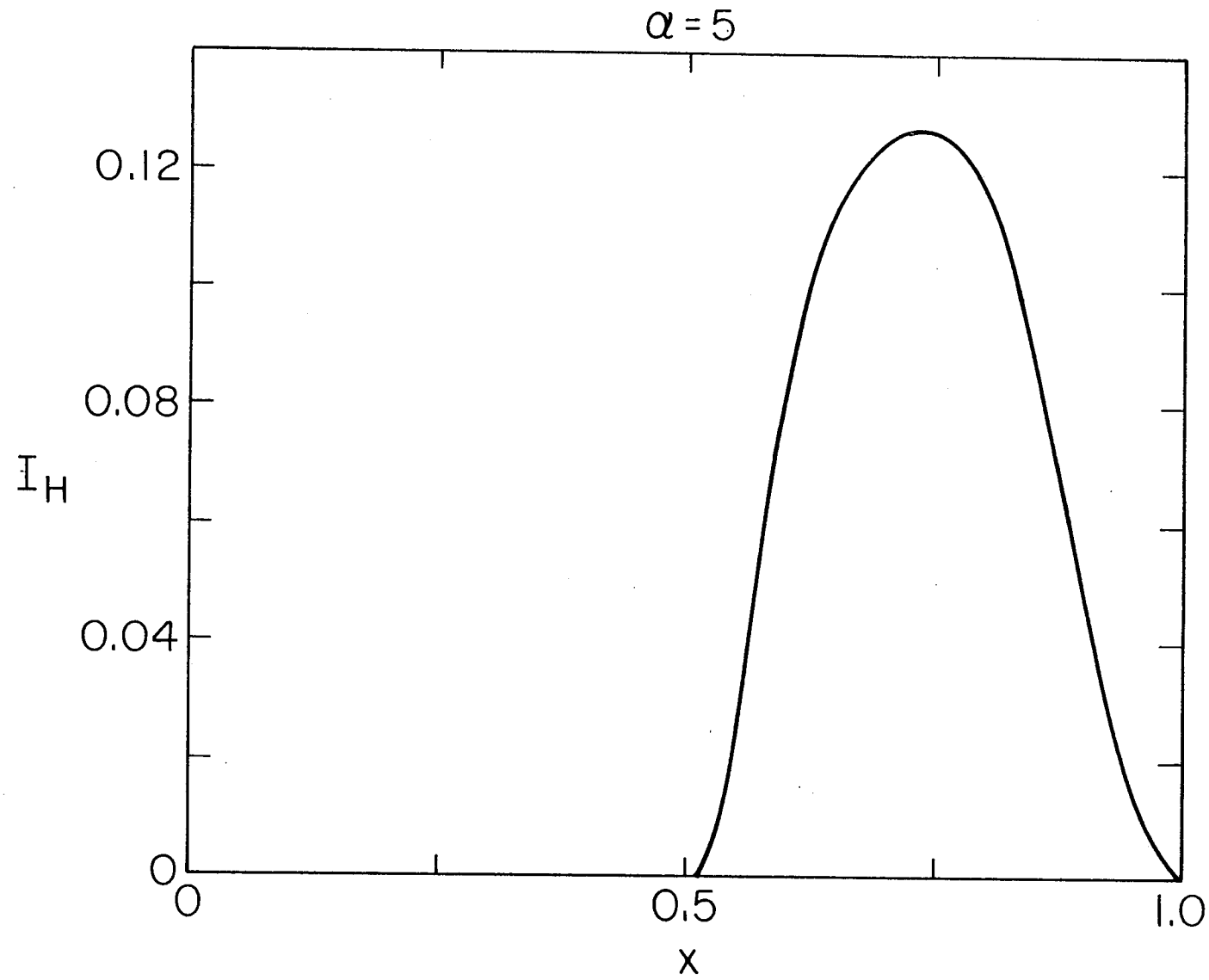

Fig. 4(a)

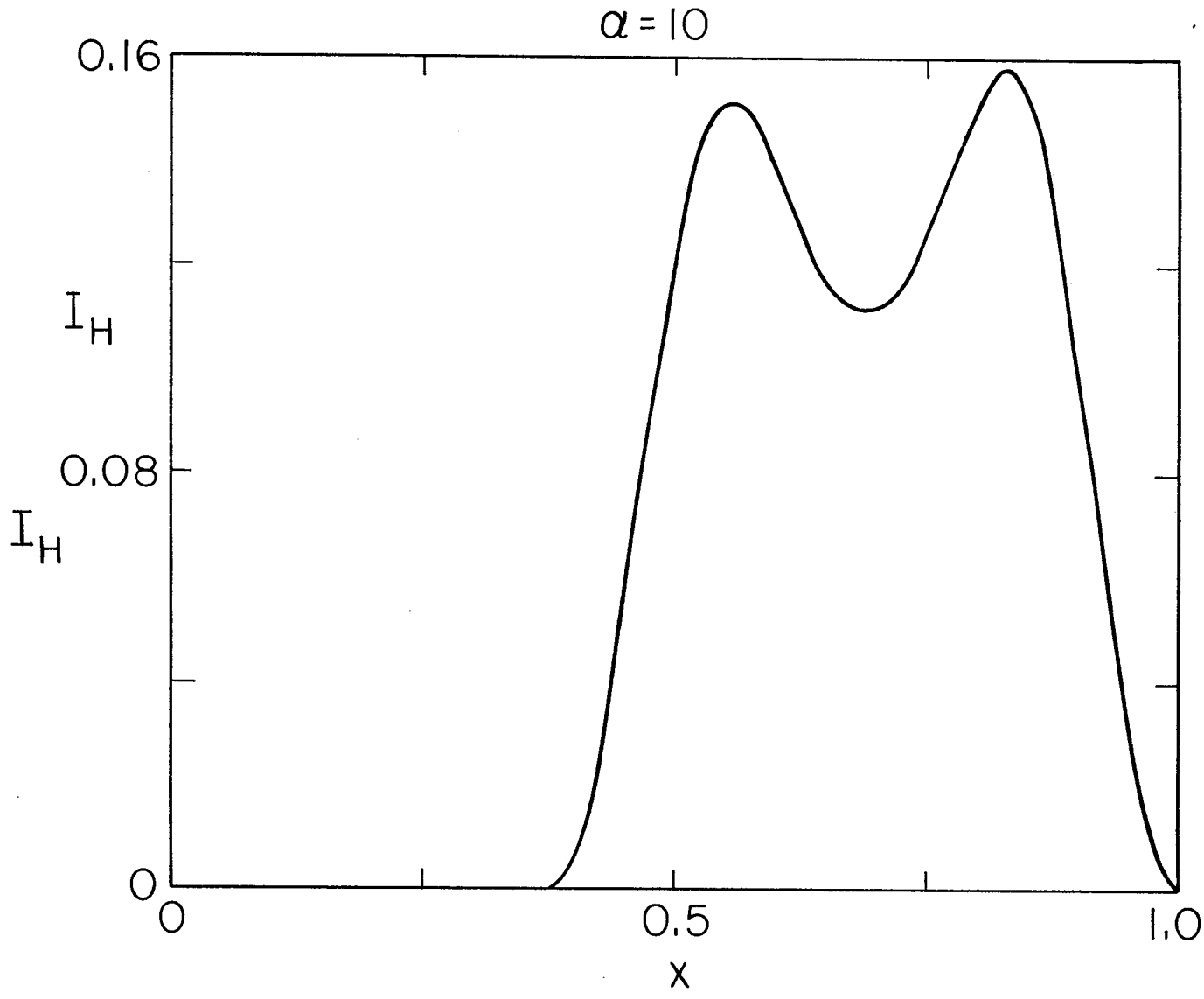

Fig. 4(b)

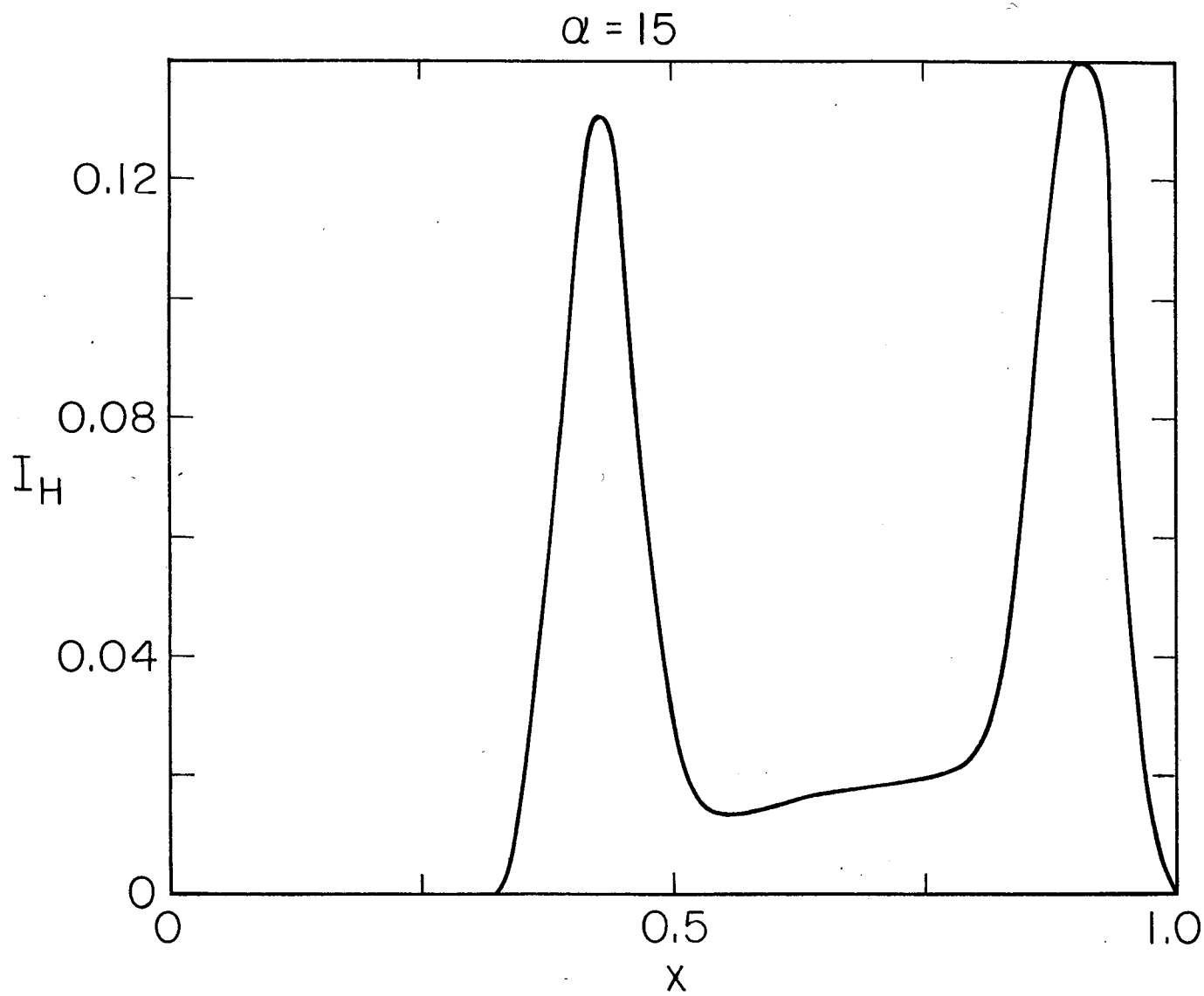

Fig. 4(c)

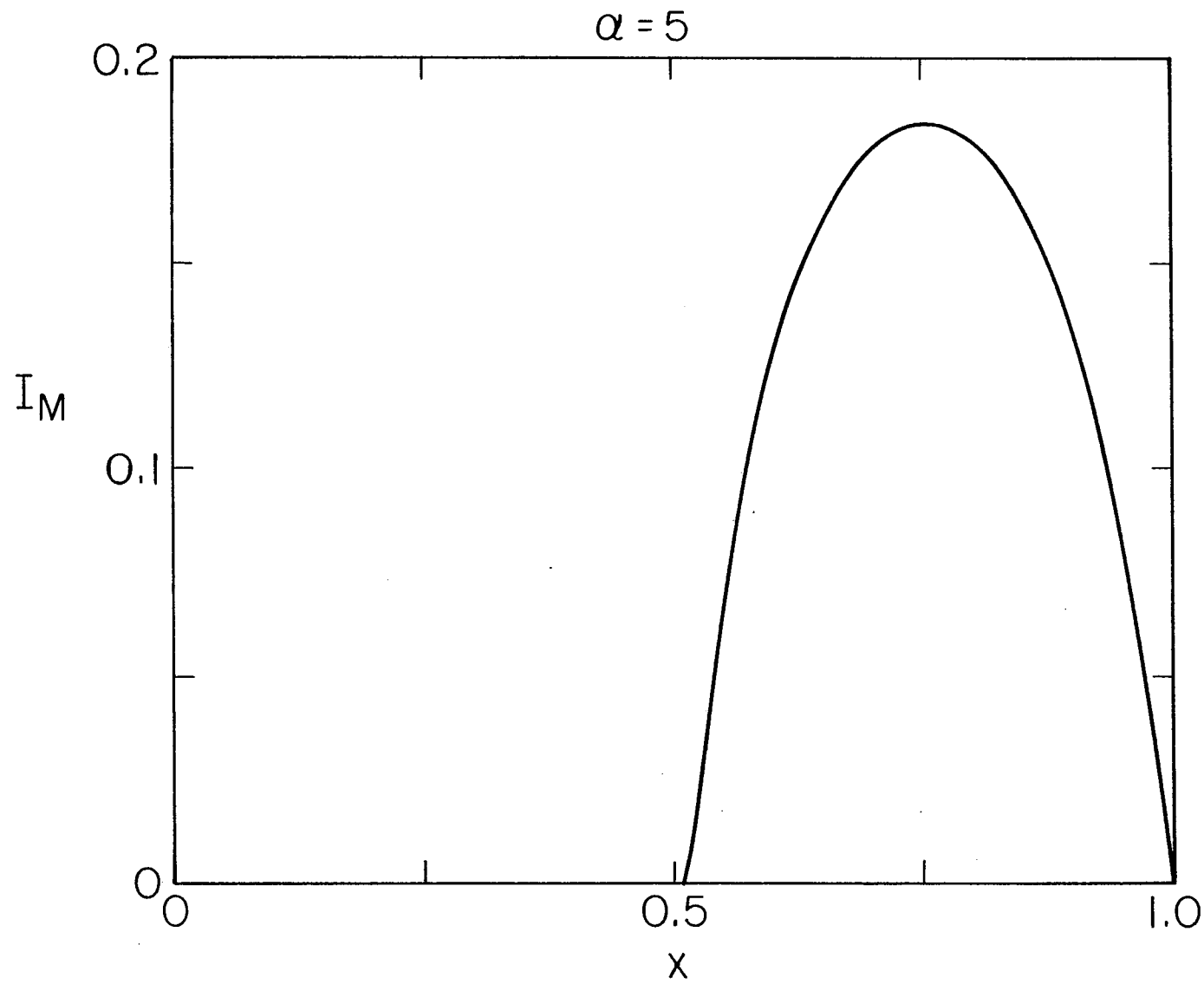

Fig. 5(a)

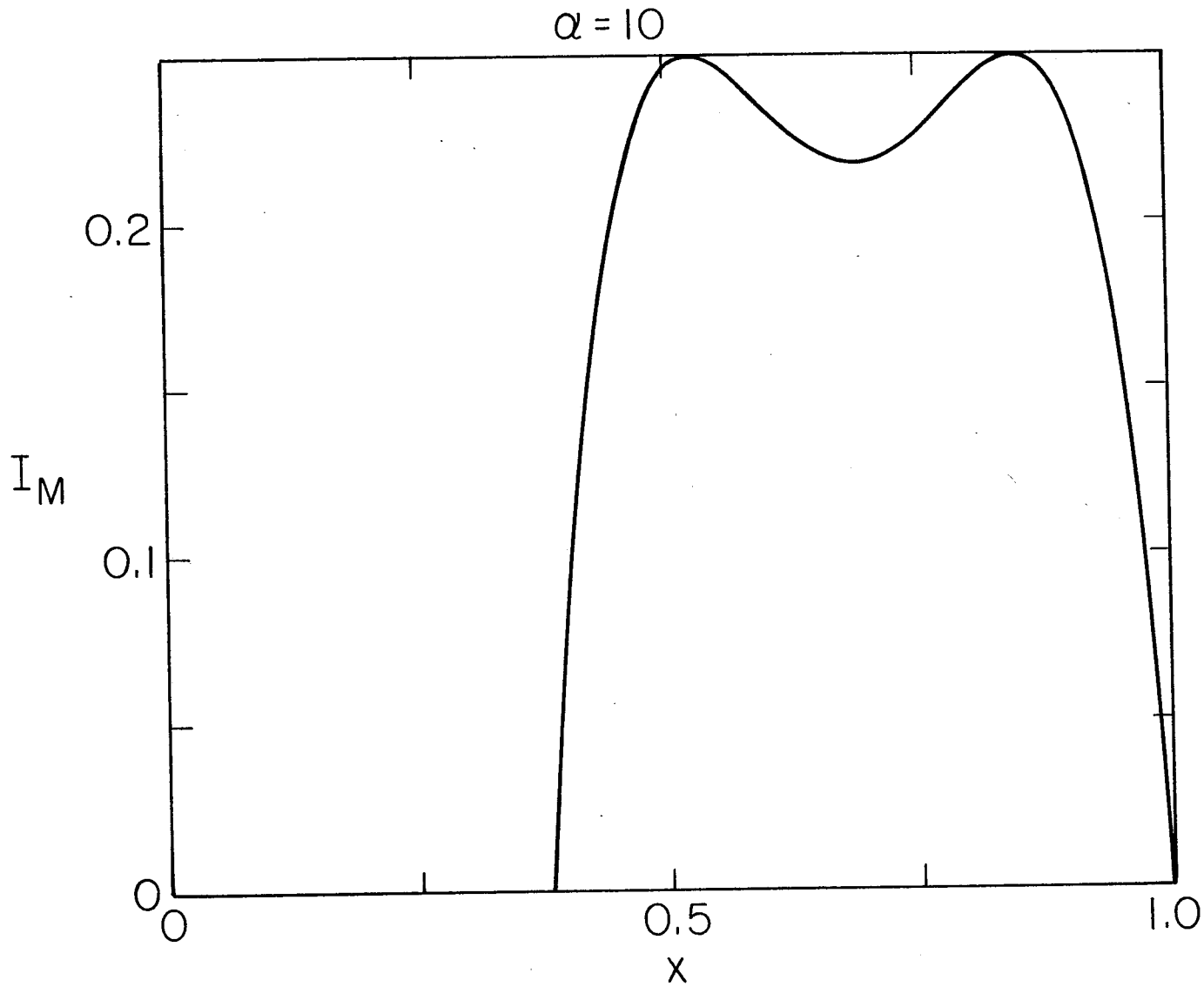

Fig. 5(b)

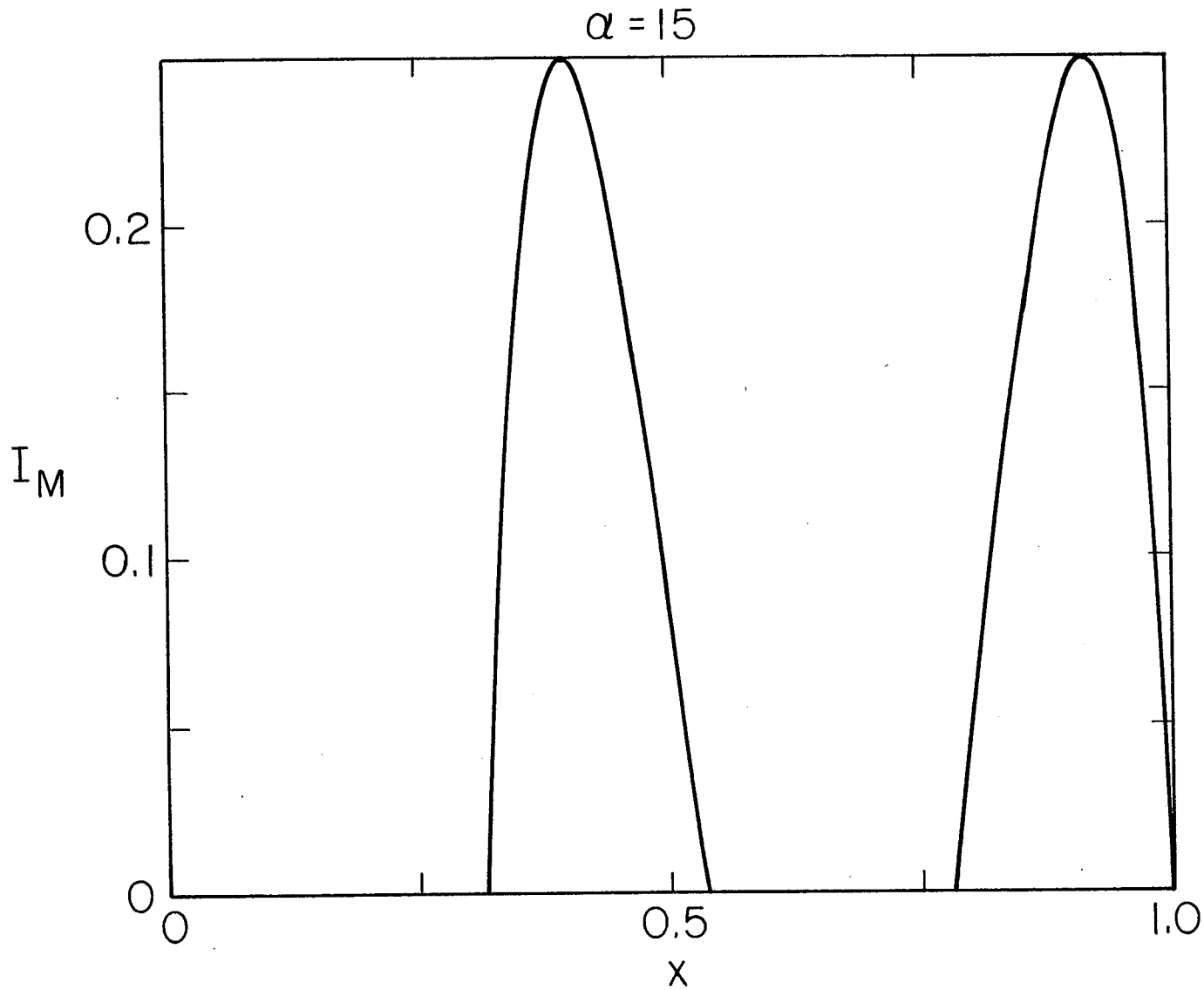

Fig. 5(c)

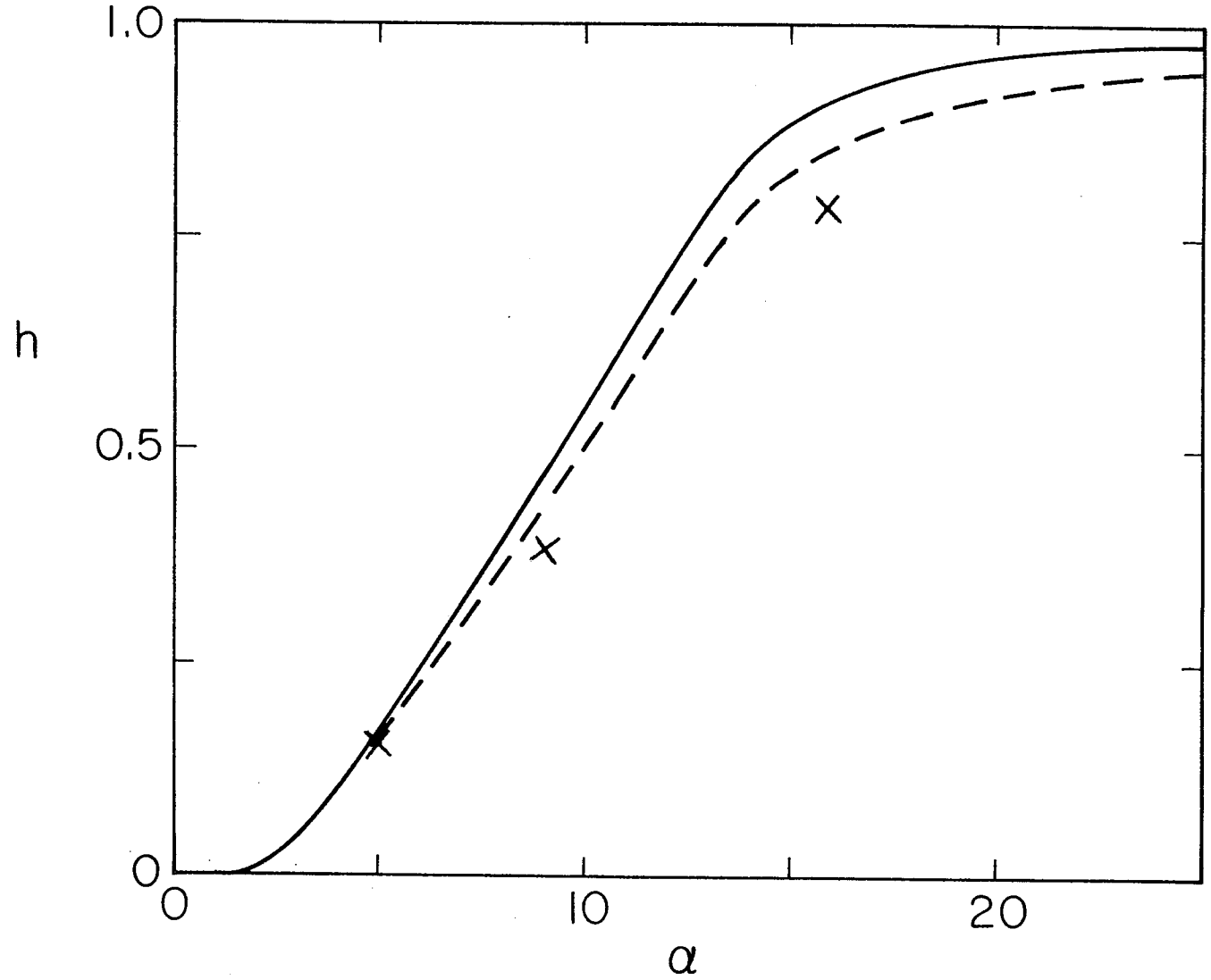

Fig. 6

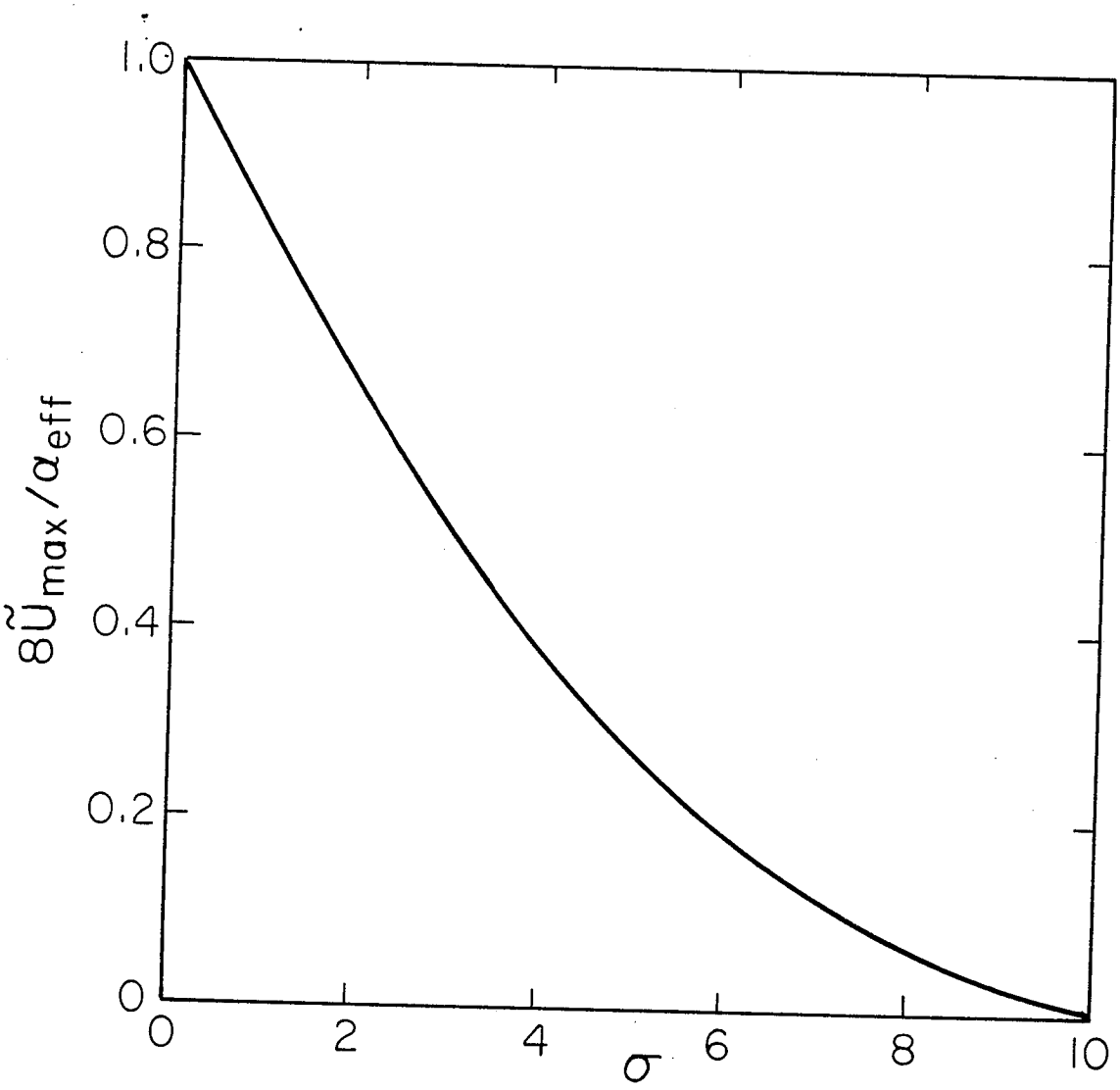

Fig. 7

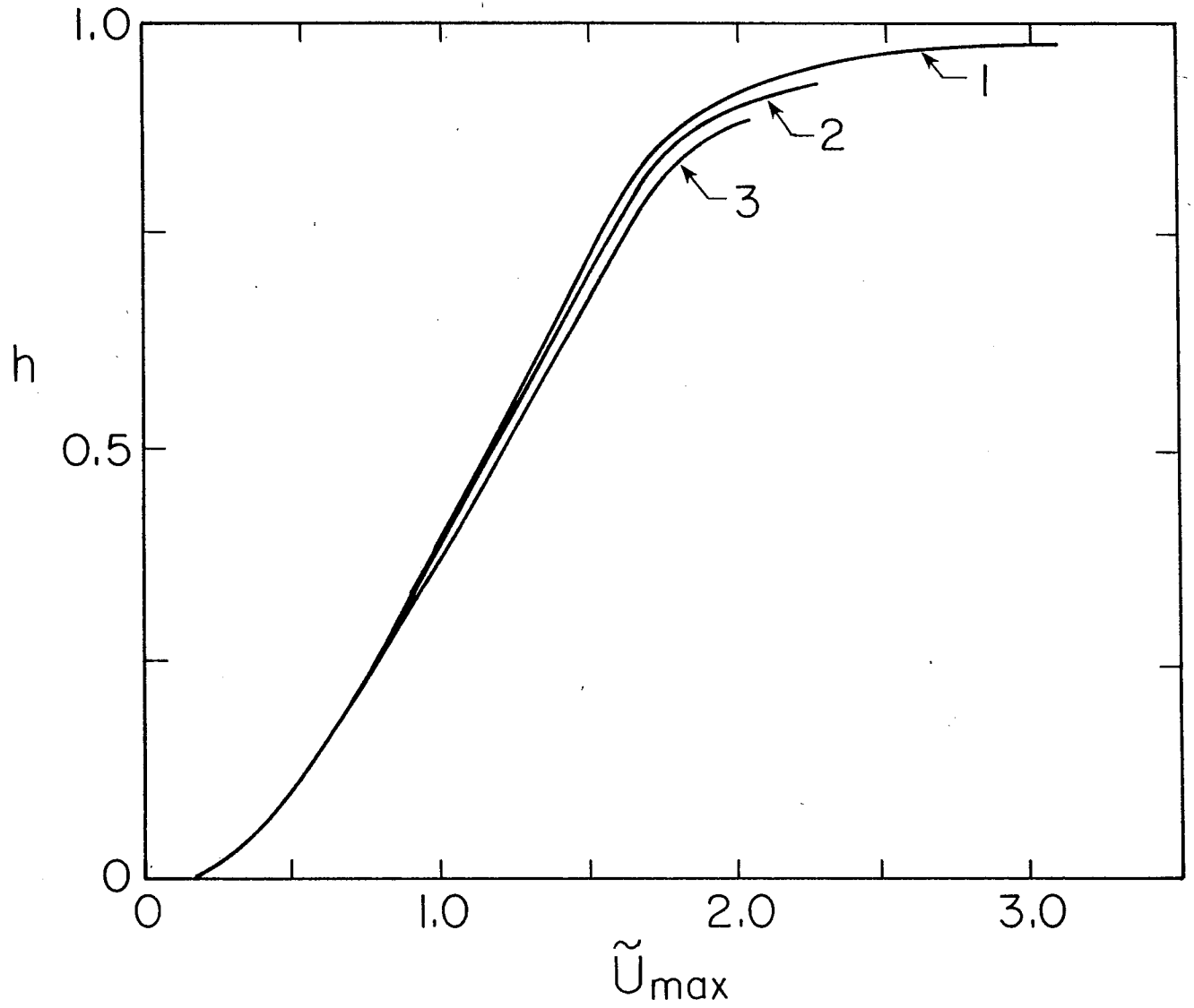

Fig. 8

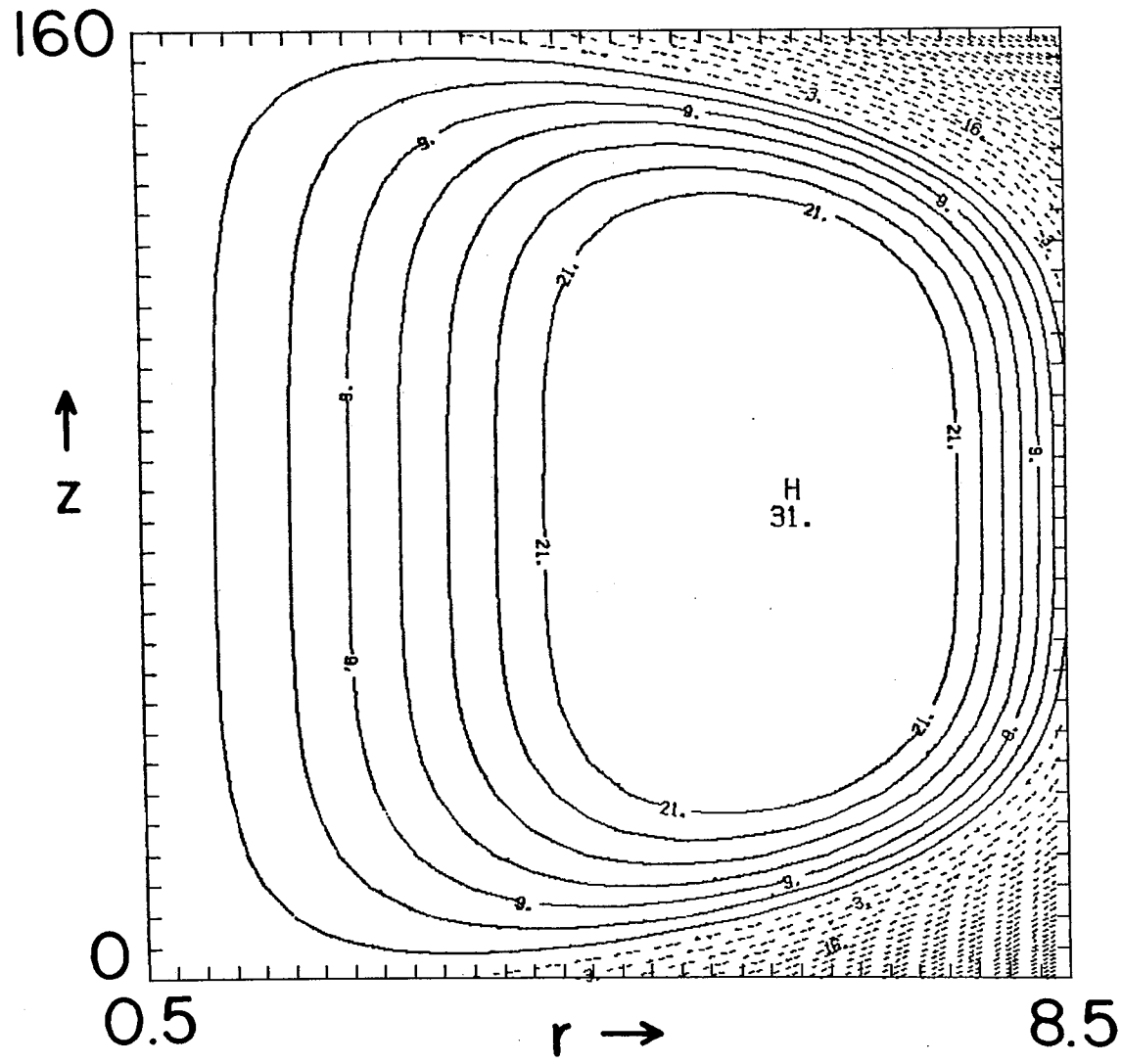

Fig. 9

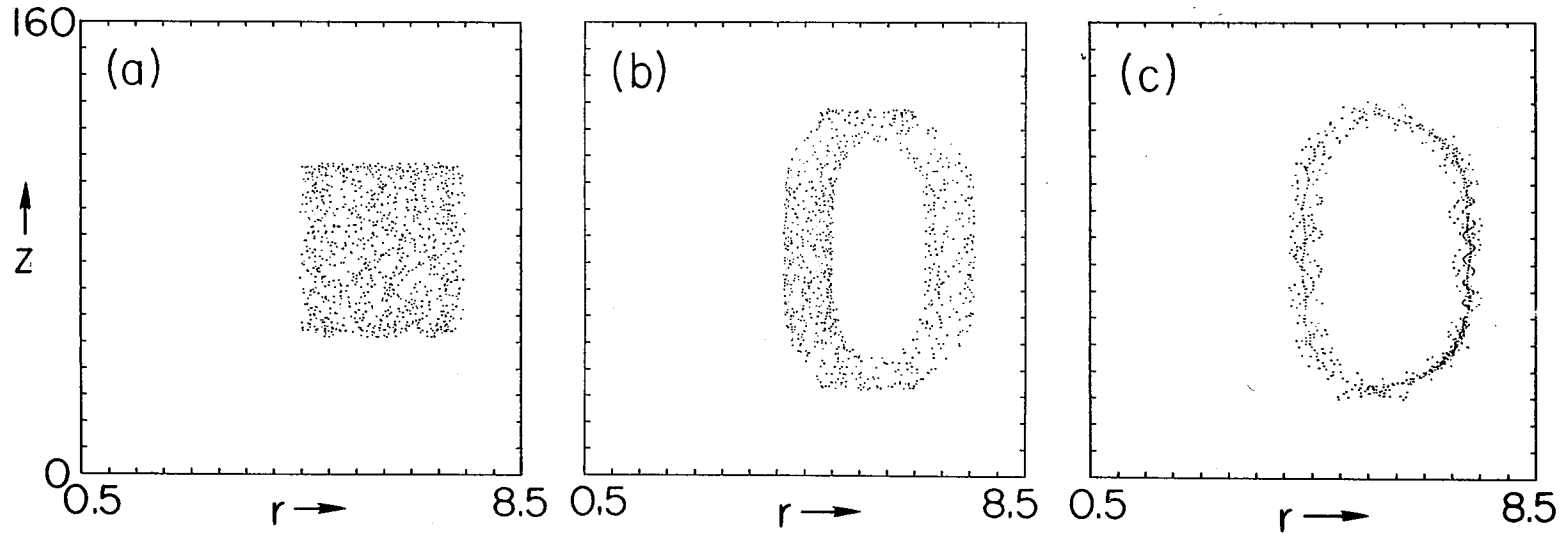

Fig. 10

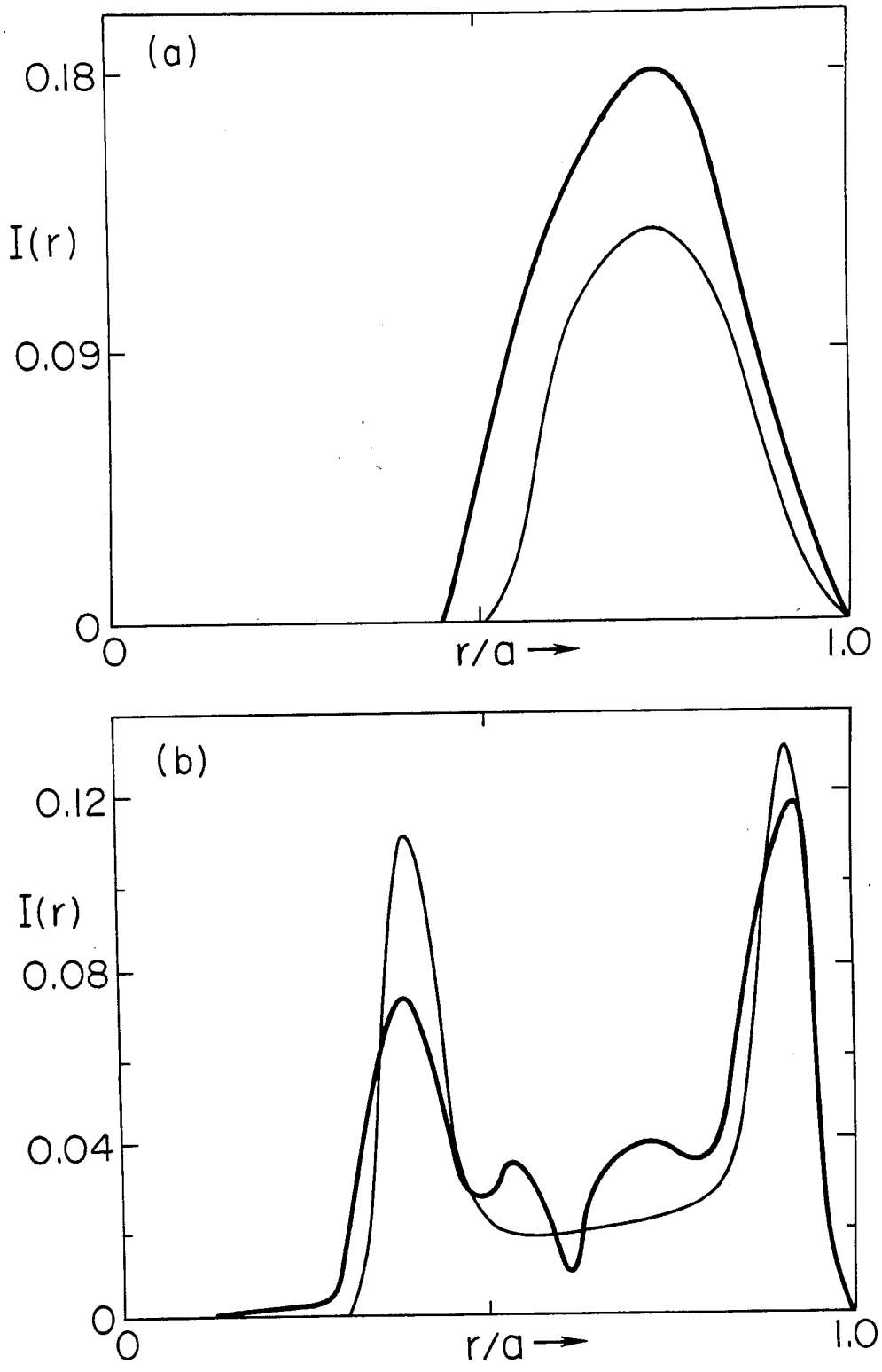

Fig. 11

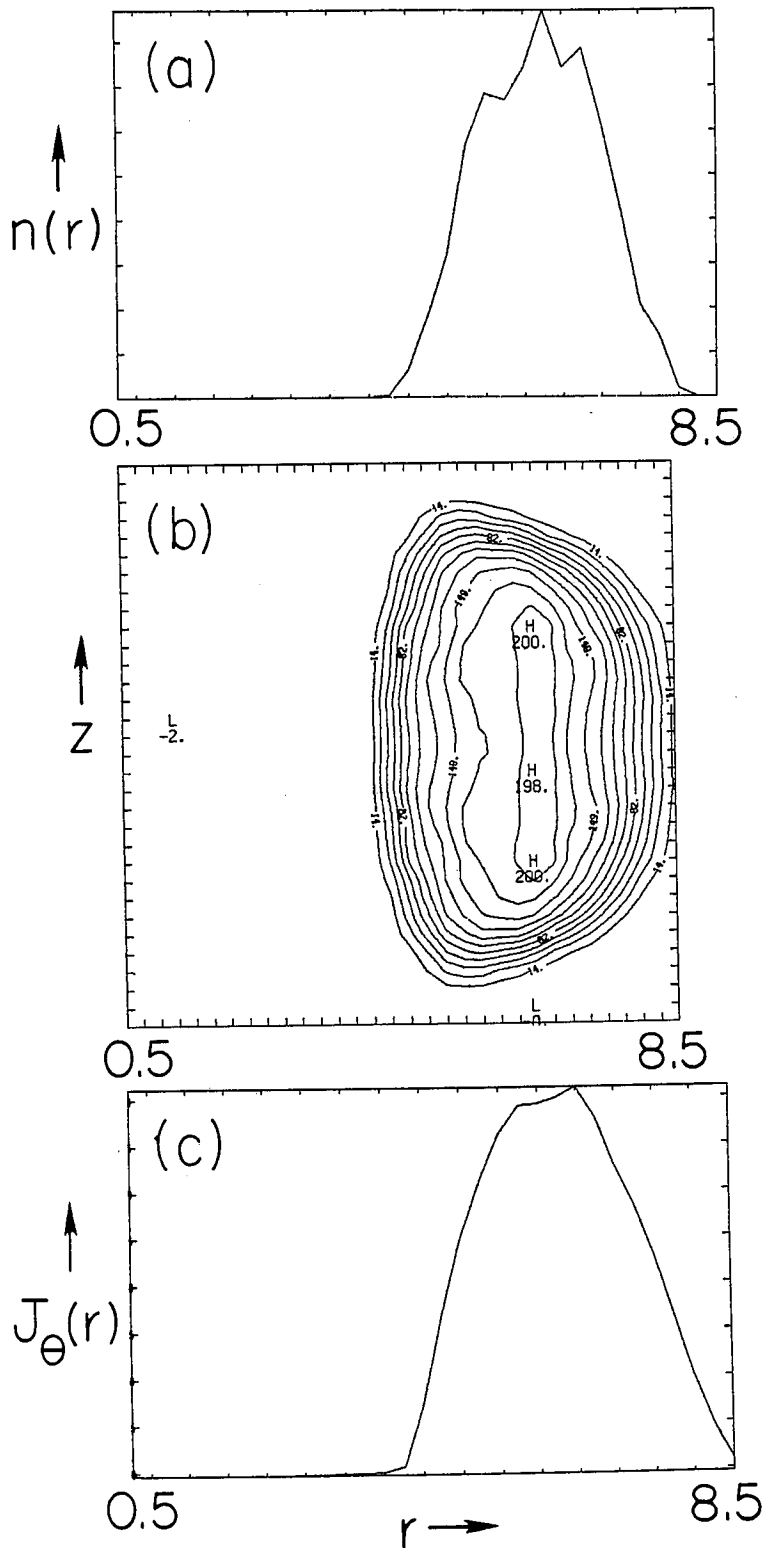

Fig. 12

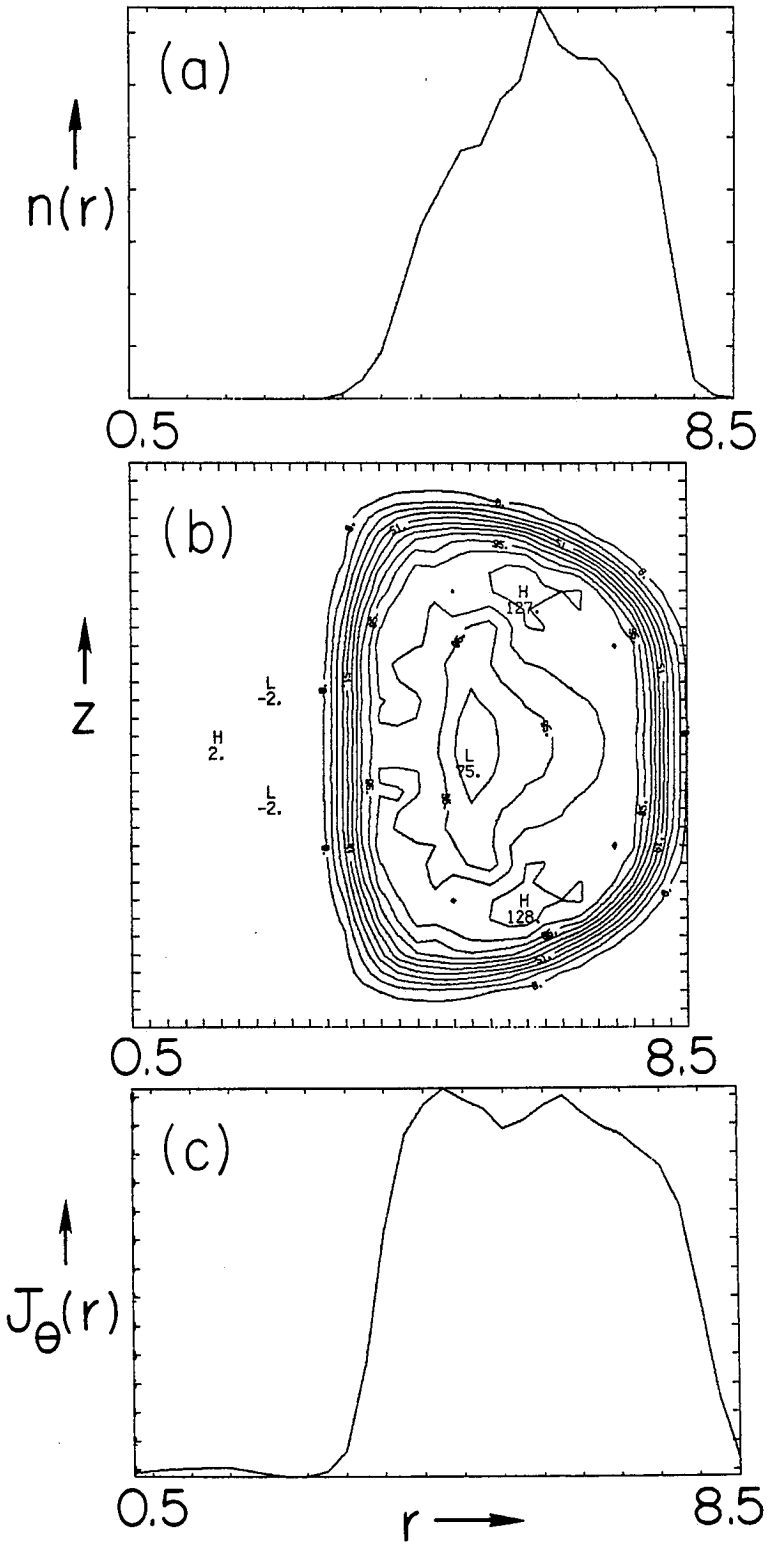

Fig. 13

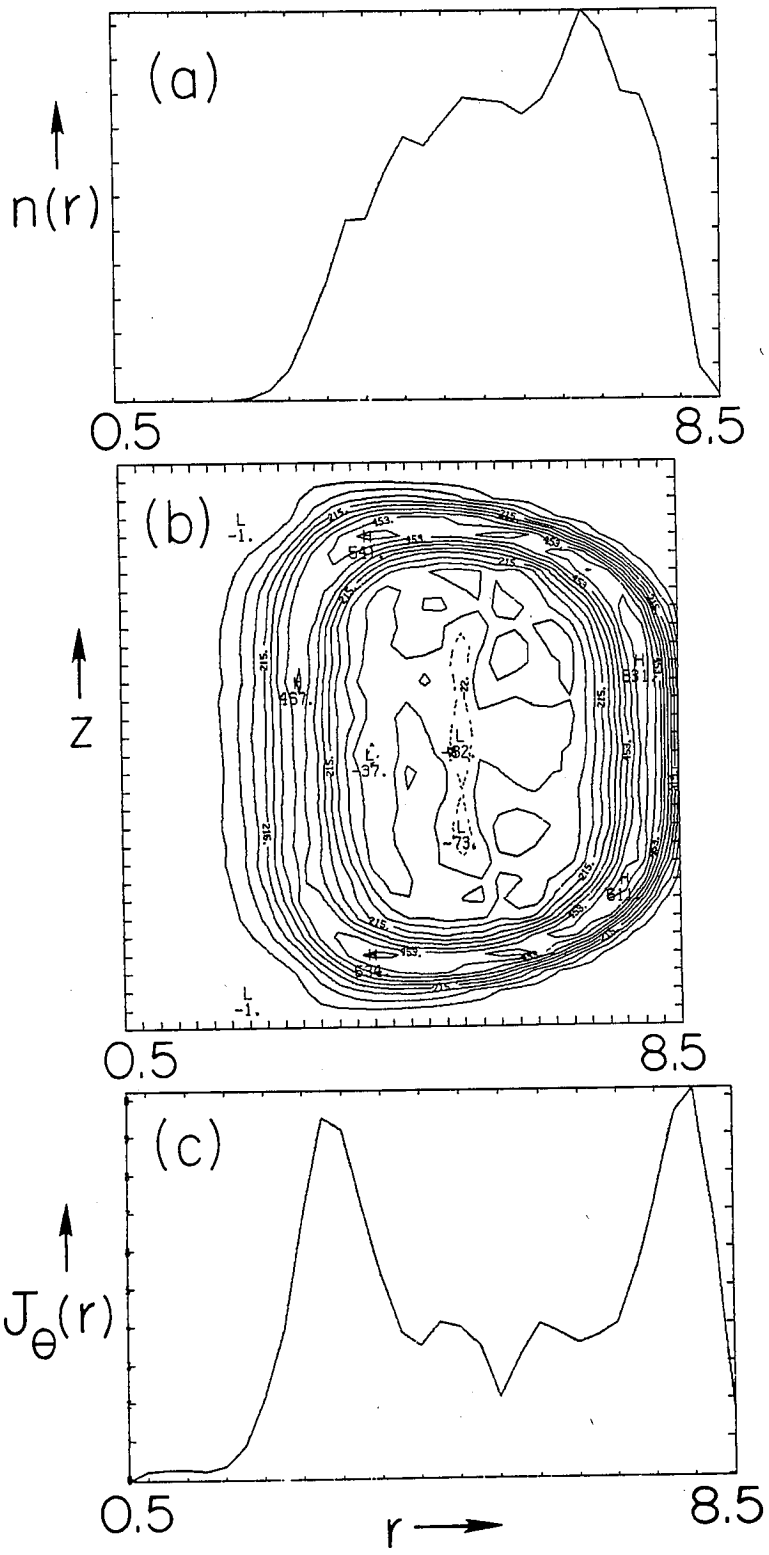

Fig. 14

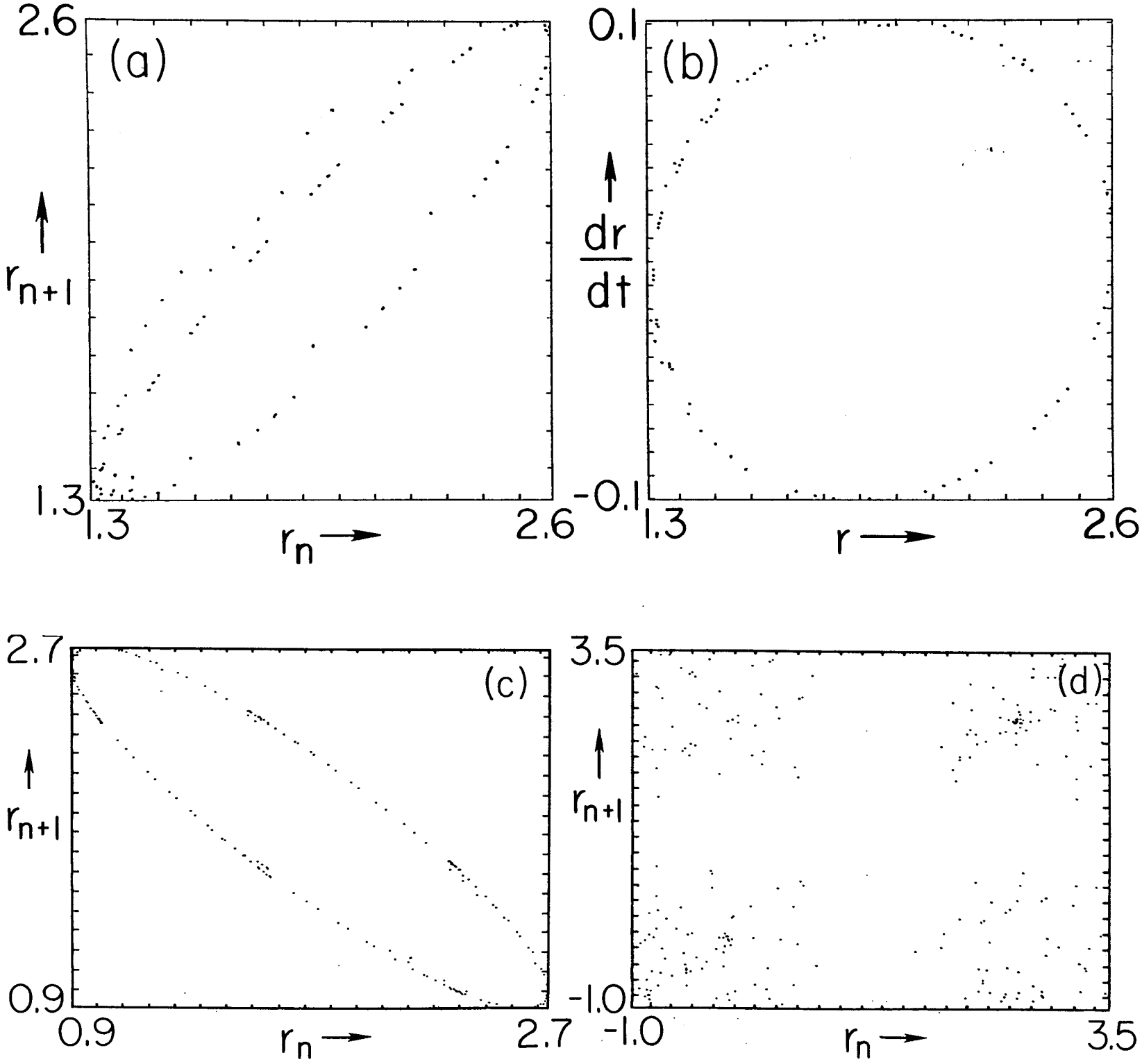
2.6
(a)
r_{n+1}
1.3
1.3
r_n
2.6
0.1
(b)
$\frac{dr}{dt}$
-0.1
1.3
r
2.6
2.7
(c)
r_{n+1}
0.9
0.9
r_n
2.7
3.5
(d)
r_{n+1}
-1.0
-1.0
r_n
3.5

Fig. 15

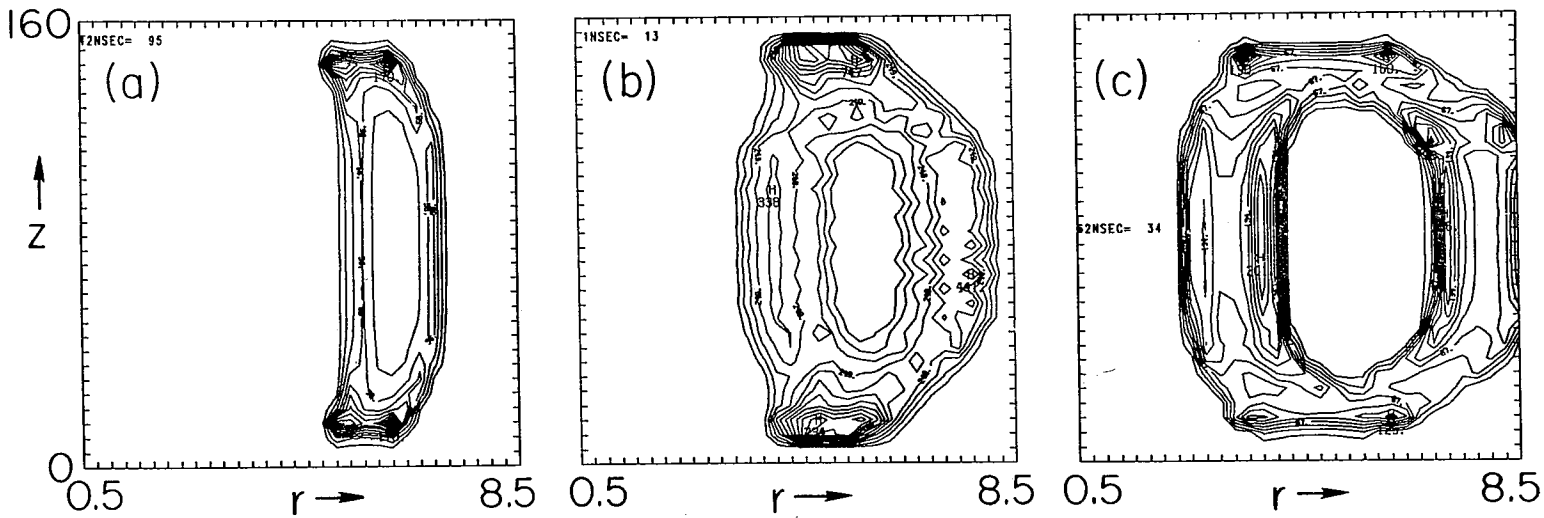

Fig. 16

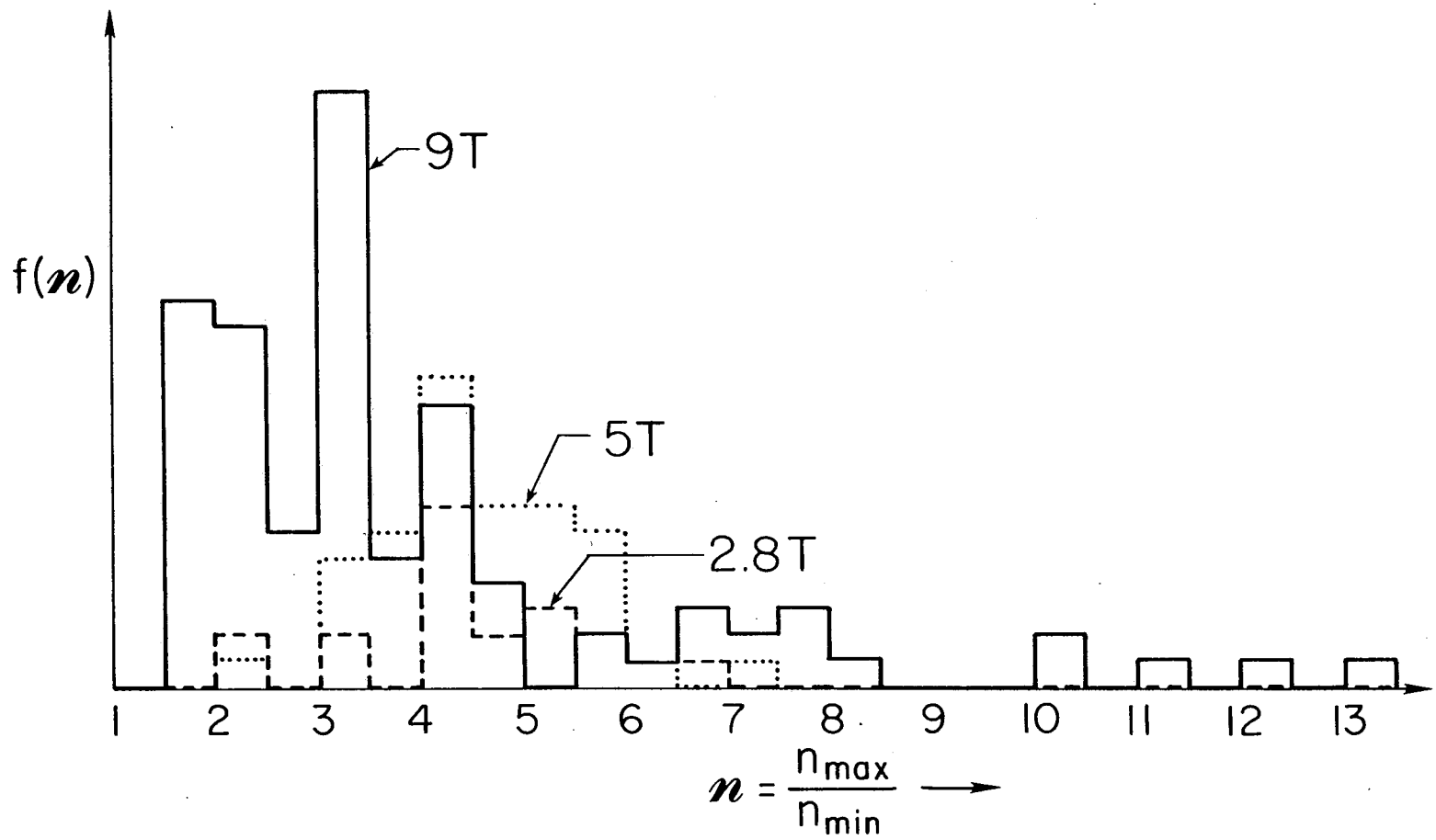

Fig. 17

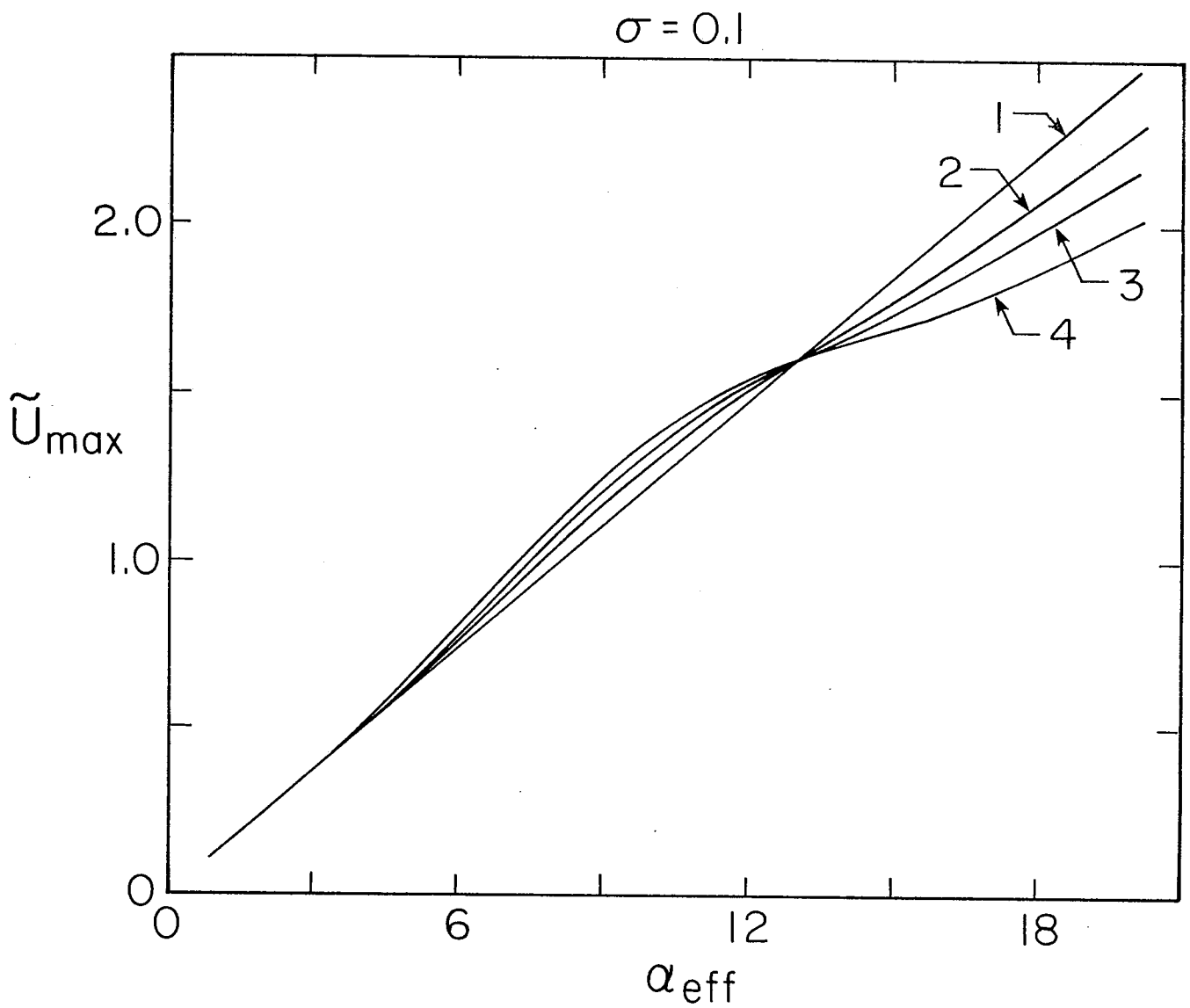

Fig. 18(a)

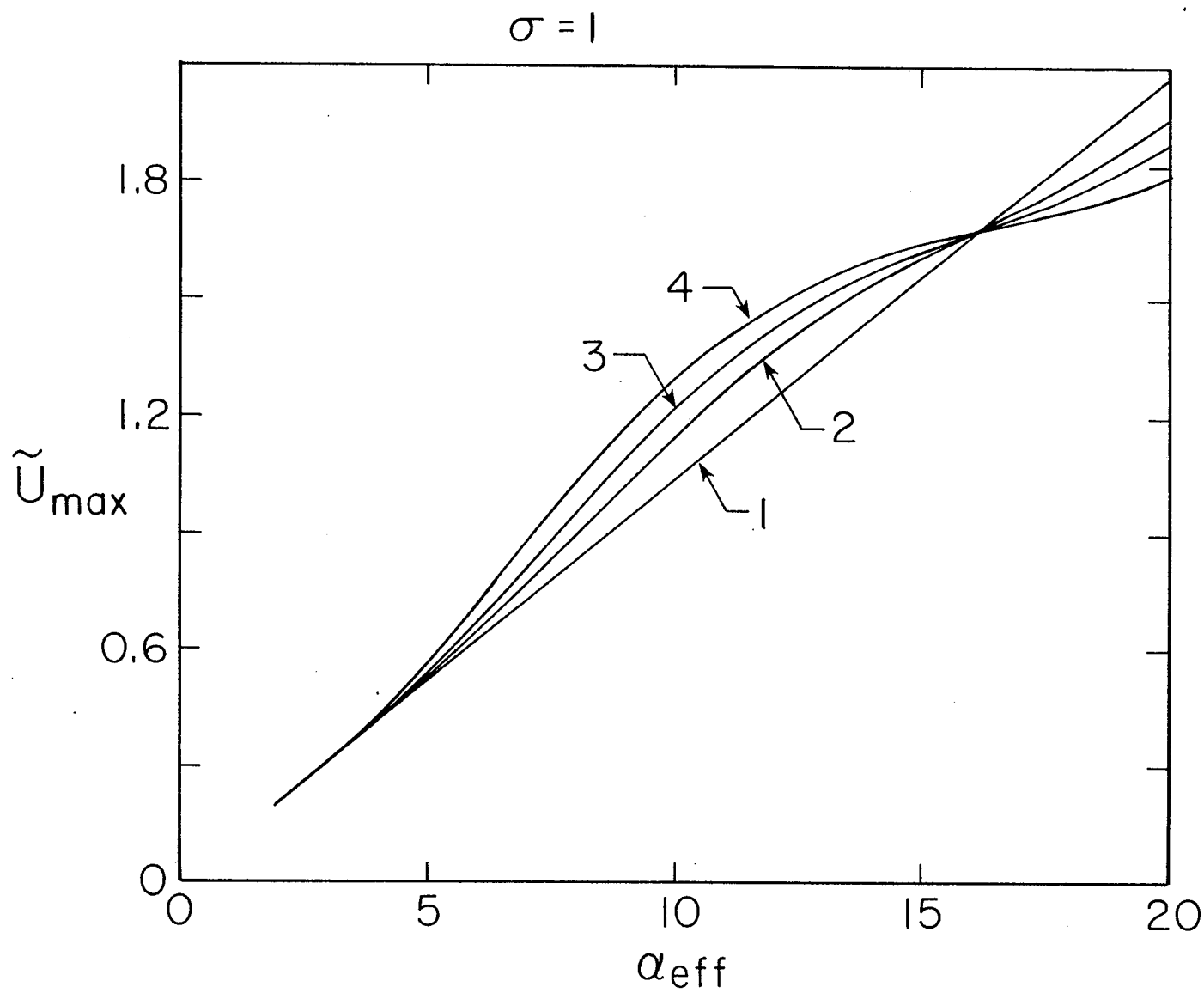

Fig. 18(b)

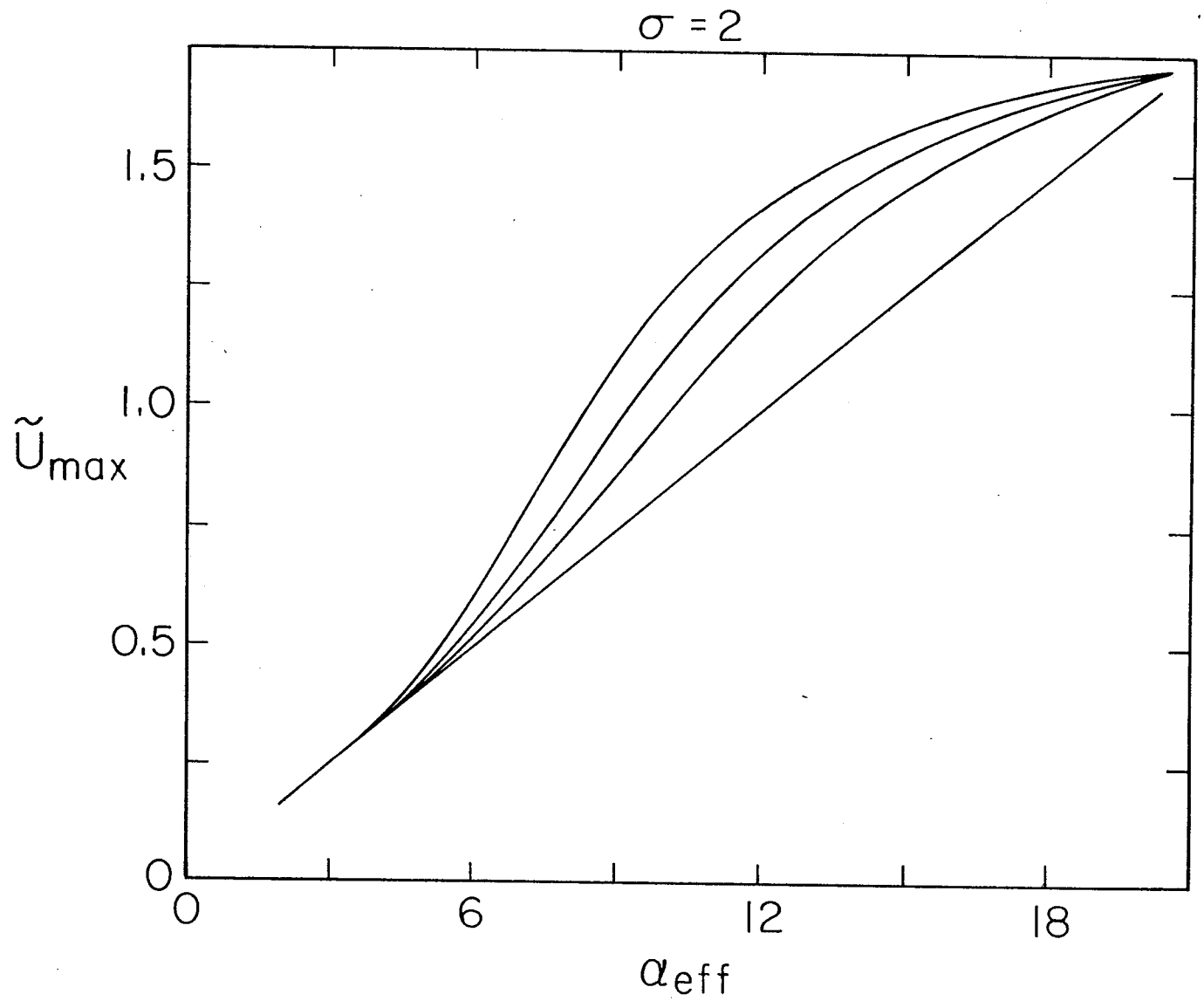

Fig. 18(c)

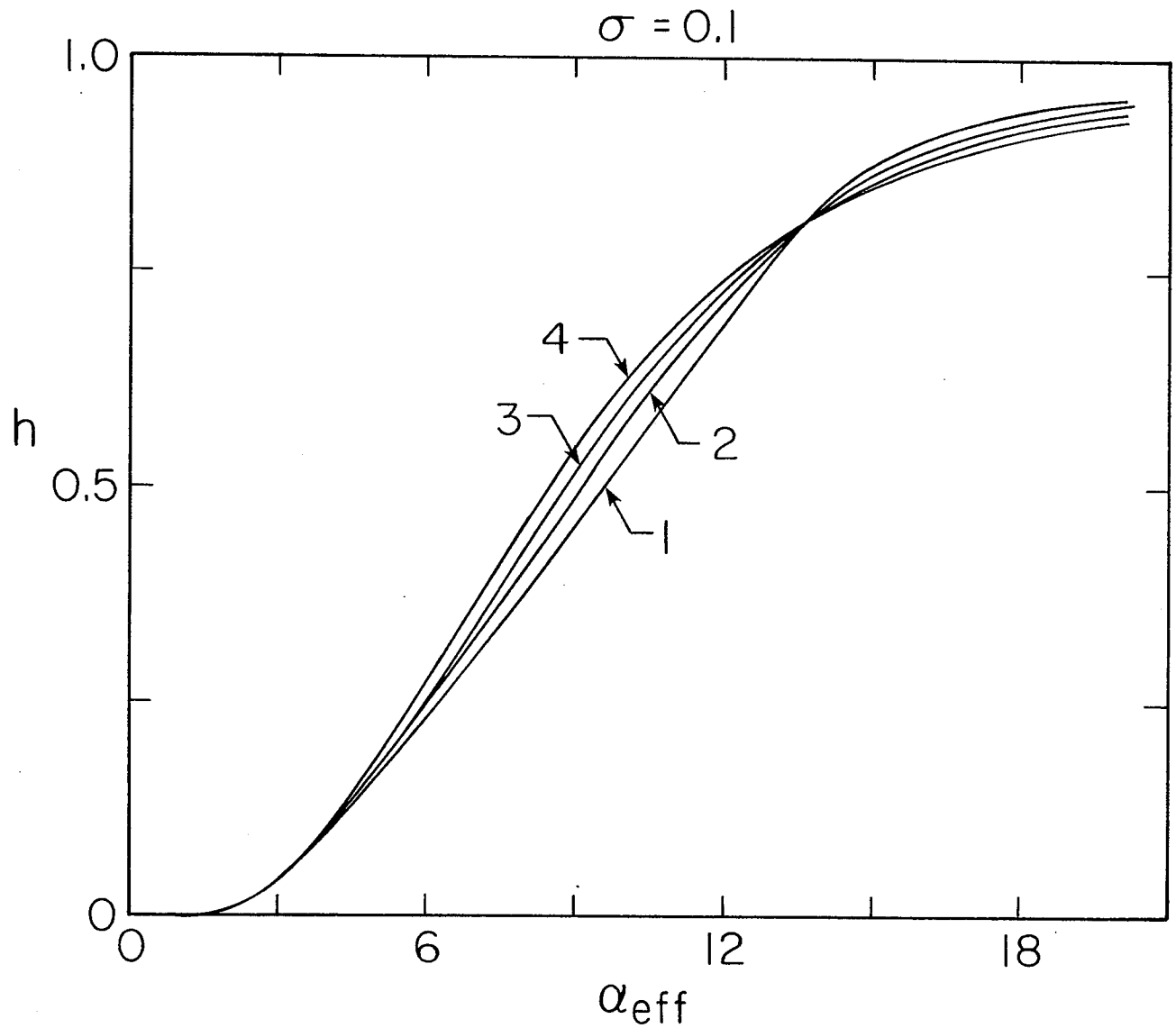

Fig. 19(a)

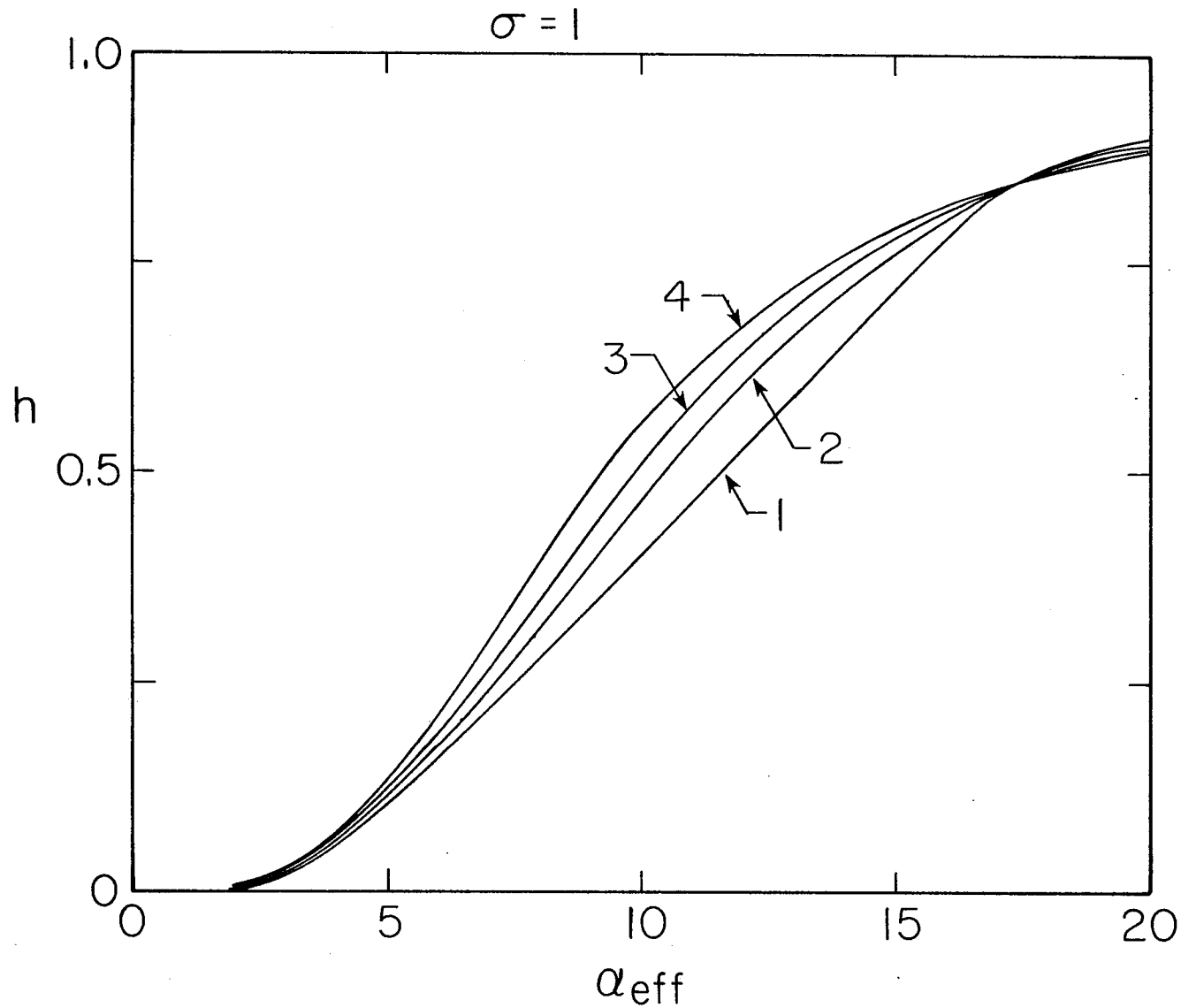

Fig. 19(b)

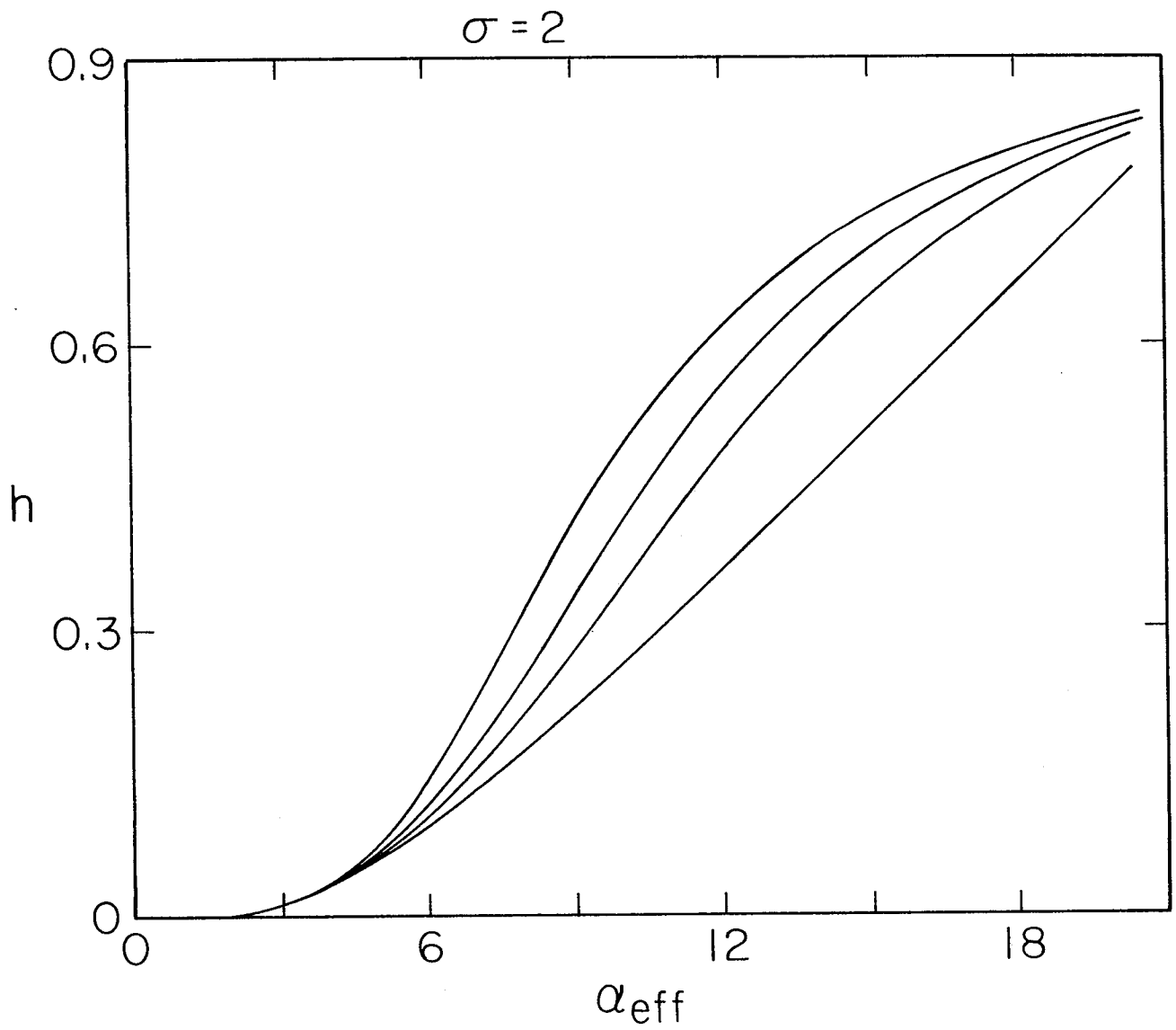

Fig. 19(c)

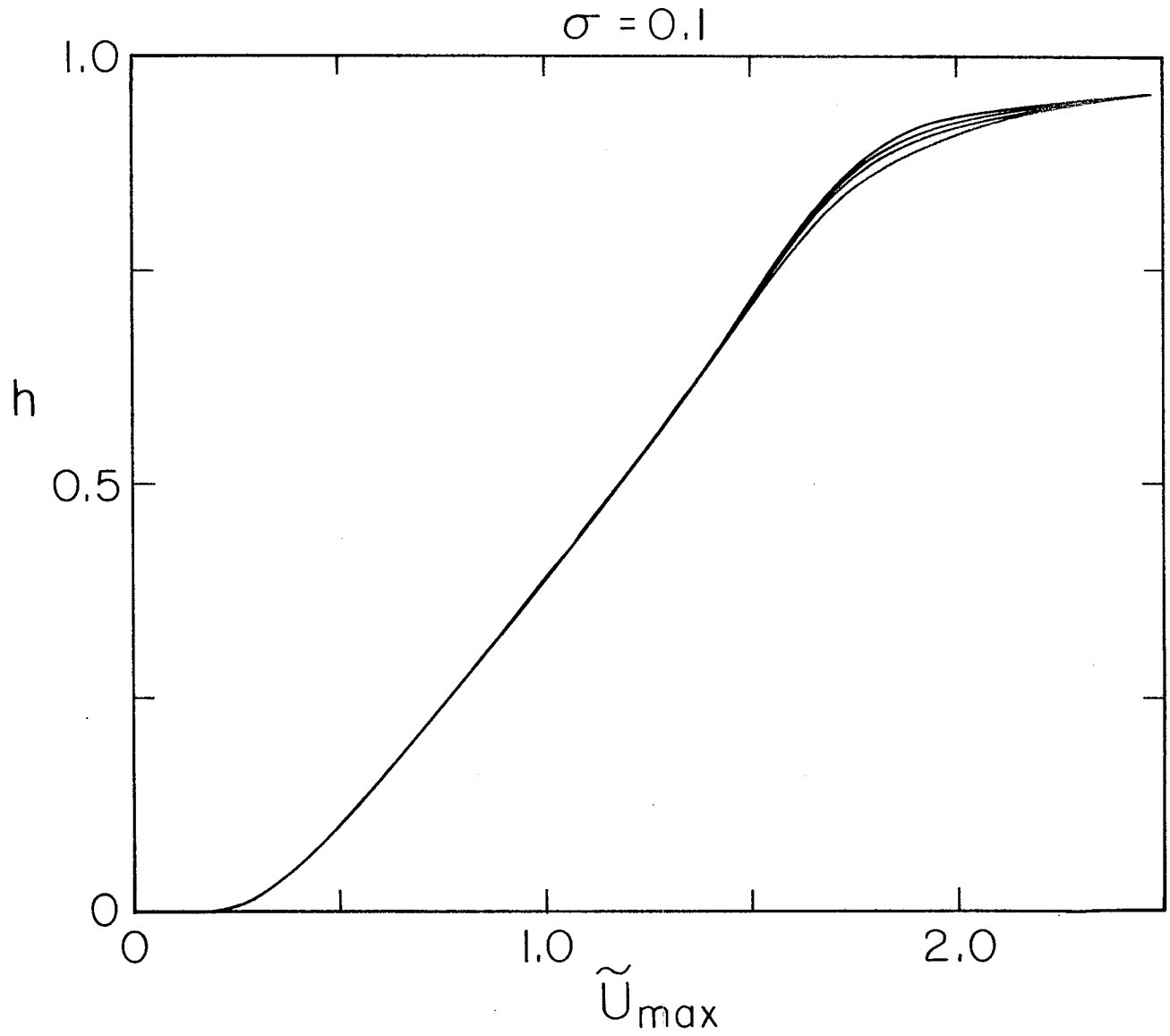

Fig. 20(a)

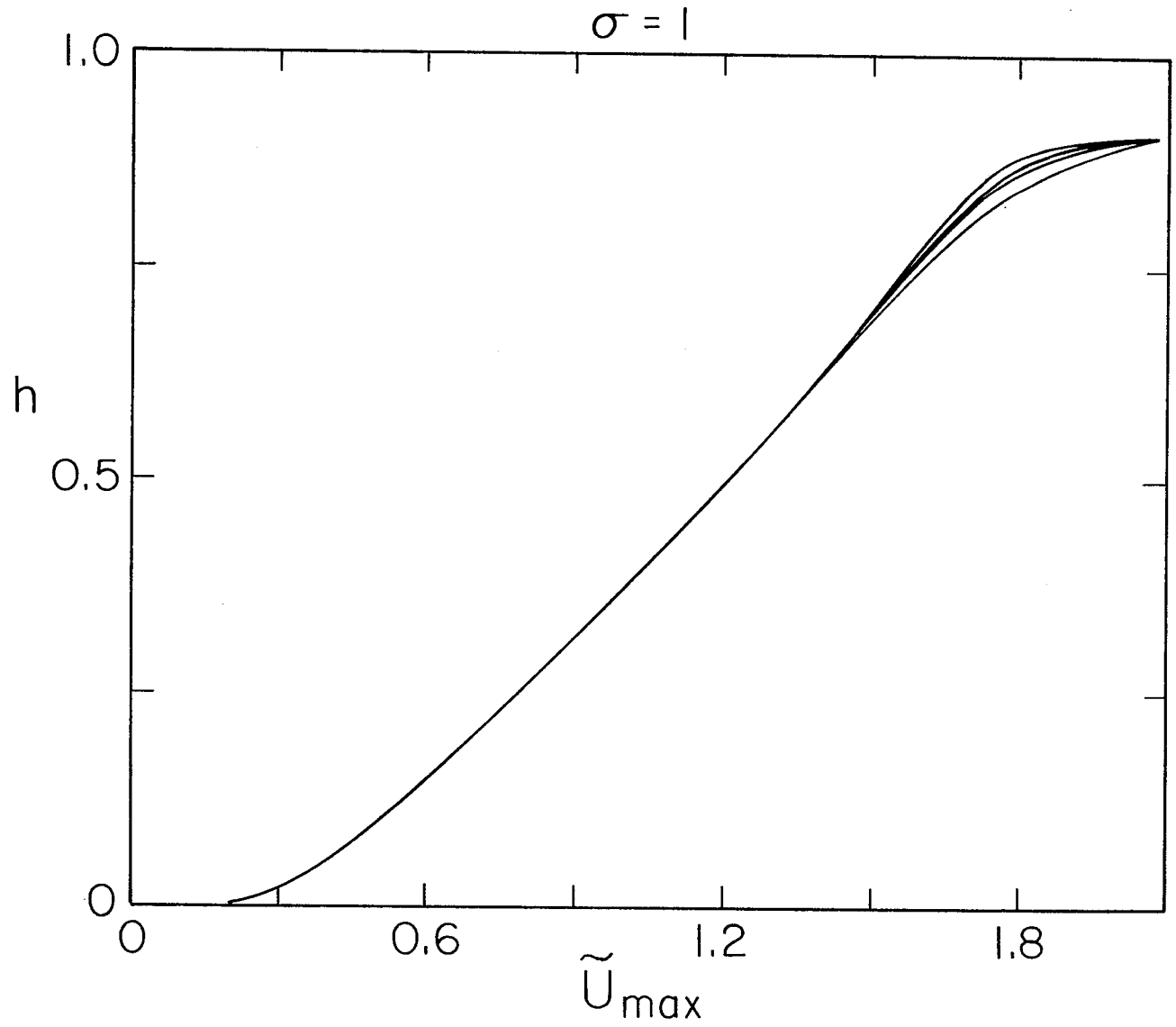

Fig. 20(b)

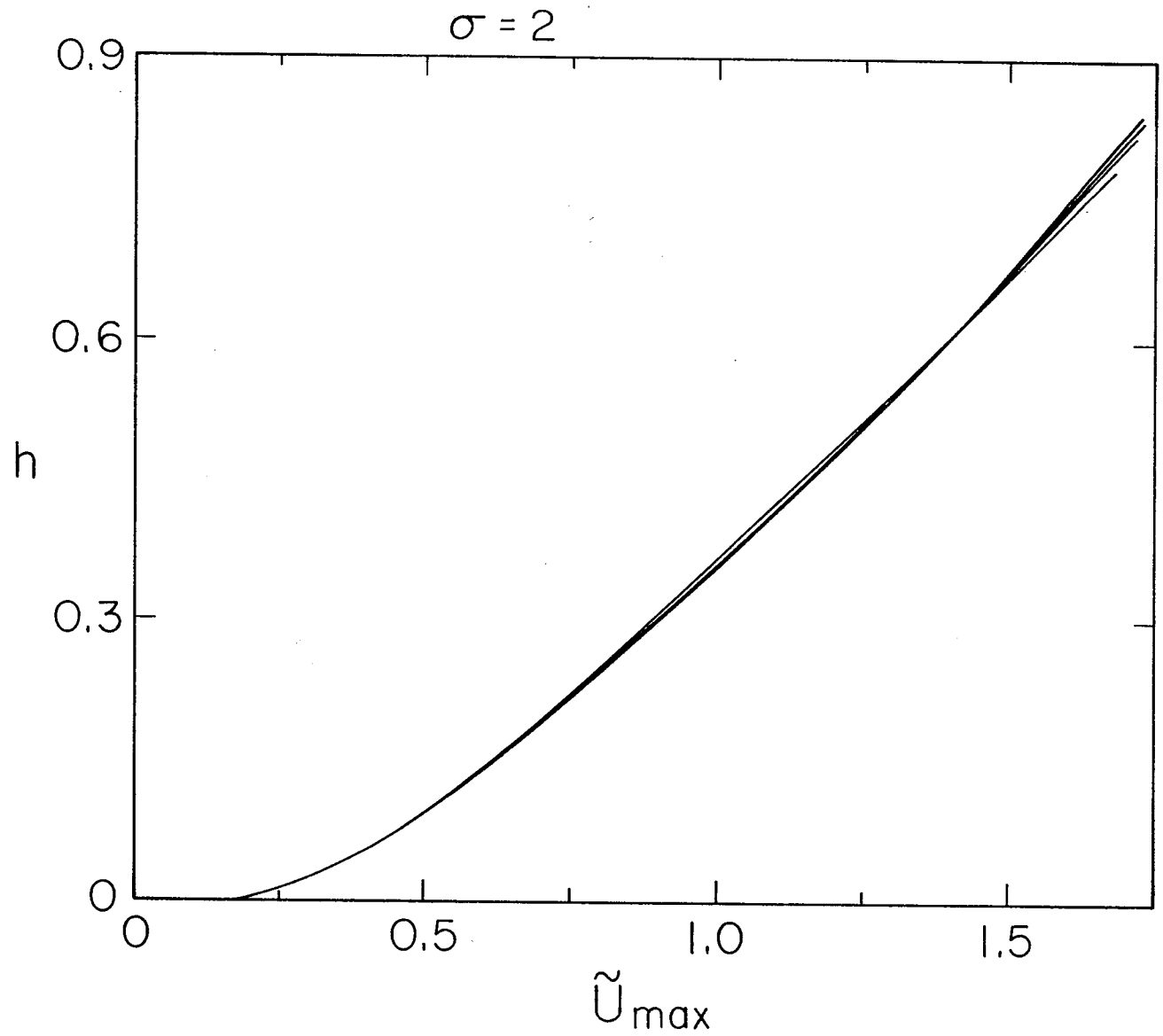

Fig. 20(c)

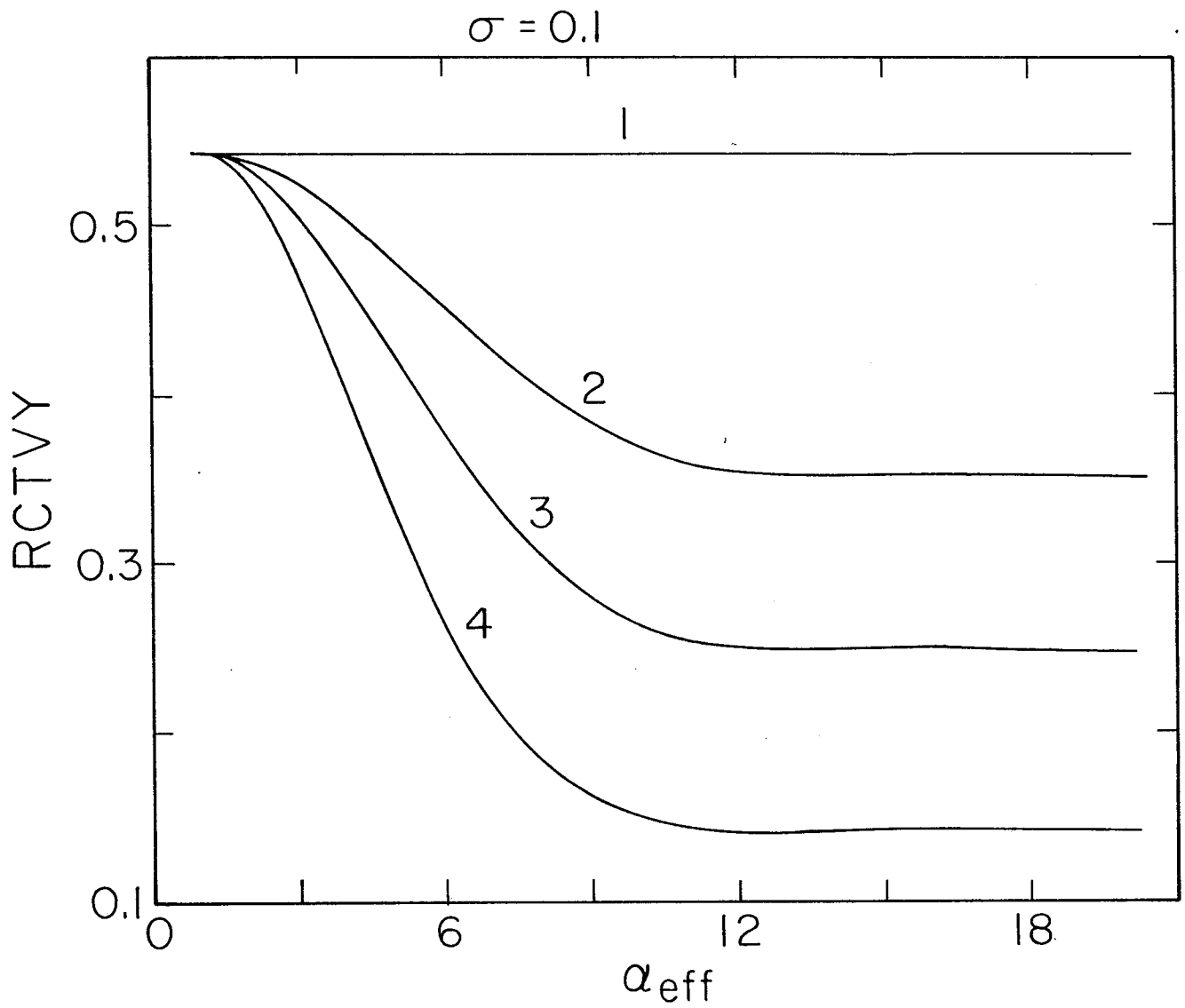

Fig. 21(a)

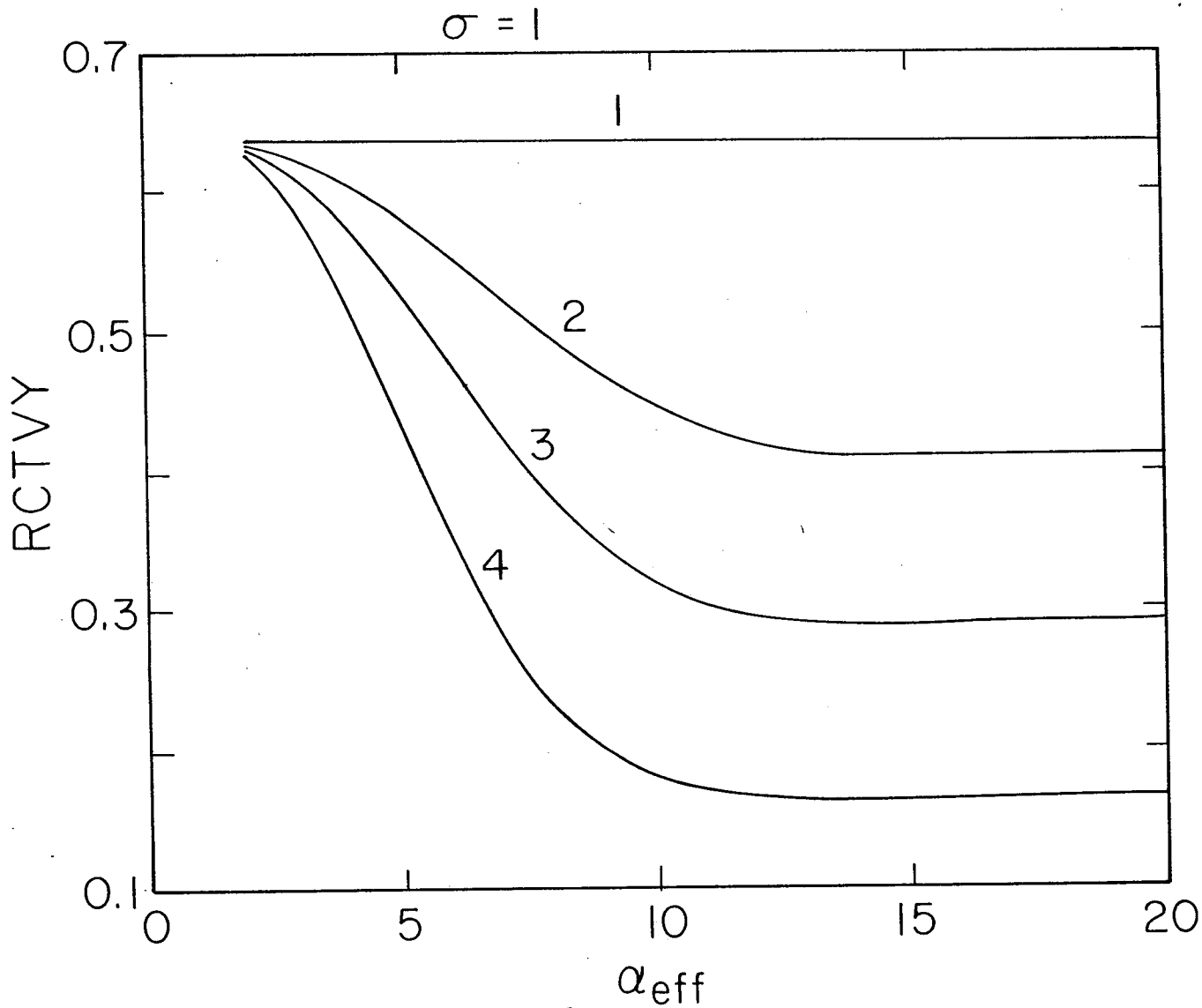

Fig. 21(b)

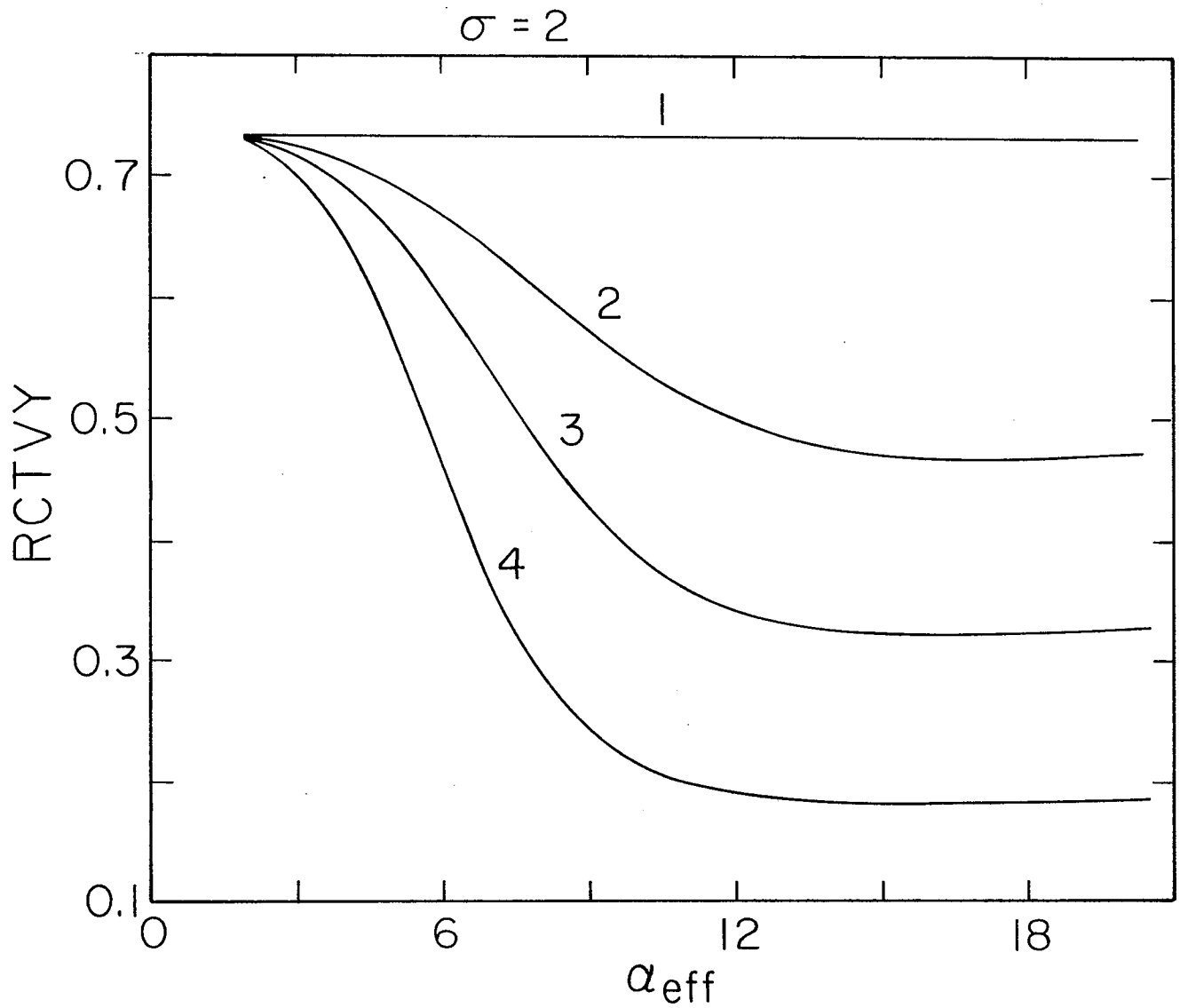

Fig. 21(c)

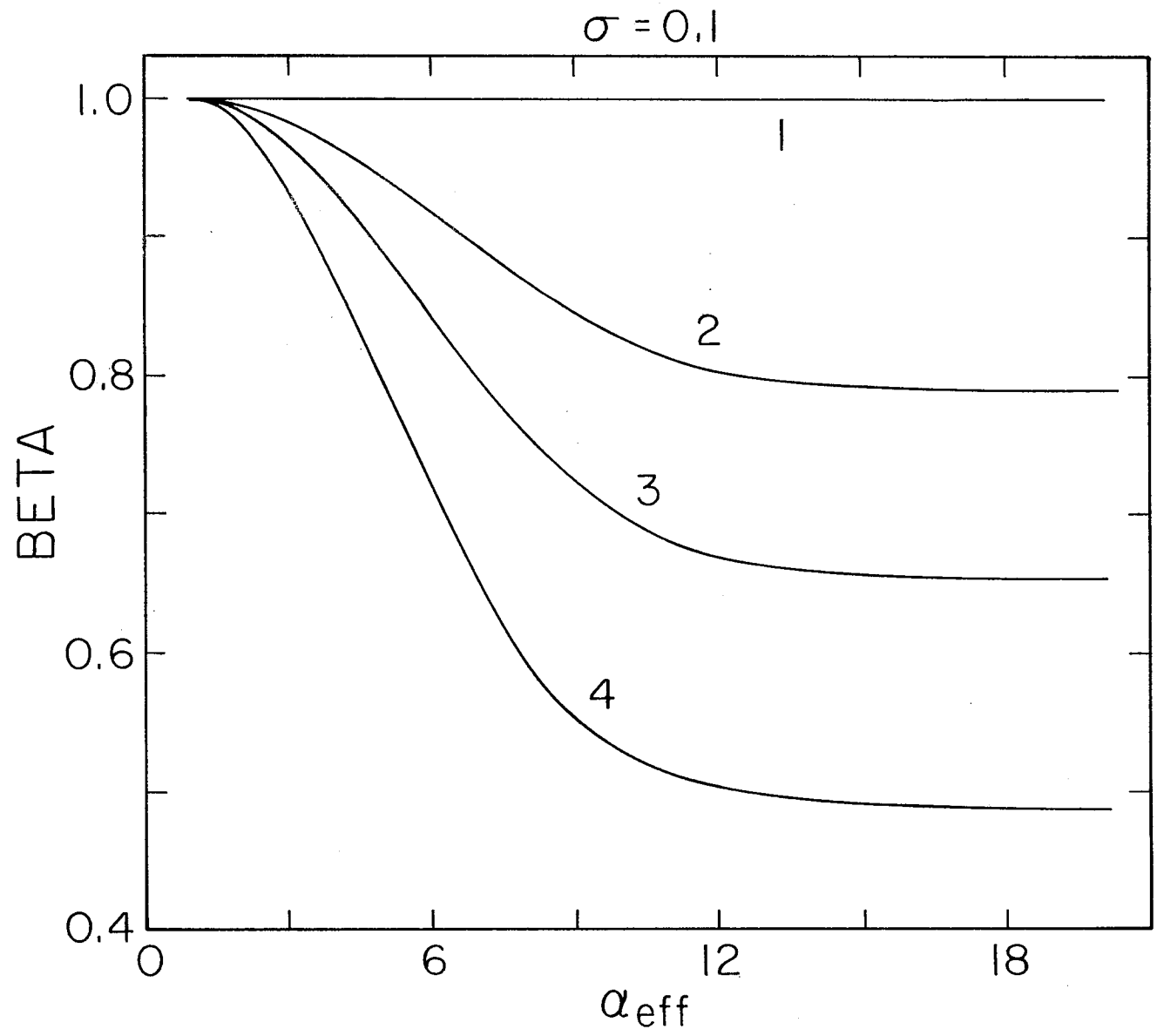

Fig. 22(a)

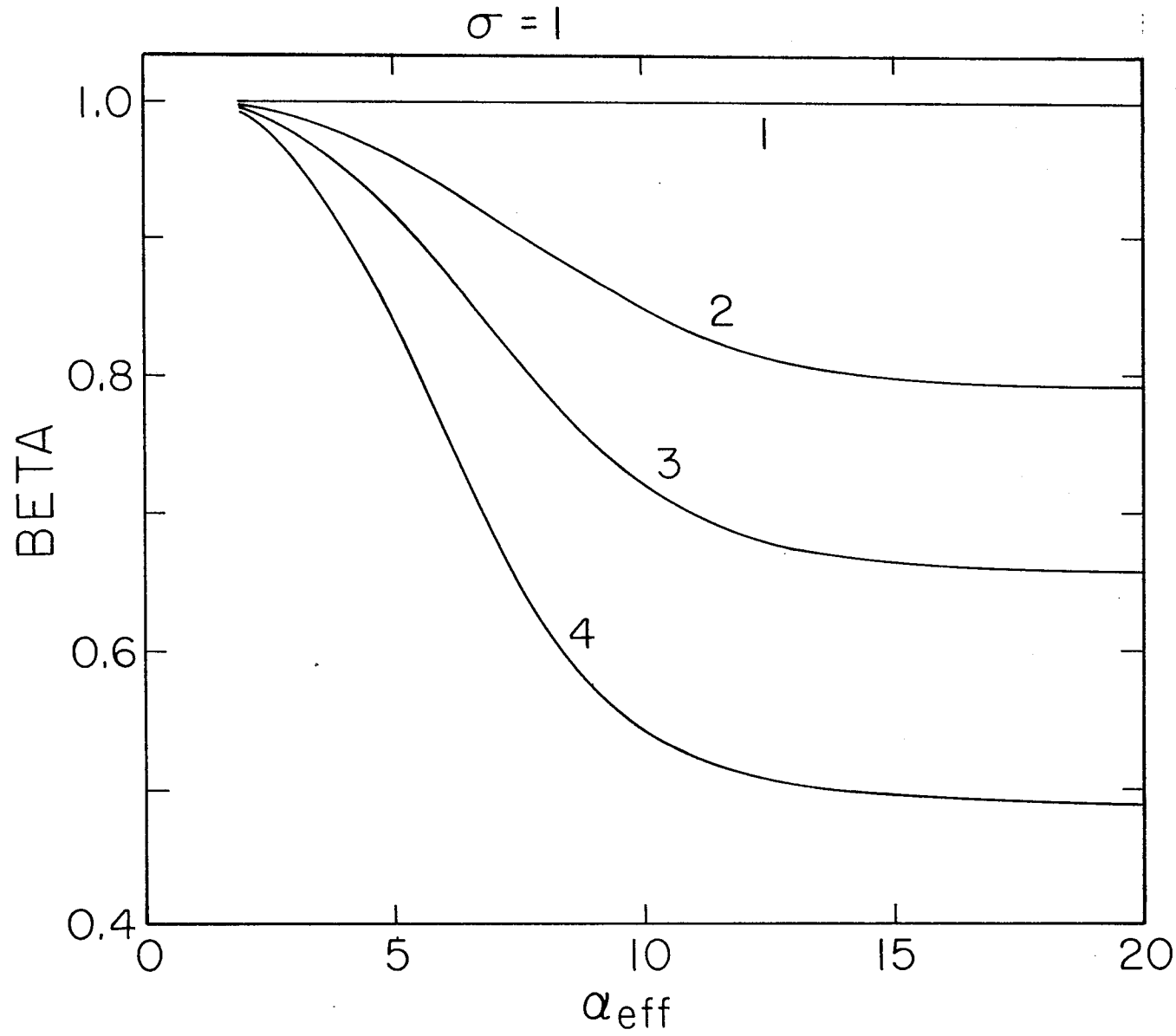

Fig. 22(b)

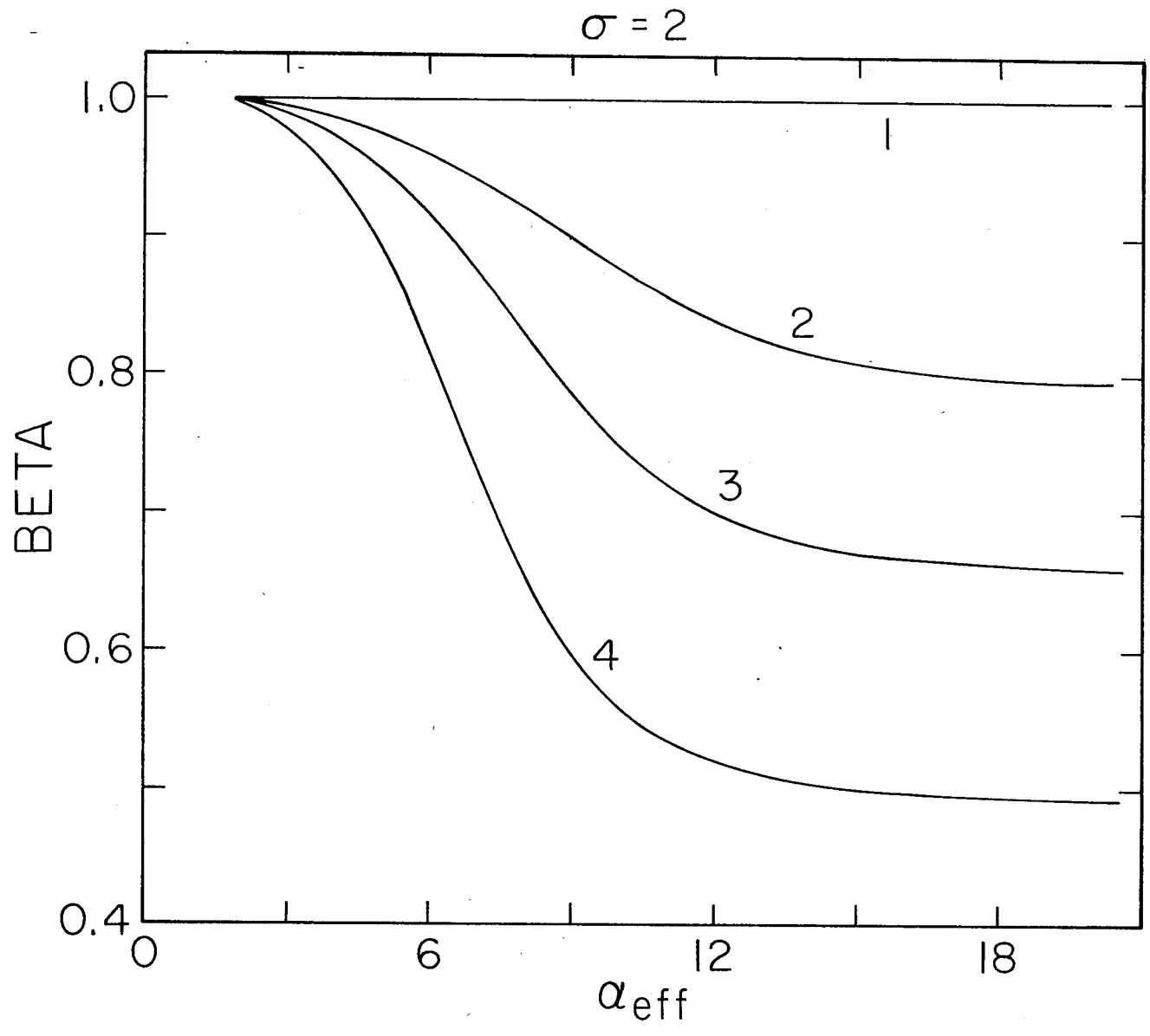

Fig. 22(c)

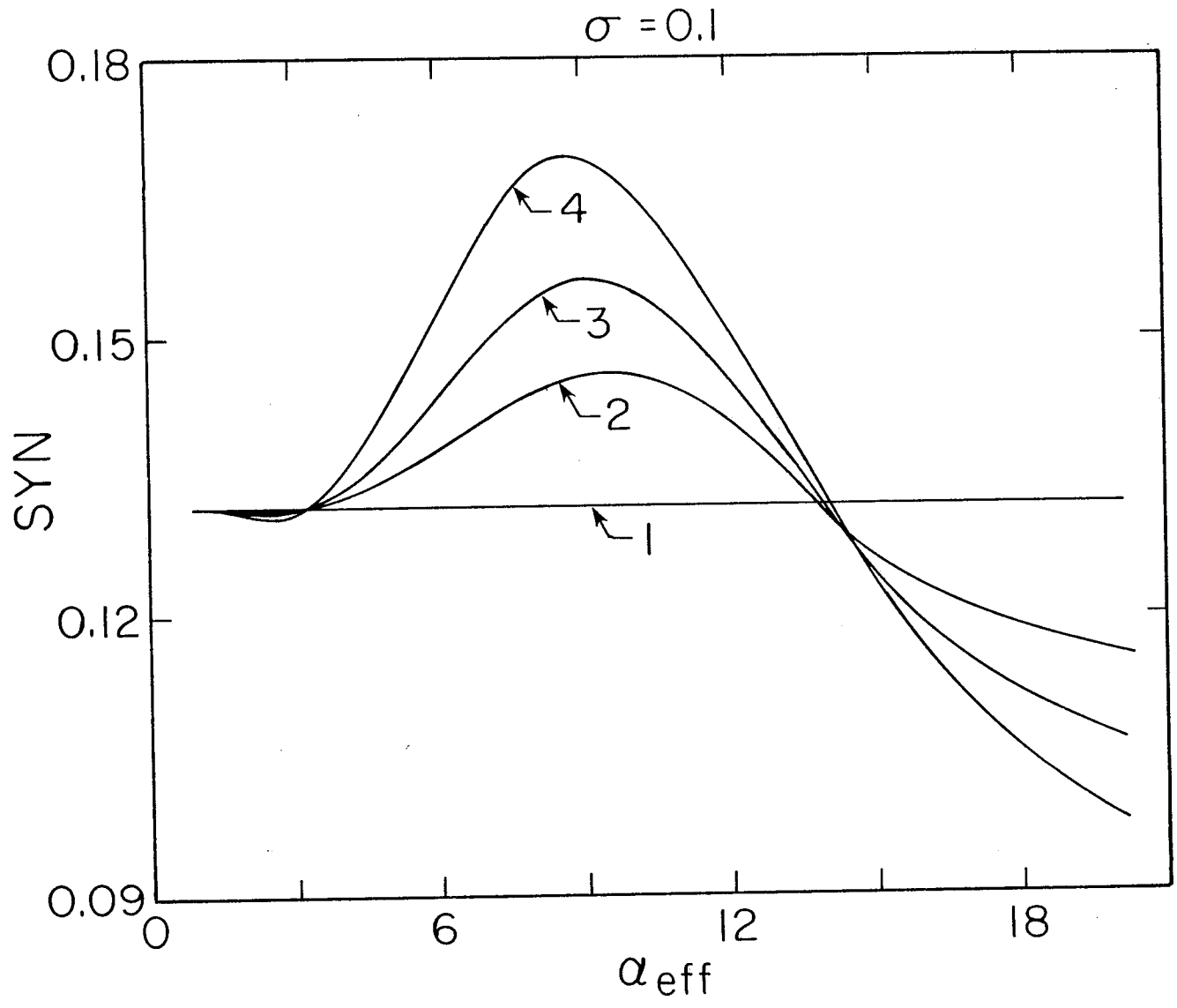

Fig. 23(a)

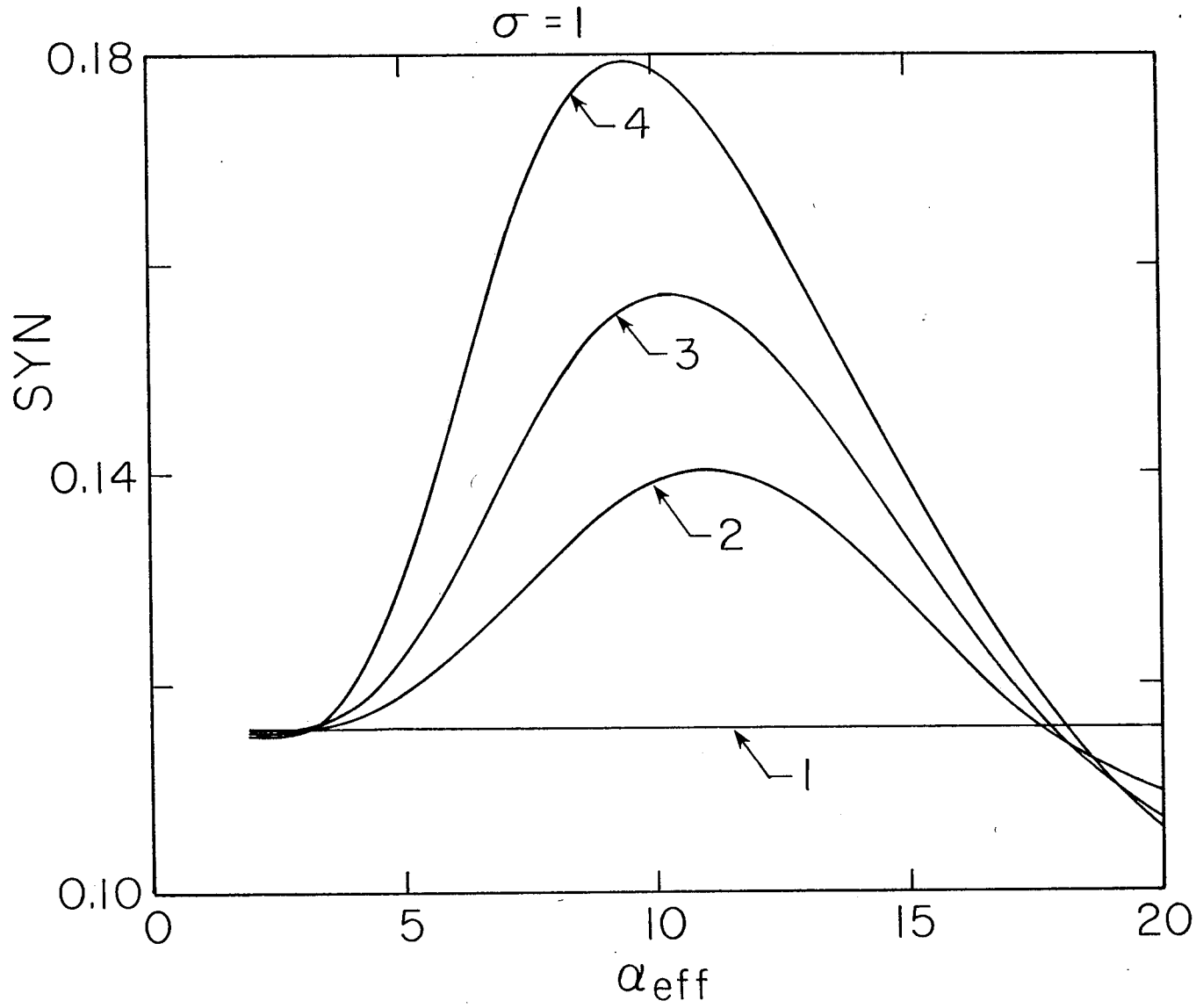

Fig. 23(b)

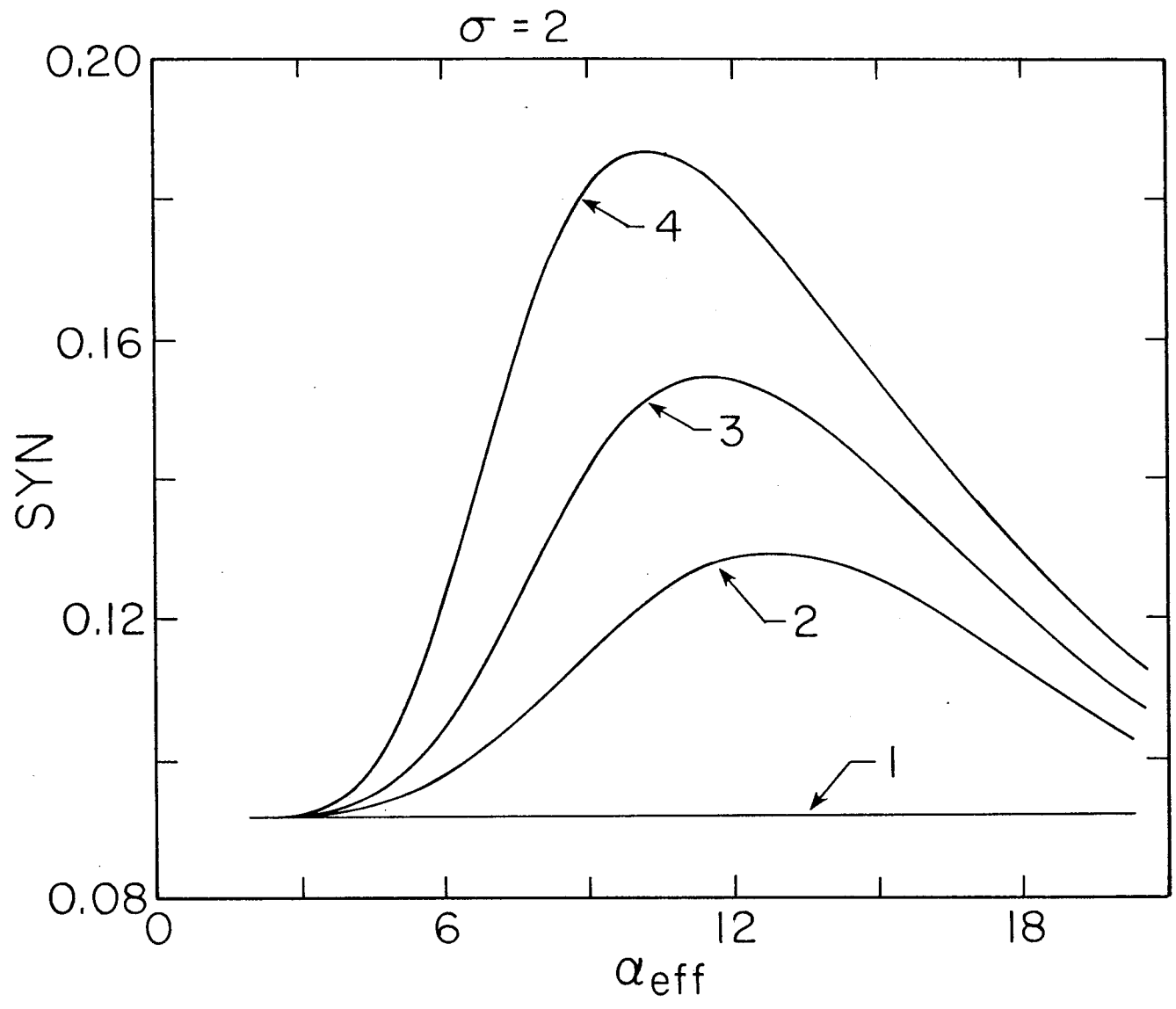

Fig. 23(c)